

Development and Application of StrainNet: Improved Myocardial Strain Analysis of Cine MRI by Deep Learning from DENSE

A

Dissertation

Presented to

the faculty of the School of Engineering and Applied Science

University of Virginia

in partial fulfillment
of the requirements for the degree

Doctor of Philosophy

by

Yu Wang

May 2024

APPROVAL SHEET

This
Dissertation
is submitted in partial fulfillment of the requirements
for the degree of
Doctor of Philosophy

Author: Yu Wang

This Dissertation has been read and approved by the examining committee:

Advisor: Frederick Epstein

Advisor:

Committee Member: Kenneth Bilchick

Committee Member: Craig Meyer

Committee Member: Amit Patel

Committee Member: Claudia Prieto

Committee Member: Miaomiao Zhang

Committee Member:

Accepted for the School of Engineering and Applied Science:



Jennifer L. West, School of Engineering and Applied Science

May 2024

Abstract

Myocardial strain imaging is used for the evaluation of multiple types of heart disease including the detection of chemotherapy-induced cardiotoxicity (1), for optimization of cardiac resynchronization therapy (CRT) (2), for outcome prediction after myocardial infarction (3) and for identification of subclinical cardiac dysfunction in obesity and diabetes (4). CMR methods such as myocardial tagging (5), displacement encoding with stimulated echoes (DENSE) (6, 7), and strain-encoded imaging (8) acquire images specifically designed to measure intramyocardial deformation and strain, and can be referred to as strain-dedicated methods. Alternatively, feature tracking (FT) (9) estimates strain from routine cine balanced steady-state free precession (bSSFP) images. Recent studies that evaluated both DENSE and FT in the settings of acute myocardial infarction and CRT found that DENSE outperformed FT for prognostication (2, 3). Studies have shown that DENSE is reproducible for global and segmental strain (10), whereas FT has poor reproducibility for segmental strain (11). While DENSE provides well-validated and more predictive strain than FT, the time needed to acquire DENSE images may not always be compatible with an efficient clinical workflow. A strain method with performance similar to DENSE and the efficiency of FT would be ideal.

In this thesis, a novel deep learning workflow termed StrainNet was developed and validated to predict intramyocardial tissue motion and strain from myocardial contours. StrainNet was trained using 2D+t DENSE data and applied to cine bSSFP MR images, and validated on both healthy volunteers and patients from multiple sites. The performance of StrainNet was compared with commercial FT algorithm, with DENSE as the reference. To further improve the model performance in complex motion patterns especially motions with spatiotemporal long-term dependencies, we developed TransStrainNet, a transformer-based network combining the self-

attention mechanisms for long-term dependencies and the locality properties of convolution, to capture both global and local patterns for improved intramyocardial motion estimation from contour motion. TransStrainNet was validated against StrainNet on general testing dataset and the subgroup of left bundle branch block (LBBB) with distinctive and complicated mechanical contraction patterns. In addition to technical development, TransStrainNet models were assessed on the prognostication of CRT patients and compared with commercial FT. The strain-based parameter (circumferential uniformity ratio estimated with singular value decomposition) from commercial FT and TransStrainNet would be calculated and used for 6-month response, 4-year survival predictions and risk stratifications.

In summary, StrainNet models provide accurate and convenient global and segmental strain analysis of routine cine MR images in healthy controls and patients with heart diseases, providing better prognostic performance for cardiac resynchronization therapy response and outcome predictions. These findings will facilitate greater use of strain cardiac MRI in research and in clinical settings.

Table of Contents

Chapter 1 – Introduction	13
1.1 Cardiac Function and Myocardial Strain Imaging	14
1.2 CMR Strain Methods	17
1.2.1 Cine DENSE.....	18
1.2.2 Feature Tracking.....	20
1.3 Deep Learning in Cardiac MR and Myocardial Strain Analysis	22
1.3.1 Deep Learning in Cardiac MR	22
1.3.2 Deep Learning in Myocardial Motion Estimation and Strain Analysis	24
1.4 Cardiac Resynchronization Therapy (CRT).....	25
1.5 Scope of Dissertation	26
Chapter 2 – StrainNet.....	28
2.1 Introduction	29
2.2 Methods.....	30
2.2.1 Subjects and Imaging Protocol.....	30
2.2.2 Algorithm Performance Evaluation Using DENSE Contours and DENSE Displacement	31
2.2.3 Deep Learning Architecture	31
2.2.4 Data Pre-processing.....	33
2.2.5 Selection of Training and Independent Testing Datasets	33
2.2.6 Statistical Analysis	34
2.3 Results	34

2.3.1 Examples of End-systolic Displacement and E_{cc} Maps and E_{cc} -time Curves from Volunteers and Heart Disease Patients.....	34
2.3.2 End-Point-Error	37
2.3.3 Detection of Transmural Strain Gradient	37
2.3.4 Correlations and Agreement of End-systolic E_{cc} between StrainNet, FT, and DENSE38	
2.4 Discussion	44
2.5 Appendix	46
2.5.1 Demographic Information of the Dataset	46
2.5.2 Correlation and Bland-Altman Plots of StrainNet and FT Analyses of Basal Cine bSSFP Slices with DENSE.....	49
2.5.3 Correlation and Bland-Altman Plots of StrainNet and FT Analyses of Mid-ventricular Cine bSSFP Slices with DENSE	50
2.5.4 Correlation and Bland-Altman Plots of StrainNet and FT Analyses of Apical Cine bSSFP Slices with DENSE.....	51
2.5.5 Comparison of Layer-specific End-systolic E_{cc} (%) among FT, StrainNet and DENSE for Basal, Mid-level and Apical Slices.....	52
2.5.6 Full Details of Cine and DENSE Imaging Parameters.....	52
Chapter 3 – TransStrainNet	54
3.1 Introduction.....	55
3.2 Methods.....	56
3.2.1 Convolution vs. Attention	56
3.2.2 Transformer with Self-attention Mechanisms	59
3.2.3 Transformer with 3D Patches as Inputs.....	61

3.2.4 Swin Transformer Blocks.....	62
3.2.5 Model Training and Testing.....	65
3.2.6 Model Performance Evaluation.....	65
3.3 Results.....	66
3.3.1 Computation Time.....	66
3.3.2 End-systolic Displacement, E_{cc} Maps and E_{cc} -time Curves from Healthy Volunteers and Patients with Heart Disease	66
3.3.3 Correlations and Agreement of End-systolic E_{cc} and Whole E_{cc} -time Curves.....	69
3.4 Discussion.....	70
Chapter 4 – Application in CRT Patient Prognostication.....	73
4.1 Background.....	74
4.1.1 Strain in CRT.....	74
4.1.2 StrainNet Analysis of CRT Patients.....	75
4.2 Methods.....	76
4.2.1 Patient Cohort Description	76
4.2.2 Determination of CURE-SVD.....	79
4.3.3 Prediction of CRT Response and Outcomes	80
4.3.4 Statistics Analysis.....	80
4.4 Results.....	81
4.4.1 CRT Patients Response and Outcome Predictions.....	81
4.4.2 CRT Cohort Risk Stratification	84
Chapter 5 – Conclusions and Future Directions	86
5.1 Conclusions.....	87

5.2 Future Directions.....	87
5.2.1 Reproducibility of StrainNet	87
5.2.2 StrainNet Extension to Multi-modality	88
5.2.3 StrainNet Extension to Longitudinal Strain	89
5.2.4 StrainNet Application to Cardiotoxicity.....	89
5.2.5 Inline StrainNet	90
Appendix A – FlowNet2-based StrainNet	92
A.1 Background and Rationale	93
A.2 Abstract	93
Appendix B – StrainNet Applied to Echocardiography	102
B.1 Abstract.....	103
Appendix C – List of Publications.....	109
C.1 Awards.....	110
C.2 First Author Manuscripts.....	111
C.3 Other Manuscripts	111
C.4 First Author Conference Abstracts	113
C.5 Invention Disclosures	115
Acknowledgements.....	116
References.....	117

List of Figures

Figure 1-1: Schematic showing the definition of circumferential strain. 16

Figure 1-2: The circumferential strain bullseye plot with respect to the 16-segment left ventricular model. Adapted from (30)..... 16

Figure 1-3: Example of cine DENSE images, displacement map, circumferential strain map and segmental strain-time curves on a healthy subject at end-systole. (A) Magnitude image. (B) Phase image with displacement-encoded in the X direction. (C) Phase image with displacement-encoded in the Y direction. The phase values in the myocardium reflect the tissue displacement in the two directions respectively. (D, E) Myocardial displacement field and circumferential strain map at the same frame. (F) Segmental circumferential strain-time curves along the cardiac cycle. 19

Figure 1-4: Example of commercial feature tracking algorithm on short-axis cine MRIs. (A) LV segmentation on a series of cine MRIs at end-diastole. (B) Bull’s Eye plots of peak circumferential strain derived from feature tracking. (C) Segmental circumferential strain-time curves along the cardiac cycle..... 21

Figure 1-5: Literature review. (A) Number of AI-CMR publications per year. (B) AI-CMR studies categorized by machine learning tasks. (C) AI-CMR studies categorized by CMR modalities... 23

Figure 2-1: Schematic showing the proposed StrainNet to predict intramyocardial displacement from contour motion. A 3D Unet architecture consisting of convolution, batch normalization, ReLU layers, residual connections and pooling layers was used. Our models were trained with the Adam optimizer using a total of 120 epochs. The initial learning rate was set to $1e-4$, with a halving schedule at 20 and 100 epochs. During training, the inputs were a time series of myocardial contours derived from DENSE magnitude images and the ground truth data were displacement measurements computed from DENSE phase images. End-point-error (EPE) was the loss to

calculate the difference between the estimated displacement maps and ground truth DENSE displacements. During testing, the inputs were a time series of myocardial contours derived from routine bSSFP cine images. 32

Figure 2-2: Flow diagram showing patient (n = 161) and volunteer (n = 144) datasets. The StrainNet CNN was trained with the DENSE training dataset (80% of study participants), and assessed using an independent testing dataset including DENSE and cine images (20% of study participants)..... 34

Figure 2-3: Example end-systolic displacement and E_{cc} maps comparing StrainNet analysis of bSSFP cine images and DENSE for (A) a healthy volunteer (female; age, 23 year) and (B) a heart failure patient with left bundle branch block (female; age, 71 year). 35

Figure 2-4: Example segmental circumferential strain-time curves for StrainNet analysis of bSSFP cine MRI, FT analysis of bSSFP cine MRI, and DENSE for (A) a healthy volunteer (age, 28 year; female) and (B) a myocardial infarct patient (age, 42 year; male).The healthy volunteer has 30 frames with repetition time (TR) = 32.17ms for bSSFP cine MRI, and 24 frames with TR = 30ms for cine DENSE; the patient has 25 frames with TR = 34.44ms for bSSFP cine MRI, and 29 frames with TR = 30ms for cine DENSE. 36

Figure 2-5: Layer-specific E_{cc} measurements for FT analysis of bSSFP cine MRI, StrainNet analysis of bSSFP cine MRI, and DENSE. FT: subendocardium, $-22.88 \pm 2.92\%$; middle layer, $-16.40 \pm 2.54\%$, subepicardium, $-10.13 \pm 2.35\%$, [P<.001]. StrainNet: subendocardium, $-22.62 \pm 2.26\%$; middle layer, $-19.20 \pm 1.89\%$; subepicardium, $-15.71 \pm 1.62\%$, [P<.001]. DENSE: subendocardium, $-21.60 \pm 3.34\%$; middle layer, $-18.71 \pm 2.92\%$; subepicardium, $-15.75 \pm 2.95\%$, [P<.001]. There was significant difference between FT and DENSE for all three layers [P=.007 for subendocardium, P<.001 for middle layer, and P<.001 for subepicardium]; there was

significant difference between StrainNet and DENSE for subendocardium [P=.002], and no significant difference for middle layer [P=.09] and subepicardium [P=.91]. 38

Figure 2-6: Correlation and Bland-Altman plots comparing StrainNet and FT analyses of bSSFP cine MRI with DENSE for end-systolic (A) global and (B) segmental E_{cc} 40

Figure 2-7: Bull’s eye plots of per-segment E_{cc} for intraclass correlation coefficient (ICC, %), coefficient of variation (CV), bias and limits of agreements comparing StrainNet and FT with DENSE. A linear mixed-effects model was performed over techniques for each segment, and an asterisk in the bias column was indicated as having statistical significance with reference DENSE. 44

Figure 2-8 Supplementary: Correlation and Bland-Altman plots of StrainNet and FT analyses of basal cine bSSFP slices with DENSE for end-systolic (A) global and (B) segmental E_{cc} 49

Figure 2-9 Supplementary: Correlation and Bland-Altman plots of StrainNet and FT analyses of mid-ventricular cine bSSFP slices with DENSE for end-systolic (A) global and (B) segmental E_{cc} 50

Figure 2-10 Supplementary: Correlation and Bland-Altman plots of StrainNet and FT analyses of apical cine bSSFP slices with DENSE for end-systolic (A) global and (B) segmental E_{cc} 51

Figure 3-1: Illustration and Comparison of Convolution and Attention Mechanisms. (A) illustrates the fundamental differences between convolution and attention mechanisms. Convolution, depicted by the blue arrows, focuses on local regions, processing information in a confined receptive field. In contrast, the attention mechanism, indicated by green arrows, captures dependencies over larger distances, allowing a broader context to be considered in the analysis. (B) contrasts the ability of convolution and attention mechanisms to capture long-term dependencies in cardiac motion. The orange box at the septum highlights the area of interest.

Convolution, marked by the blue box, is limited to immediate surroundings, while attention, shown by the green box, encompasses a wider field, capturing the compensatory relationship between septal stretching and lateral contraction. The strain-time curve further demonstrates the attention mechanism's capacity to discern temporal long-term dependencies, such as the sequence of the lateral wall's prestretch and subsequent contraction. 58

Figure 3-2: Illustration of the encoder-decoder structure of the Transformer architecture. 60

Figure 3-3: General description of Swin transformer-based StrainNet architecture. Encoder, decoder and bottleneck are all composed of 3D (2D+t) Swin transformer blocks. Patch merging and expanding were used to provide the hierarchical architecture, and the encoder latent features were skip connected to decoder features to compose an UNet architecture. Patch merging was used for down-sampling where the input features of each group of $2 \times 2 \times 2$ are concatenated and projected by a linear layer. Patch expanding, in reverse, up-sampled the compressed features into higher resolutions. Our model was trained with the AdamW optimizer using a total of 200 epochs. The initial learning rate was set to $1e-4$, with a halving schedule every 50 epochs. During training, the inputs were a time series of myocardial contours derived from DENSE magnitude images and the ground truth data were tissue displacement measurements computed from DENSE phase images. End-point-error (EPE) was the loss to calculate the difference between the estimated displacement maps and ground truth DENSE displacements. During testing, the inputs were a time series of myocardial contours derived from routine bSSFP cine images. DENSE data at matched slice locations served as the reference. 64

Figure 3-4: Example of end-systolic displacements and E_{cc} maps and segmental circumferential strain-time curves comparing (A) StrainNet and (B) TransStrainNet analysis of bSSFP cine images and (C) ground-truth DENSE for a healthy volunteer. 67

Figure 3-5: Example of end-systolic displacements and E_{cc} maps and segmental circumferential strain-time curves comparing (A) StrainNet and (B) TransStrainNet analysis of bSSFP cine images and (C) ground-truth DENSE for a heart failure patient with left bundle branch block. 68

Figure 4-1: Time-Dependent Receiver-Operating Characteristic Curves for CRT patient 6-month response prediction with 5-fold cross validation. Time-dependent receiver-operating characteristic curves based on CURE-SVDs are shown for 3 models: (A) Commercial Feature Tracking, (B) TransStrainNet and (C) DENSE. 82

Figure 4-2: Time-Dependent Receiver-Operating Characteristic Curves for CRT patient 4-year survival prediction with 5-fold cross validation. Time-dependent receiver-operating characteristic curves based on CURE-SVDs are shown for 3 models: (A) Commercial Feature Tracking, (B) TransStrainNet and (C) DENSE. 83

Figure 4-3: Stratified Kaplan-Meier analysis. Kaplan-Meier survival curves are presented for the two groups (Group 1: with lower CURE-SVD score, Group 2: with higher CURE-SVD score) stratified by the medium of CURE-SVDs from (A) Commercial Feature Tracking, (B) TransStrainNet and (C) DENSE. 85

Figure 5-1: Example E_{cc} maps from a breast cancer patient before (A) and 3 months after (B) initiating chemotherapy. Impaired strain, especially in the septum and inferior wall are detected and quantified in (B). 90

List of Tables

Table 2-1: Comparison of agreement of global and segmental E_{cc} for all slices.	41
Table 2-2: Comparison of agreement of per-slice global and segmental E_{cc}	41
Table 2-3 Supplementary: Demographic information and left ventricular volumetric data for patients and volunteers.....	47
Table 2-4 Supplementary: Comparison of Layer-specific End-systolic E_{cc} (%) among FT, StrainNet and DENSE.....	52
Table 3-1: Comparison of agreement between StrainNet, TransStrainNet and Feature Tracking with DENSE for global and segmental peak-systolic E_{cc} and whole E_{cc} -time curve errors	69
Table 4-1: Demographics of the 200 CRT patients. Values are median (interquartile range) or n (%). ACE = angiotensin-converting enzyme; ARB = angiotensin receptor blocker; BMI = body mass index; BNP = B-type natriuretic peptide; BP = blood pressure; CABG = coronary artery bypass graft; CURE-SVD = circumferential uniformity ratio estimate with singular value decomposition; GFR = glomerular filtration rate; LBBB = left bundle branch block; LGE = late gadolinium enhancement; LVEDVI = left ventricular end-diastolic volume index; LVEF = left ventricular ejection fraction; LVESVI = left ventricular end-systolic volume index; NYHA = New York Heart Association; QLV = QRS-LV electrogram time; RBBB = right bundle branch block; RVEDVI = right ventricular end-diastolic volume index; RVEF = right ventricular ejection fraction; RVESVI = right ventricular end-systolic volume index.	77

Chapter 1 – Introduction

1.1 Cardiac Function and Myocardial Strain Imaging

Heart failure is a prevalent condition that is linked with substantial morbidity, mortality, and economic impact on healthcare system (12). The critical step in managing heart disease involves identifying heart anomalies in both structure and function. Techniques like echocardiography (ECHO), computed tomography (CT), and MRI play a pivotal role in the non-invasive examination of heart structures and the measurement of cardiac performance (13). The left ventricular ejection fraction (LVEF), a measure based on the contrast between end-systolic and end-diastolic ventricular volumes, is a primary metric used in cardiac function quantification. It represents the percentage fluctuation in left ventricular (LV) volume and is instrumental in both the diagnosis and patient categorization during treatment for various conditions. Nevertheless, due to LVEF's volumetric nature, it might not capture regional and subtle changes in ventricular function, especially evident in cases involving minor or subclinical tissue modifications. For instance, LVEF might inaccurately suggest heightened systolic function in patients with a hypertrophic myocardium (14). It generally measures overall heart performance, potentially overlooking regional disparities or nuanced shifts that regional assessments could capture more effectively (15).

Myocardial strain imaging evaluates LV mechanics through myocardial deformation and provides a more in-depth characterization into heart function (16, 17). This approach, evaluating heart function by quantifying myocardial muscle deformation, allows for detailed analysis across ventricular segments and throughout multiple frames of the cardiac cycle. Specifically, as shown in Figure 1-1, parameters such as circumferential shortening, radial thickening, or longitudinal shortening provides different aspects of measurements of myocardial contractile function, both globally and regionally. Myocardial strain imaging has been shown to add incremental diagnostic or prognostic value over conventional imaging of ejection fraction (EF) in many clinical contexts

and, in general, detects cardiac dysfunction earlier than imaging of EF (18). For example, myocardial strain imaging is routinely performed and guideline recommended for monitoring of cardiotoxicity in patients undergoing certain anti-cancer therapies (19-21). Other clinical applications include image-guidance and prognostication for heart failure patients undergoing cardiac resynchronization therapy (CRT) (22, 23), optimizing the timing of aortic valve replacement surgery (24), prognosis after acute myocardial infarction (25), and risk stratification in dilated cardiomyopathy (26). Myocardial strain imaging is most commonly performed using echocardiography; however, the use of CMR is increasing and CMR is considered the reference standard modality for myocardial strain imaging (27, 28). Furthermore, CMR strain can be combined with CMR cine imaging of left ventricular (LV) volumes and EF, perfusion imaging, late gadolinium enhancement, and T1 mapping, facilitating a multiparametric evaluation of the heart for precision diagnosis, prognosis, and procedure planning.

Regarding strain calculation, the equation for Lagrangian strain calculation (29) is defined by how much the myocardium is deformed as follows:

$$strain(t) = \frac{L_t - L_0}{L_0} \times 100$$

where L_0 is the initial myocardial length at end-diastole, and L_t stands for the length at any subsequent time point length. This is quantified by determining the percentage of shortening or lengthening throughout the cardiac cycle.

To illustrate the segmental deformation of the myocardium spatially, the American Heart Association (AHA) bull's-eye plot is utilized, a visual representation of myocardial contractility based on the 16 or 17-segment model (30) (Figure 1-2). Strain-time curves offer values of peak systolic strain, time to peak strain and depict changes in strain across the cardiac cycle.

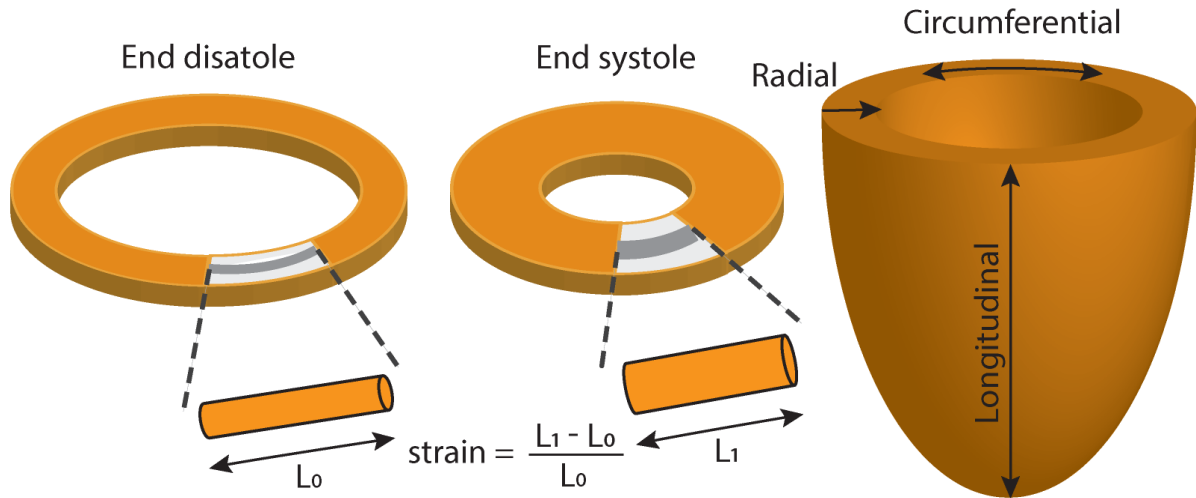


Figure 1-1: Schematic showing the definition of circumferential strain.

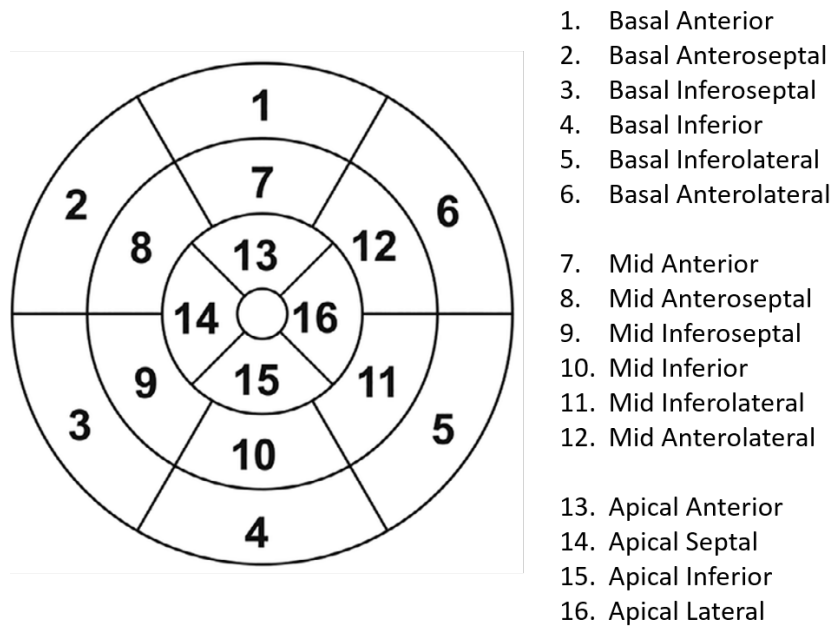


Figure 1-2: The circumferential strain bullseye plot with respect to the 16-segment left ventricular model. *Adapted from (30).*

1.2 CMR Strain Methods

Myocardial deformation can be assessed from all imaging modalities of ECHO (31-33), MRI (5-9) and CT (34-36). Myocardial strain imaging is most commonly performed using speckle-tracking echocardiography (STE); however, the use of CMR is increasing and CMR is considered the reference standard modality for myocardial strain imaging (27, 28). Within CMR there are multiple strain imaging methods with either strain-dedicated sequences or post-processing algorithms based on routine cine MRI, such as MR tagging (5, 37), harmonic phase (HARP) MRI (38), strain-encoded (SENC) MRI (8), cine displacement-encoded stimulated echoes (cine DENSE) (7) and feature tracking (9).

MR tagging consists of a preparation phase where tag lines or tag grids are superimposed to the myocardium at the beginning of a cine sequence. The tag lines, deforming along with myocardial movements throughout the cardiac cycle, facilitate the direct quantification of myocardial displacement. The motion estimation is achieved by tracking the tags and interpolate the intersect points throughout consecutive frames. Despite its high reproducibility, MR tagging post-processing is complicated and time-consuming, which impedes its clinical application. HARP is an advanced post-processing algorithm from MR tagging acquisition. HARP simplifies the tracking steps and improve accuracy by applying a band-pass filter in the k-space extract the spectral peaks and produce the harmonic phase images. Myocardial motion between consecutive frames are then tracked by matching the HARP values in the later time frame.

SENC applies tag lines as a series of planes in the through-plane direction rather than as a series of lines in the in-plane direction as in MR tagging. The myocardial motion causes a shift in the location of the peak spectrum in k space, from which myocardial strain is estimated. However,

SENC can only provide the longitudinal strain component but not circumferential or radial strains. Further, SENC requires prior knowledge of strain ranges and the k-space slice profile (39).

1.2.1 Cine DENSE

DENSE is a highly reproducible method (40) that directly measures intramyocardial motion and strain with high accuracy (41). Rather than tracking image features after the acquisition, DENSE measures myocardial displacement and strain by directly encoding the displacement into phase images (Figure 1-3). DENSE sequence is performed by a displacement encoding module consisting of two 90-degree RF pulses with encoding gradients in between. DENSE signal could be represented by the following equation:

$$\begin{aligned}
 M_{xy}(x, t) &= \frac{M}{2} \sin(\alpha) e^{-\frac{t}{T_1}} e^{-ik_e \Delta x} \\
 &+ M_0 \sin(\alpha) \left(1 - e^{-\frac{t}{T_1}}\right) e^{-ik_e(x+\Delta x)} \\
 &+ \frac{M}{2} \sin(\alpha) e^{-\frac{t}{T_1}} e^{-ik_e \Delta x} e^{-i2k_e x}
 \end{aligned}$$

There are three components in DENSE signal that correspond to three echoes centered at $0, k_e, 2k_e$, respectively. The first signal is the desired stimulated echo whose phase is proportional to the myocardial displacement Δx since the application of displacement encoding module. The second term is T_1 -relaxation echo, which will be eliminated by phase cycling. The third term is complex conjugate echo which be adjusted to outside the acquisition window by an appropriate k_e value.

After acquiring the cine DENSE images, motion-guided segmentation of the LV myocardium (42), phase-unwrapping algorithm for the LV myocardial pixels, and Lagrangian displacement and strain calculation were sequentially performed using previously developed and

validated fully-automatic methods (41). For the semi-automatic motion-guided segmentation, an initial region-of-interest of the left ventricular (LV) region is delineated manually on a single frame, followed by automatic propagation across all other frames. Manual correction will be applied if needed. Then phase unwrapping algorithm is applied to LV pixels to obtain true phase values. Next, the displacement fields are directly derived from the unwrapped phase images. By interpolating within these displacement fields, the motion trajectories of individual pixels throughout the cardiac cycle are estimated. Finally, the strains are calculated from the through-time displacement maps for each myocardial pixel. Figure 1-3 shows a healthy volunteer example of cine DENSE images, displacement map, circumferential strain map at end-diastole and segmental strain-time curves.

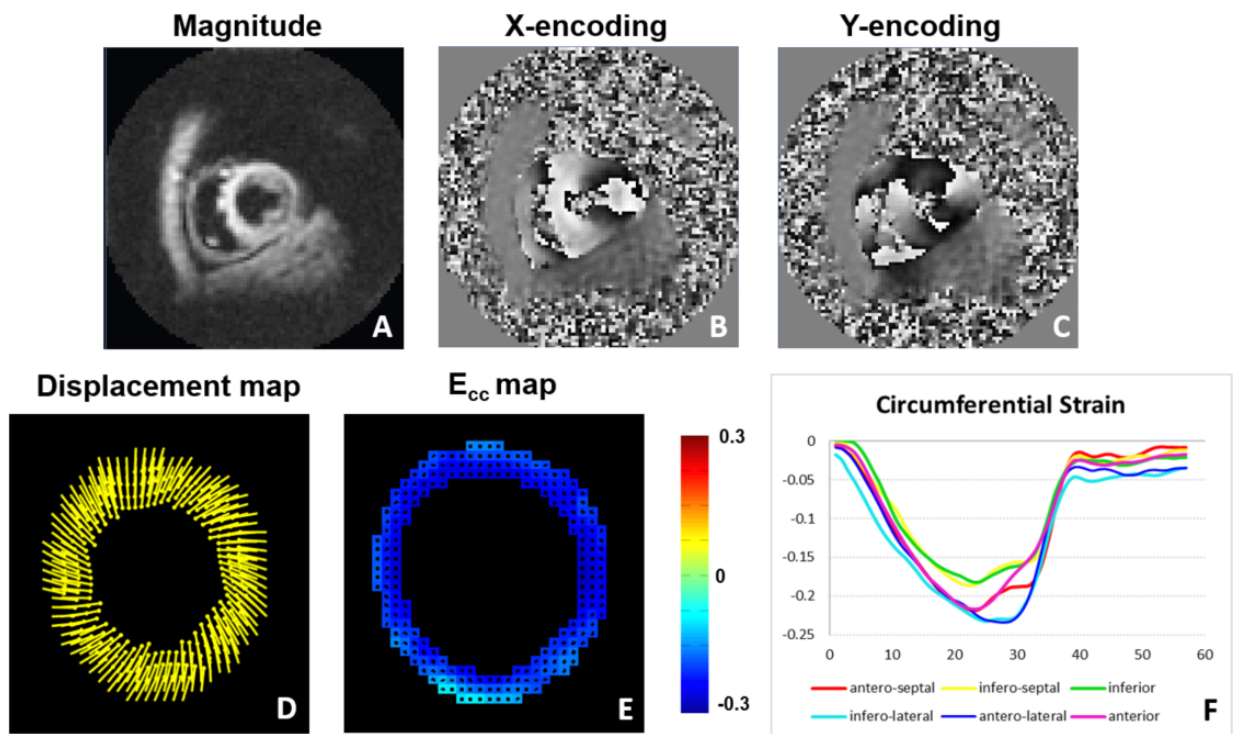


Figure 1-3: Example of cine DENSE images, displacement map, circumferential strain map and segmental strain-time curves on a healthy subject at end-systole. (A) Magnitude image. (B) Phase image with displacement-encoded in the X direction. (C) Phase image with displacement-encoded in the Y direction. The phase values in the myocardium reflect the tissue displacement in the two

directions respectively. (D, E) Myocardial displacement field and circumferential strain map at the same frame. (F) Segmental circumferential strain-time curves along the cardiac cycle.

1.2.2 Feature Tracking

FT is the most widely used and convenient CMR technique (43), as it applies post-processing algorithms to standard CMR cine images. Conventional CMR FT techniques are based on optical flow technology which recovers image motion at each pixel from spatiotemporal image variations (44). Specifically, the endocardial and epicardial contours are detected and tracked as they move through time in the cardiac cycle (43). Then, the optical flow algorithm is applied to the tracked contours to estimate the motion of pixels within the myocardium, from which strain is computed (43). It is important to recognize that FT directly tracks contour features, but does not track intramyocardial features, as the myocardium on standard CMR images generally produces a very uniform signal and doesn't present intramyocardial features suitable for tracking. Figure 1-4 shows a healthy volunteer example of feature tracking on short-axis cine MRI stacks by a commercial software NeoSoft, SuiteHeart.

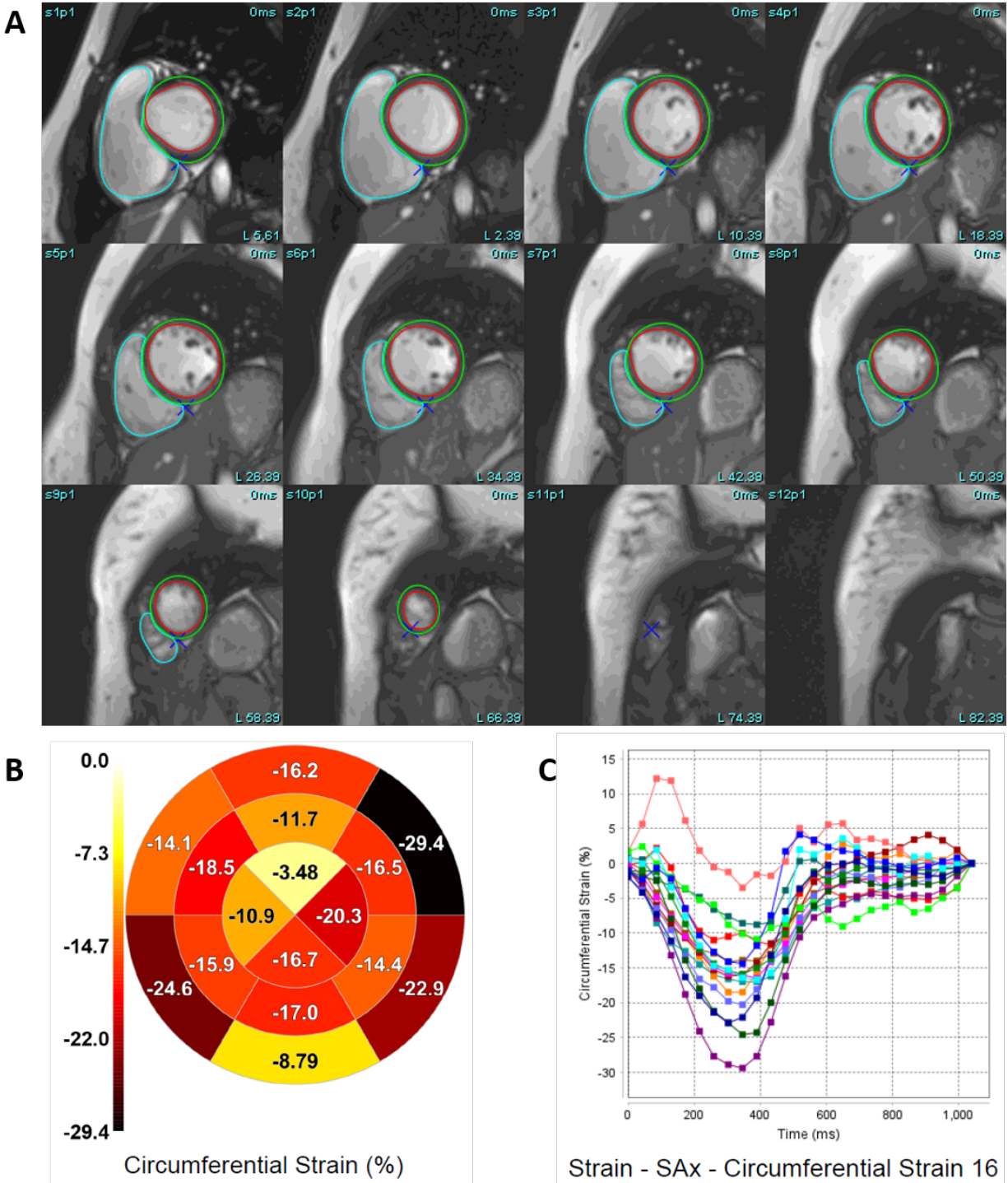


Figure 1-4: Example of commercial feature tracking algorithm on short-axis cine MRIs. (A) LV segmentation on a series of cine MRIs at end-diastole. (B) Bull's Eye plots of peak circumferential strain derived from feature tracking. (C) Segmental circumferential strain-time curves along the cardiac cycle.

1.3 Deep Learning in Cardiac MR and Myocardial Strain Analysis

1.3.1 Deep Learning in Cardiac MR

Deep learning (DL) is one of the branches of artificial intelligence that has seen exponential growth in recent years. The scientific community has focused its attention on DL due to its versatility, high performance, high generalization capacity, and multidisciplinary uses, among many other qualities.

Convolutional neural networks (CNN) with contracting and expanding paths plays a vital role in image processing for a decade (45). U-Net is an extension of encoder-decoder structures with a U-shaped architecture (46). Skip connections are used to combine the high-level semantic features from the decoder and the corresponding detailed feature maps from the encoder, which takes the advantage of both the latent features and reducing distortion by preserving the original high-resolution information. U-Net shows ground-breaking performance on biomedical imaging tasks because it perfectly meets the requirements of medical imaging in terms of its combination of both latent and high-resolution features, convenient and fast training procedure and the small amount of training data used (47).

Recently, vision transformers have emerged as a competitive alternative to CNNs (48). The attention mechanism (49) central to transformers offers several advantages over convolutions, including but not limited to the long-term relationships capture and built-in saliency to give insights into what the model focuses on (50). The excellent global representation capabilities of transformers enable them to exploit long-distance dependencies along the temporal dimension of dynamic cardiac images.

In terms of the CMR domain, deep learning has various applications such as reconstruction, segmentation, motion and deformation analysis and outcome prediction. As shown in Figure 1-5, the number of AI CMR publications per year is increasing rapidly, and with applications ranging from different tasks and sequence modalities, reflecting the increasing research interest and various application with artificial intelligence in CMR domain.

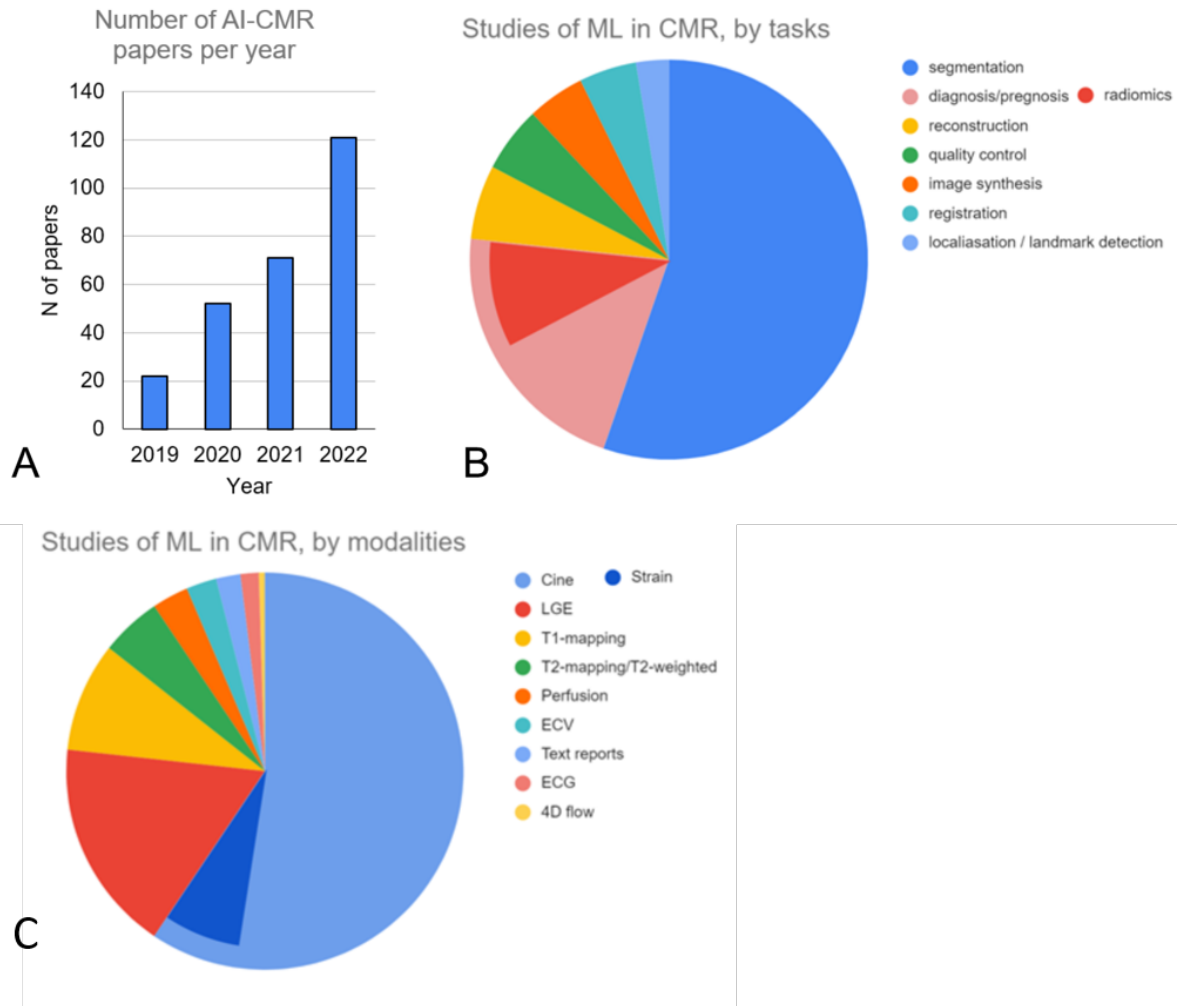


Figure 1-5: Literature review. (A) Number of AI-CMR publications per year. (B) AI-CMR studies categorized by machine learning tasks. (C) AI-CMR studies categorized by CMR modalities.

Figure source: Improving the efficiency of CMR with AI – review of evidence and proposition of a roadmap.

1.3.2 Deep Learning in Myocardial Motion Estimation and Strain Analysis

Recently, learning-based myocardial motion tracking methods have been investigated (51-54) and demonstrated the potential for high performance that ought to be achievable by leveraging big data and the ability of convolutional neural networks to extract intangible and multi-scale features.

In terms of cardiac structure and diseases, DL-based automatic or semi-automatic segmentation applied to structures including the LV, RV, and LA also facilitates the efficient use of feature tracking or other methods to compute strain for each of these chambers (55-58). In terms of network design, most of the cardiac motion tracking models are based on convolutional neural network, particularly using the U-Net structure. In addition, recurrent neural networks (59) and transformers have also been used to better exploit the time dimension. Network inputs are paired 2D (60) or 3D (51) image frames or a sequence of cardiac images (52, 61).

The main challenge in the development of motion tracking methods using deep learning is the lack of ground-truth displacement, velocity, or strain data (52). Previous studies have shown the feasibility of regional strain assessment by deep learning using cine MR images, but they used classical optical-flow to generate the motion ground truth (52) or unsupervised warping loss and smoothness regularizations during training (51, 53, 54). For clinical evaluation, DeepStrain demonstrated high correlation of global circumferential strain and global radial strain with commercial feature tracking in 533 patients (62).

DL for strain also extends beyond the analysis of cine imaging to strain-dedicated CMR sequences. For example, DL-based methods to analyze tagged CMR images has been shown to be superior to harmonic phase analysis with regard to tag tracking accuracy and inference efficiency (63). For the analysis of DENSE CMR, DL for LV segmentation and phase unwrapping provides

fully-automated, and highly accurate and reproducible results for both global and segmental circumferential strain (64).

1.4 Cardiac Resynchronization Therapy (CRT)

CRT is a therapy that uses a biventricular pacemaker to enhance cardiac function by pacing late-activating myocardium which can improve survival rate, enhance heart function, and improve quality of life (65). However, the nonresponse rate is around 40%, and therefore improved prediction of CRT response is of vital importance in managing patients who are potential CRT candidates (66). The results obtained from CMR can be used to select patients likely to benefit from CRT, as well as to guide the implantation of the LV pacing lead in the optimal region (67). Considering that 60,000 new CRT devices are implanted each year and that HF is associated with increased morbidity and decreased survival, there is a need to address the CRT nonresponder problem (68). MRI using cine DENSE, LGE, and coronary vein imaging can assess dyssynchrony, regional mechanical activation time, presence of scar, and potential for CRT lead accessibility (leads are placed in coronary veins). The circumferential uniformity ratio estimated with singular value decomposition (CURE-SVD) (69) is a validated measure for quantifying cardiac discoordination based on regional circumferential strain, and a lower CURE-SVD from DENSE has shown to be strongly associated with the outcomes of CRT patients (2). Alternative CURE-SVD based on FT from bSSFP cine images may be more compatible with an efficient clinical workflow, but the poor reproducibility for segmental strain of FT (11) limits its performance in the CURE-SVD calculation and in CURE-SVD based prognostics.

1.5 Scope of Dissertation

This dissertation focuses on developing deep learning-based methods that estimate intramyocardial motion from contour motion, and validate the models for global and segmental circumferential strain analysis and for clinical prognostication.

As DENSE provides both myocardial contours and accurate intramyocardial tissue displacement measurements, we investigated the use of DENSE data to train a supervised deep network for intramyocardial tissue motion prediction from contours. The trained StrainNet model could then be applied to contours from routine cine bSSFP MRI. In this study, our goal is to use deep learning to improve strain analysis of routine cine MRI, and to demonstrate the advantages of DL-models over conventional feature tracking for prognostication in cardiac resynchronization therapy.

This thesis investigates the use of DENSE data to train a 3D (2D+t) convolutional neural network model called StrainNet for predicting intramyocardial tissue motion and strain from myocardial contours. StrainNet will be trained using DENSE data and applied to cine bSSFP MR images. The results will be validated on both healthy volunteers and patients from multiple sites. The performance of StrainNet will be compared with commercial FT algorithm, with DENSE as the reference (Aim 1). The development of the technique is summarized in *Chapter 2*.

Additionally, a Transformer-based deep neural network, termed TransStrainNet, will be developed to capture the long-distance dependency of the temporal dimension. The Transformer-based network may outperform the convolutional layers by better exploiting both local and global features (Aim 2). The development of the technique is summarized in *Chapter 3*.

Lastly, we will test the hypothesis that TransStrainNet will outperform conventional feature tracking for prognostication on heart failure patients who underwent cardiac

resynchronization therapy (CRT). The outcomes of 6-month post CRT remodeling and 4-year survival will be predicted through a strain-based parameter circumferential uniformity ratio estimated with singular value decomposition (CURE-SVD) (Aim 3). The results of these experiments are summarized in *Chapter 4*.

Chapter 2 – StrainNet

2.1 Introduction

Myocardial strain imaging using cardiac magnetic resonance (CMR) has applications in many types of heart conditions including the detection of chemotherapy-induced cardiotoxicity (1), for optimization of cardiac resynchronization therapy (CRT) (70), for outcome prediction after myocardial infarction (3) and for identification of subclinical cardiac dysfunction in obesity and diabetes (4). CMR methods such as myocardial tagging (5), displacement encoding with stimulated echoes (DENSE) (6, 7), and strain-encoded imaging (8) acquire images specifically designed to measure intramyocardial deformation and strain, and can be referred to as strain-dedicated methods. Alternatively, feature tracking (FT) (9) estimates strain from routine cine balanced steady-state free precession (bSSFP) images. Recent studies that evaluated both DENSE and FT in the settings of acute myocardial infarction and CRT found that DENSE outperformed FT for prognostication (3, 70). Studies in phantoms and humans have shown that DENSE provides accuracy and reproducibility equivalent to or better than tagging (71, 72) (often considered the reference standard), and that DENSE is reproducible for global and segmental strain (10), whereas FT has poor reproducibility for segmental strain (11). While DENSE provides well-validated and more predictive strain than FT, the time needed to acquire DENSE images may not always be compatible with an efficient clinical workflow. A strain method with performance similar to DENSE and the efficiency of FT would be ideal.

Conventional FT utilizes endocardial and epicardial contours and optical flow (9) and/or an incompressibility model (73) to compute intramyocardial displacement; however, these models have limitations when applied to two-dimensional images. Recently, deep learning (DL) has demonstrated better performance for general motion tracking tasks than optical flow (74, 75), and has been introduced for cine bSSFP motion estimation (51-54). However, to date, DL-based

motion estimation for bSSFP has used either unsupervised learning (51, 53, 54) or supervised learning with suboptimal training data (52), providing suboptimal results.

As DENSE provides both myocardial contours and accurate intramyocardial tissue displacement measurements, we investigated the use of DENSE data to train a supervised deep network (StrainNet) for intramyocardial tissue motion prediction from contour motion. Since multiphase endocardial and epicardial contours segmented from DENSE and bSSFP images reflect the same underlying cardiac motion, we reasoned that the model trained using DENSE contours could be applied to contours from bSSFP. We aimed to show that StrainNet analysis of bSSFP images could provide the clinical convenience of FT and better agreement with DENSE.

2.2 Methods

2.2.1 Subjects and Imaging Protocol

Eight centers (University of Virginia, Charlottesville, USA; University Hospital, Saint-Etienne, France; University of Kentucky, Lexington, USA; University of Glasgow, Scotland, UK; St. Francis Hospital, New York, USA; the Royal Brompton Hospital, London, UK; Emory University, Atlanta, USA; and Stanford University, Palo Alto, USA) provided data for this study. 144 healthy volunteers and 161 patient subjects with (a) myocardial infarction ($n = 62$), (b) heart failure with left bundle branch block ($n = 47$), (c) hypertrophic cardiomyopathy ($n = 17$), (d) amyloidosis ($n = 13$), (e) dilated cardiomyopathy ($n = 10$), (f) ischemic heart disease without infarction ($n = 7$), and (g) myocarditis ($n = 5$) were included. Within the 144 healthy volunteers, 45 of them were children ($12.4 \pm 2.7y$). One-hundred and ninety-six datasets were acquired using 3.0 T scanners (MAGNETOM Prisma, Skyra or Trio, Siemens Healthcare, Erlangen, Germany) and 109 were

acquired using 1.5 T scanners (MAGNETOM Aera or Avanto, Siemens Healthcare, Erlangen, Germany).

For each subject, short-axis cine bSSFP images were acquired during repeated breatholds covering the LV (field of view, 320×320 – 380×380 mm²; temporal resolution, 30–55 msec, depending on heart rate). Three–four short-axis cine DENSE slices were also acquired (field of view 200×200 – 360×360 mm²; temporal resolution, 30–34 msec, resulting in 18–43 frames across the cardiac cycle). DENSE images were analyzed using previously described methods. For bSSFP images, the endocardial and epicardial contours were automatically detected and FT was performed using commercial software (SuiteHeart, NeoSoft).

2.2.2 Algorithm Performance Evaluation Using DENSE Contours and DENSE Displacement

The accuracy between the StrainNet-estimated displacement from DENSE contours and DENSE ground truth displacements was assessed using the end-point-error (EPE), defined by:

$$EPE = \frac{1}{n} \sum_{t=1}^n \sqrt{(d_{est}^x(t) - d_{gt}^x(t))^2 + (d_{est}^y(t) - d_{gt}^y(t))^2}.$$

Average EPE within the myocardial region for the whole time series was calculated, where $d_{gt}^x(t)$ and $d_{gt}^y(t)$ are the ground truth displacements from DENSE for the x and y directions at time frame t, respectively, $d_{est}^x(t)$ and $d_{est}^y(t)$ are the StrainNet-estimated displacements, and n is the number of frames.

2.2.3 Deep Learning Architecture

A 3D (2D+t) U-Net (46) was trained to predict intramyocardial displacement from contour data. The network depth was 3 and the numbers of filters were 64, 128, 256 and 512, from the top to the

bottom levels, respectively. The kernel sizes were $3 \times 3 \times 3$ for the convolutional layers and $4 \times 4 \times 2$ for the pooling layers. During training, the U-Net inputs were a time series of myocardial contours derived from DENSE magnitude images and the ground-truth output data were Lagrangian displacement measurements derived from DENSE phase images, with EPE as the loss function. For testing, StrainNet was applied to contours derived from FT software applied to standard bSSFP images, and DENSE at matched slice locations served as the reference (Figure 2-1). Lagrangian strain was computed from StrainNet displacements using the same methods as used for DENSE.

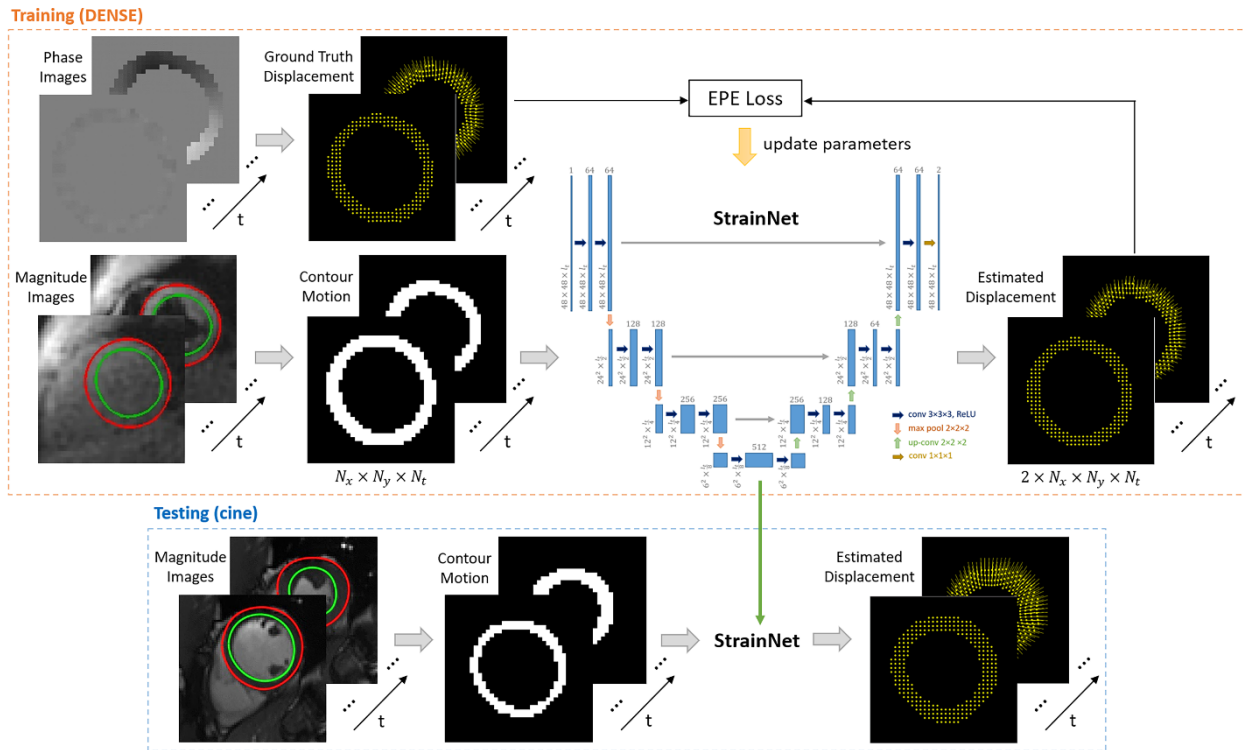


Figure 2-1: Schematic showing the proposed StrainNet to predict intramyocardial displacement from contour motion. A 3D U-net architecture consisting of convolution, batch normalization, ReLU layers, residual connections and pooling layers was used. Our models were trained with the Adam optimizer using a total of 120 epochs. The initial learning rate was set to $1e-4$, with a halving schedule at 20 and 100 epochs. During training, the inputs were a time series of myocardial contours derived from DENSE magnitude images and the ground truth data were displacement

measurements computed from DENSE phase images. End-point-error (EPE) was the loss to calculate the difference between the estimated displacement maps and ground truth DENSE displacements. During testing, the inputs were a time series of myocardial contours derived from routine bSSFP cine images.

2.2.4 Data Pre-processing

After LV segmentation, images were binarized by filling the myocardial area with ones and the non-myocardial area with zeroes. DENSE images were cropped to a fixed size (48×48) which included the LV. Cine images were scaled to match the mean spatial resolution of DENSE (pixel size, $2.73 \times 2.73 \text{ mm}^2$). Morphological dilation was applied to the bSSFP binary mask to approximately match the wall thickness of bSSFP cine MRI and DENSE, and then the mask images were cropped to the same size as the DENSE training data. Data augmentation on-the-fly was performed by random $\pm 90^\circ$ and 180° rotations. The input data for the network was a series of binarized images of LV myocardium of size $N_x \times N_y \times N_t$, with N_t representing the number of temporal frames. The output was the corresponding Lagrangian displacement maps of size $2 \times N_x \times N_y \times N_t$, with the factor of 2 accounting for 2D displacement.

2.2.5 Selection of Training and Independent Testing Datasets

The 305 subjects were randomly divided 80:20 into training and independent testing datasets, and this ratio was applied to each sub-group (healthy adults, healthy pediatrics and each disease type). Basal, mid-level and apical slices were analyzed, resulting in 670 slices from 243 subjects for training and 190 slices from 62 subjects for testing (Figure 2-2). Five-fold cross-validation was applied within the training datasets, and a single final model was trained using all training data with the optimal hyperparameters selected by cross-validation.

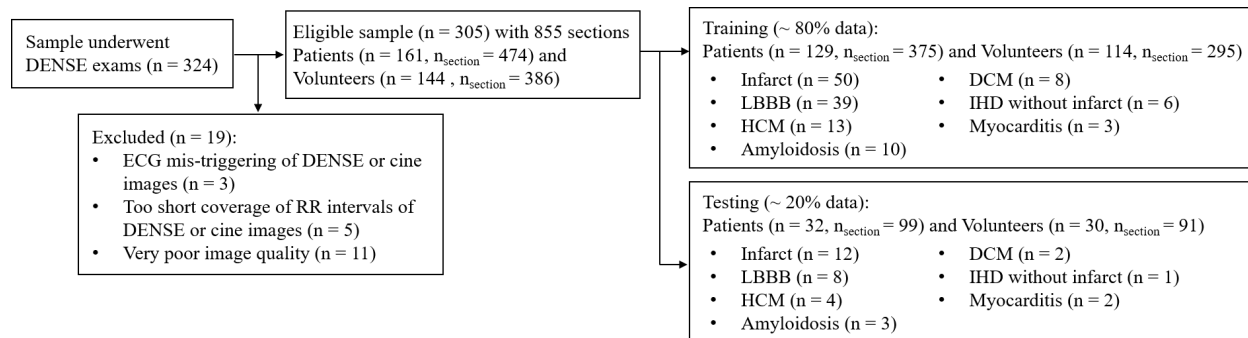


Figure 2-2: Flow diagram showing patient (n = 161) and volunteer (n = 144) datasets. The StrainNet CNN was trained with the DENSE training dataset (80% of study participants), and assessed using an independent testing dataset including DENSE and cine images (20% of study participants).

2.2.6 Statistical Analysis

End-systolic global and segmental circumferential strain (E_{cc}) computed by StrainNet and FT were compared with DENSE using the intra-class correlation coefficient (ICC), Pearson correlation coefficient (Pearson CC), coefficient of variation (CV) and Bland-Altman analysis. Transmural strain differences among the subendocardium, middle layer and subepicardium and strain differences among StrainNet, FT and DENSE for each segment were assessed by linear mixed-effects models. $P < .05$ (two-sided) was considered statistically significant. Statistical analyses were performed using MATLAB R2018b (Mathworks Inc, Natick, MA).

2.3 Results

2.3.1 Examples of End-systolic Displacement and E_{cc} Maps and E_{cc} -time Curves from Volunteers and Heart Disease Patients

Examples of end-systolic displacement and E_{cc} maps from StrainNet processing of bSSFP image contours and from DENSE for a healthy subject and a heart failure patient with left bundle branch block are shown in Figure 2-3 For the healthy subject, qualitatively StrainNet depicted normal

displacement and E_{cc} , in good agreement with DENSE. For the heart failure patient, StrainNet showed simultaneous stretching of the septal segments and contraction of the lateral wall, also with generally good agreement with DENSE.

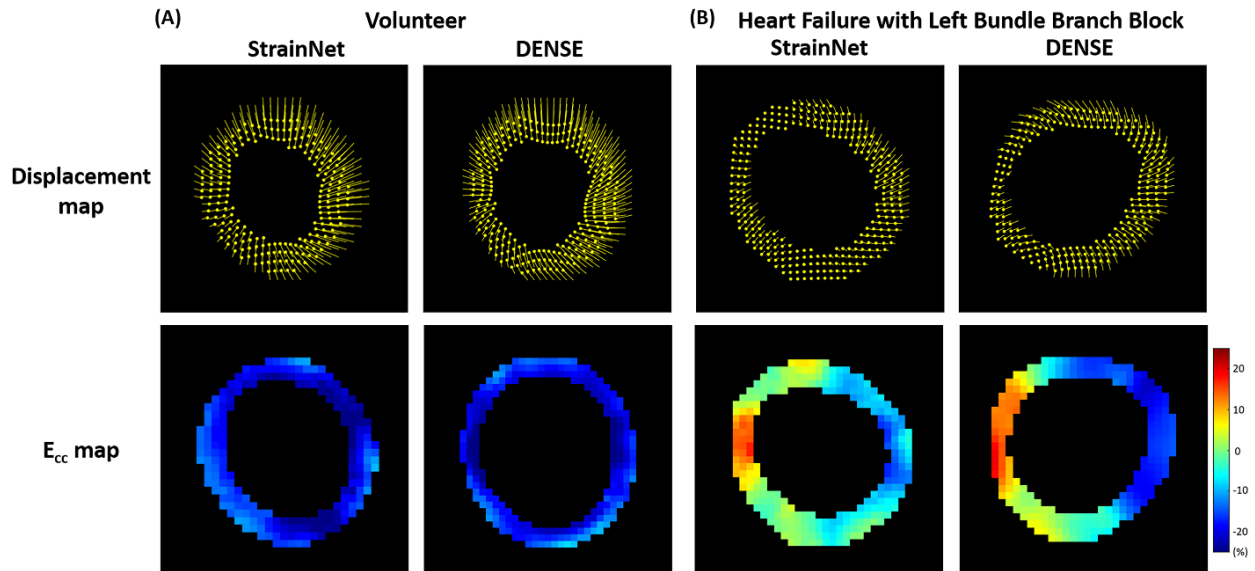


Figure 2-3: Example end-systolic displacement and E_{cc} maps comparing StrainNet analysis of bSSFP cine images and DENSE for (A) a healthy volunteer (female; age, 23 year) and (B) a heart failure patient with left bundle branch block (female; age, 71 year).

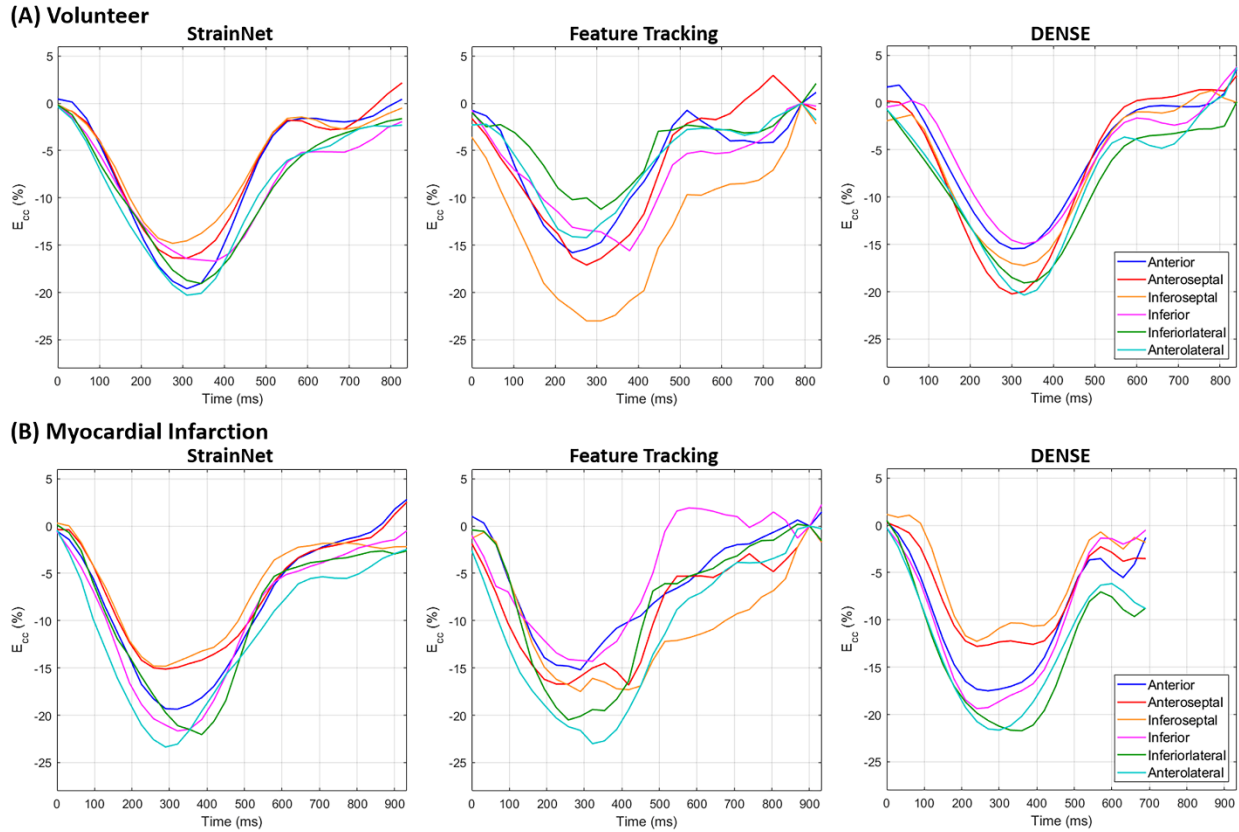


Figure 2-4: Example segmental circumferential strain-time curves for StrainNet analysis of bSSFP cine MRI, FT analysis of bSSFP cine MRI, and DENSE for (A) a healthy volunteer (age, 28 year; female) and (B) a myocardial infarct patient (age, 42 year; male). The healthy volunteer has 30 frames with repetition time (TR) = 32.17ms for bSSFP cine MRI, and 24 frames with TR = 30ms for cine DENSE; the patient has 25 frames with TR = 34.44ms for bSSFP cine MRI, and 29 frames with TR = 30ms for cine DENSE.

Figure 2-4 shows example segmental strain-time curves for a healthy volunteer and a myocardial infarction patient computed using FT, StrainNet processing of standard cine images and DENSE. For the healthy volunteer, qualitatively, segmental strain-time curves computed using StrainNet showed better agreement than FT with DENSE. FT showed more variability, both spatially and temporally than StrainNet and DENSE. For the myocardial infarction patient, both DENSE and StrainNet showed diminished circumferential shortening in the anteroseptal and inferoseptal segments and normal strain elsewhere, whereas FT showed the least amount of

circumferential shortening in the anterior and inferior segments, in disagreement with the reference standard DENSE method.

2.3.2 End-Point-Error

To compute EPE for displacement, where a one-to-one pixel-wise mapping of the StrainNet output to the DENSE displacement field is needed for the calculation, StrainNet was applied to the myocardial contours of DENSE magnitude images. For the independent testing datasets, the average EPE within the myocardium for the whole time series was 0.75 ± 0.35 mm (0.30 ± 0.12 pixels).

2.3.3 Detection of Transmural Strain Gradient

A layer-specific analysis of end-systolic Ecc was performed for the 30 independent testing volunteers, with results shown in Figure 2-5. A transmural gradient of Ecc within the LV myocardial wall was detected by DENSE, StrainNet processing of bSSFP cine images, and FT, and the layer-specific strain values computed using StrainNet displacements showed better agreement than FT with DENSE. The transmural strain gradient is also evident in the volunteer example in Figure 2-3. A slice-by-slice layer-specific analysis for basal, mid-ventricular, and apical slices is provided in Supplementary Table 2-4.

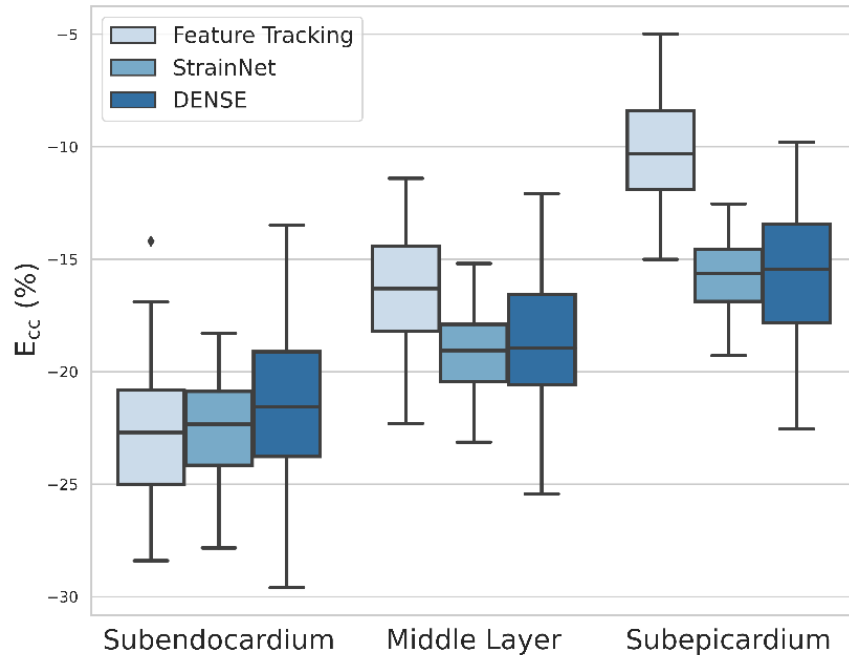


Figure 2-5: Layer-specific E_{cc} measurements for FT analysis of bSSFP cine MRI, StrainNet analysis of bSSFP cine MRI, and DENSE. FT: subendocardium, $-22.88 \pm 2.92\%$; middle layer, $-16.40 \pm 2.54\%$, subepicardium, $-10.13 \pm 2.35\%$, [$P < .001$]. StrainNet: subendocardium, $-22.62 \pm 2.26\%$; middle layer, $-19.20 \pm 1.89\%$; subepicardium, $-15.71 \pm 1.62\%$, [$P < .001$]. DENSE: subendocardium, $-21.60 \pm 3.34\%$; middle layer, $-18.71 \pm 2.92\%$; subepicardium, $-15.75 \pm 2.95\%$, [$P < .001$]. There was significant difference between FT and DENSE for all three layers [$P = .007$ for subendocardium, $P < .001$ for middle layer, and $P < .001$ for subepicardium]; there was significant difference between StrainNet and DENSE for subendocardium [$P = .002$], and no significant difference for middle layer [$P = .09$] and subepicardium [$P = .91$].

2.3.4 Correlations and Agreement of End-systolic E_{cc} between StrainNet, FT, and DENSE

Figure 2-6 shows linear correlations and Bland-Altman plots comparing end-systolic E_{cc} computed using StrainNet and DENSE and computed using FT and DENSE for global and segmental E_{cc} from all three slice positions. The 59 out of 62 independent testing subjects with images from basal, mid-level and apical slices were included. There were no significant differences between

StrainNet and DENSE for end-systolic global E_{cc} [$P=.42$] and segmental E_{cc} [$P=.08$], with the corresponding biases (limits of agreements) of -0.51 ($-5.74, 4.72$) % and -0.55 ($-9.16, 8.07$) %, respectively; whereas there were significant differences between FT and DENSE for global E_{cc} [$P=.003$] and segmental E_{cc} [$P<.001$], with the corresponding biases (limits of agreement) of 1.6 ($-4.97, 8.09$) % and 1.5 ($-12.2, 15.3$) %, respectively.

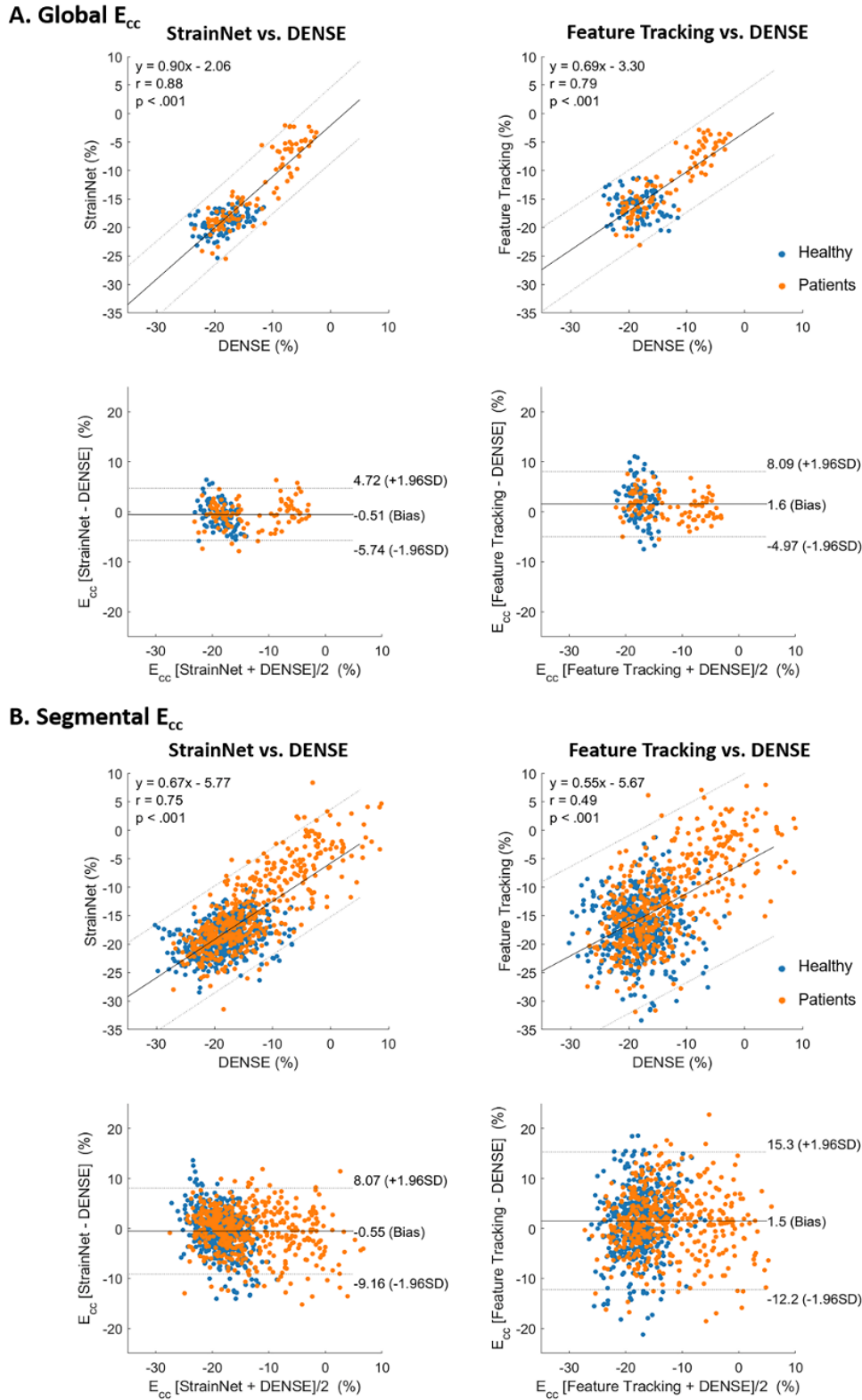


Figure 2-6: Correlation and Bland-Altman plots comparing StrainNet and FT analyses of bSSFP cine MRI with DENSE for end-systolic (A) global and (B) segmental E_{cc} .

Table 2-1: Comparison of agreement of global and segmental E_{cc} for all slices.

	Global E_{cc}		Segmental E_{cc}	
	StrainNet	Feature Tracking	StrainNet	Feature Tracking
ICC	0.87	0.72	0.75	0.48
Pearson CC	0.88	0.79	0.75	0.49
CV	13.42	17.73	22.22	36.42
Bias \pm 95% Limits	-0.51 ± 5.15	1.62 ± 6.64	-0.55 ± 8.61	1.53 ± 13.75

Table 2-2: Comparison of agreement of per-slice global and segmental E_{cc} .

	Global E_{cc}		Segmental E_{cc}	
	StrainNet	Feature Tracking	StrainNet	Feature Tracking
Basal				
ICC	0.80	0.76	0.67	0.43
Pearson CC	0.85	0.78	0.71	0.45
CV	15.08	15.18	26.49	40.68
Bias \pm 95%Limits	-1.66 ± 4.63	-0.88 ± 5.68	-1.71 ± 8.89	-0.79 ± 15.20
Mid-level				
ICC	0.92	0.83	0.79	0.56
Pearson CC	0.92	0.92	0.79	0.59
CV	11.84	18.38	23.89	38.92
Bias \pm 95%Limits	0.33 ± 4.51	2.25 ± 4.37	0.31 ± 8.75	2.35 ± 12.70
Apical				
ICC	0.88	0.67	0.78	0.56
Pearson CC	0.88	0.81	0.78	0.63
CV	14.45	3.31	20.65	30.41
Bias \pm 95%Limits	-0.24 ± 5.72	3.31 ± 6.58	-0.27 ± 8.51	3.43 ± 10.89

Note. -ICC = Intra-class correlation coefficient, Pearson CC = Pearson correlation coefficient, CV = Coefficient of Variation.

Table 2-1 summarizes ICC, Pearson CC, CV and the corresponding biases and limits of agreement results comparing FT and StrainNet to DENSE for the assessment of global and segmental E_{cc} . The ICCs between StrainNet and DENSE and FT and DENSE were 0.87 vs. 0.72, respectively, for global E_{cc} and 0.75 vs. 0.48, respectively, for segmental E_{cc} , showing that StrainNet showed good agreement with DENSE and outperformed FT for both global and segmental E_{cc} . Table 2-2 summarizes per-slice quantitative results for global and segmental E_{cc} for basal, mid-level and apical slices respectively, showing StrainNet had better correlation and less variation from DENSE for basal, mid-level and apical slices, and smaller biases for mid and apical slices.

Bull's eye plots shown in Figure 2-7 summarize per-segment ICC, CV, bias, and 95% limits of agreement between StrainNet and DENSE and between FT and DENSE. StrainNet showed better agreement with DENSE and less bias for all metrics.

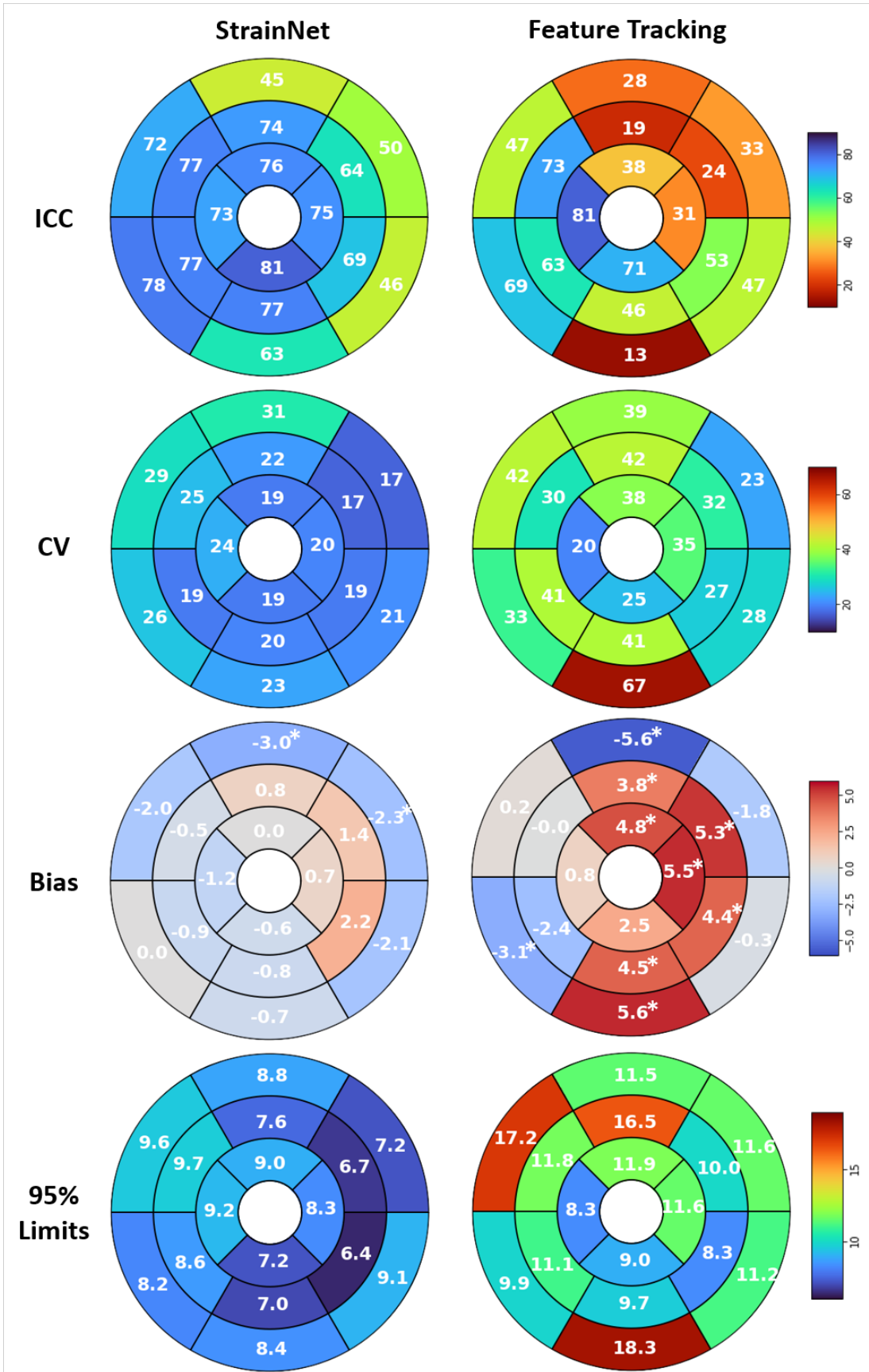


Figure 2-7: Bull’s eye plots of per-segment E_{cc} for intraclass correlation coefficient (ICC, %), coefficient of variation (CV), bias and limits of agreements comparing StrainNet and FT with DENSE. A linear mixed-effects model was performed over techniques for each segment, and an asterisk in the bias column was indicated as having statistical significance with reference DENSE.

2.4 Discussion

While strain-dedicated methods such as DENSE provide the most accurate assessment of global and segmental strain, in busy clinical settings it may not always be practical to add strain-dedicated acquisitions to the CMR protocol. The ability to perform strain analysis of routine bSSFP cine images supports an efficient clinical workflow, and DL-models trained on strain-dedicated data may provide a means to outperform conventional FT for this task. In our study, we leveraged DENSE data from more than 300 subjects to develop a DL framework that can predict intramyocardial displacement from myocardial contours and showed that the resulting 3D U-net, StrainNet, can be successfully used for strain analysis of standard cine images. There are several major findings of our study. First, for both healthy volunteers and patients, StrainNet predicts intramyocardial displacement and strain from myocardial contour motion and shows good agreement with DENSE. Second, for the analysis of routine cine MRI, StrainNet shows better agreement than FT with DENSE for global and segmental circumferential strain. Additional conclusions are: a) StrainNet is effective when applied to contours from either DENSE images or cine images; b) StrainNet showed good reliability for segmental E_{cc} with an ICC over 0.75 for mid-ventricular and apical slices; and c) transmural layer-specific E_{cc} measurements using StrainNet were more consistent than FT with DENSE.

Learning-based myocardial motion tracking methods have been investigated previously (51-54) and demonstrated the potential for high performance that ought to be achievable by

leveraging big data and the ability of convolutional neural networks to extract intangible and multi-scale features. The main challenge in the development of motion tracking methods using deep learning is the lack of ground-truth data (52). Previous studies have shown the feasibility of regional strain assessment by deep learning using cine MR images, but they used classical optical-flow to generate the motion ground truth (52) or unsupervised loss functions during training (51, 53, 54). Our study benefitted from the availability of multi-center DENSE datasets from 305 subjects with healthy hearts and various types of heart diseases, and from the strong correspondence of the depiction of heart motion between DENSE and standard cine images allowing us to generate accurate displacements, global E_{cc} and segmental E_{cc} from routine cine MRI. StrainNet performance benefitted from diversity of the data including multiple diseases, multiple data acquisition sites, multiple observers for data post-processing, a wide range of ages (adults and pediatrics), and different magnetic field strengths (1.5T and 3T). Since cine MRI and cine DENSE generally have similar temporal resolution, we found that no additional manipulation was needed to handle variability in temporal resolution or number of cardiac phases. Compared with previous DL-based cardiac motion tracking networks, our supervised learning framework took advantage of the accuracy of DENSE, resulting in a lower average EPE of 0.75 ± 0.35 mm compared to previously reported DL-based motion tracking results of 2.9 ± 1.5 mm (51) and 0.94 ± 1.59 mm (52).

Our study had several limitations. First, additional work is needed to improve the performance of StrainNet in analyzing the basal slice as it is not as fully optimized as that for the mid-level and apical slices. We believe it is the segmentation error for the basal slices that has to be corrected to improve the output from StrainNet. Second, future work should focus on training StrainNet using long-axis DENSE data to predict 2D displacement in these planes to facilitate the

computation of longitudinal strain. Lastly, the current study did not consider radial strain (Err). Presently neither StrainNet nor FT show good agreement with DENSE for radial strain (64), thus more development is needed before comparing radial strain results generated by the various methods.

In the future, StrainNet could likely be improved by further increasing the size and diversity of the training data set and retraining the network. With the sound framework of StrainNet applied to contoured images of the heart proved by the current work, we will investigate the application of the network to other modalities such as cardiac CT and echocardiography cine images. Along these lines, StrainNet provides the potential to standardize strain values across different imaging modalities.

In conclusion, using data from healthy adult and pediatric volunteers and adults with various types of heart disease, a deep learning framework to accurately predict intramyocardial motion from contour motion was developed. Its application to standard cine MRI showed better agreement than FT for the quantification of global and segmental circumferential strain using DENSE as the reference standard. This approach enables strain analysis of routine cine MRI with accuracy similar to strain-dedicated DENSE. StrainNet may facilitate greater use of strain CMR in research and in the clinical setting.

2.5 Appendix

2.5.1 Demographic Information of the Dataset

Table 2-3 Supplementary: Demographic information and left ventricular volumetric data for patients and volunteers.

	Training				Testing			
	Patients (n=129)	Adult volunteers (n=78)	Pediatric volunteers (n=36)	p value ⁴	Patients (n=32)	Adult volunteers (n=21)	Pediatric volunteers (n=9)	P value ⁴
Male	87 (67.4%)	31 (39.7%)	17 (47.2%)	<.001	22 (68.8%)	13 (61.9%)	4 (44.4%)	0.61
Age (y)	61.8 ± 12.8	36.7 ± 15.6	12.4 ± 2.8	<.001	58.9 ± 17.6	27.9 ± 7.9	12.4 ± 2.6	<.001
Height (cm)	169.5 ± 10.4	170.8 ± 9.5	155.1 ± 12.7	0.016	168.1 ± 21.1	172.1 ± 11.6	164.7 ± 18.2	0.44
Weight (kg)	79.8 ± 16.6	68.5 ± 14.5	59.8 ± 22.3	<.001	81.1 ± 23.7	71.6 ± 17.3	63.5 ± 18.0	0.12
LVEDV (mL)¹	177.5 ± 75.9	138.7 ± 34.0	130.5 ± 30.4	0.003	185.9 ± 73.3	156.3 ± 35.0	147.2 ± 33.9	0.23
LVESV (mL)¹	104.0 ± 74.7	59.8 ± 17.5	50.2 ± 13.9	<.001	107.7 ± 76.2	73.5 ± 18.1	56.1 ± 15.8	0.15
LVEF (%)¹	41.1 ± 17.1	56.9 ± 4.9	61.9 ± 4.0	<.001	43.2 ± 18.0	53.0 ± 3.7	62.2 ± 3.7	0.28
HR (BPM)²	72.3 ± 13.4	66.3 ± 12.5	72.3 ± 8.8	0.024	74.9 ± 14.0	74.6 ± 10.1	72.1 ± 10.0	0.94
SV (mL/m²)¹	73.5 ± 24.9	79.0 ± 21.1	80.4 ± 18.1	0.23	78.2 ± 18.9	82.8 ± 19.0	91.2 ± 19.3	0.48
CO (L/min)²	5.4 ± 1.9	5.2 ± 1.5	5.7 ± 1.1	0.75	6.3 ± 1.7	5.8 ± 1.2	6.5 ± 1.0	0.45
BP Dias (mmHg)³	75.0 ± 14.9	72.1 ± 9.8	70.8 ± 7.0	0.43	78.3 ± 6.7	73.7 ± 10.4	73.3 ± 7.2	0.28

BP Sys (mmHg)³	127.5 ± 24.0	122.9 ± 13.1	109.1 ± 12.7	0.42	127.6 ± 17.5	122.1 ± 15.0	116.2 ± 3.9	0.43
--------------------------------------	-----------------	-----------------	-----------------	------	-----------------	-----------------	-------------	------

Note. -Unless otherwise indicated, data are means ± standard deviations. Independent t tests were used to compare the differences between two groups for continuous numerical variables. LVEDV = Left ventricular end-diastolic volume, LVESV = Left ventricular end-systolic volume, LVEF = Left ventricular ejection fraction, HR = Heart rate, SV = Stroke volume, CO = Cardiac output, BP Dias = Diastolic blood pressure, BP Sys = Systolic blood pressure.

¹Data are from all patients and 91 volunteers.

²Data are from 105 patients and 97 volunteers.

³Data are from 51 patients and 86 volunteers.

⁴p values are calculated between patients and adult volunteers.

2.5.2 Correlation and Bland-Altman Plots of StrainNet and FT Analyses of Basal Cine bSSFP Slices with DENSE

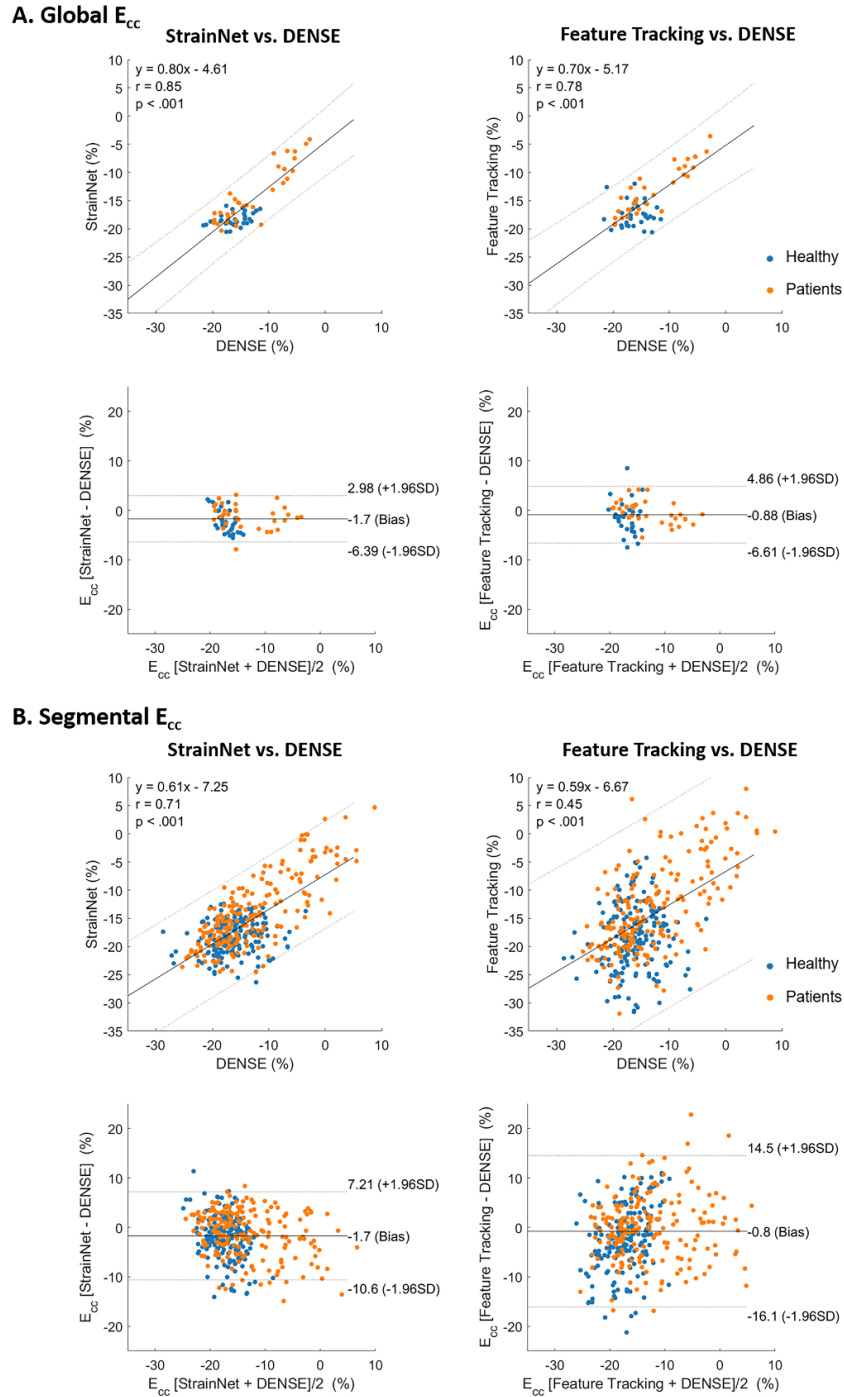


Figure 2-8 Supplementary: Correlation and Bland-Altman plots of StrainNet and FT analyses of basal cine bSSFP slices with DENSE for end-systolic (A) global and (B) segmental E_{cc} .

2.5.3 Correlation and Bland-Altman Plots of StrainNet and FT Analyses of Mid-ventricular Cine bSSFP Slices with DENSE

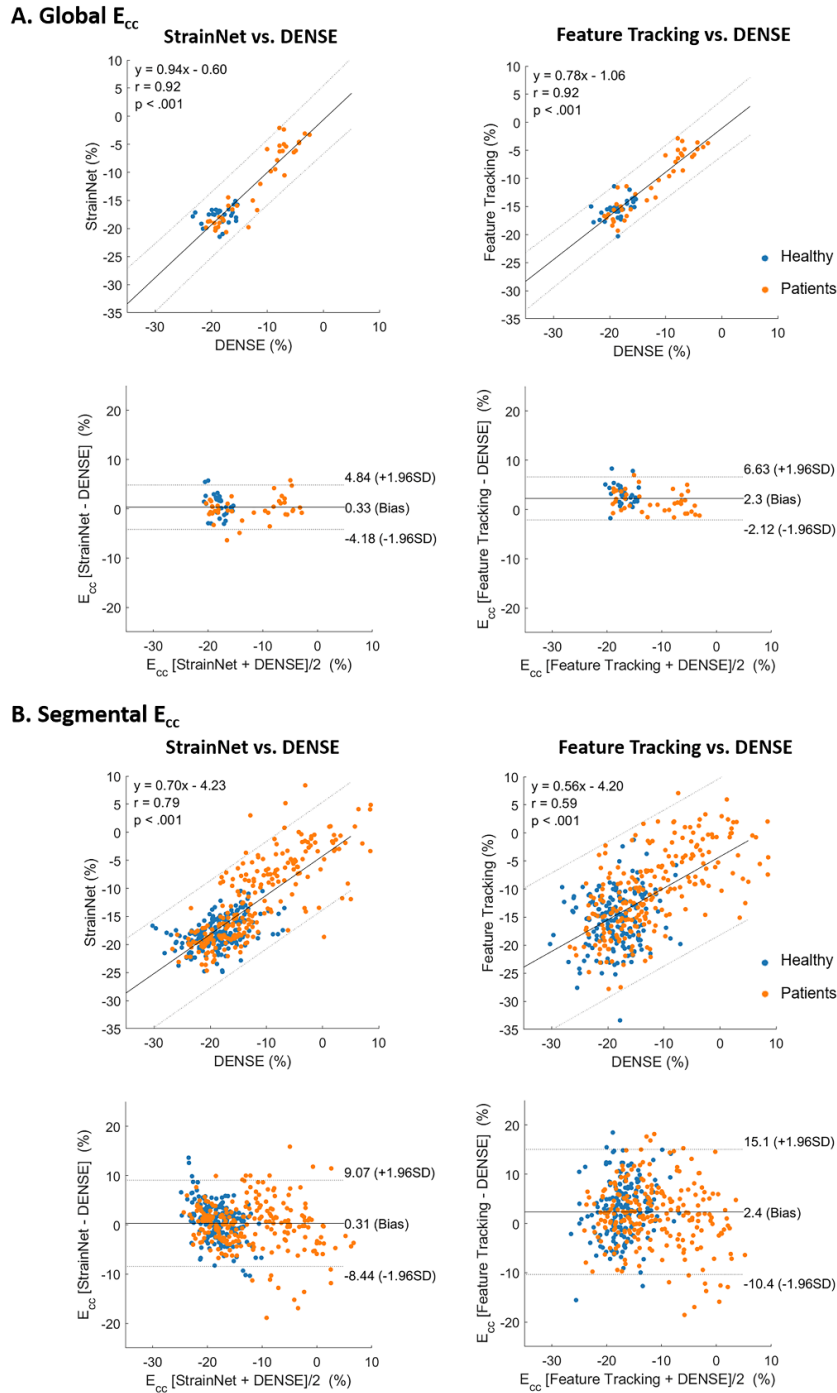


Figure 2-9 Supplementary: Correlation and Bland-Altman plots of StrainNet and FT analyses of mid-ventricular cine bSSFP slices with DENSE for end-systolic (A) global and (B) segmental E_{cc} .

2.5.4 Correlation and Bland-Altman Plots of StrainNet and FT Analyses of Apical Cine bSSFP Slices with DENSE

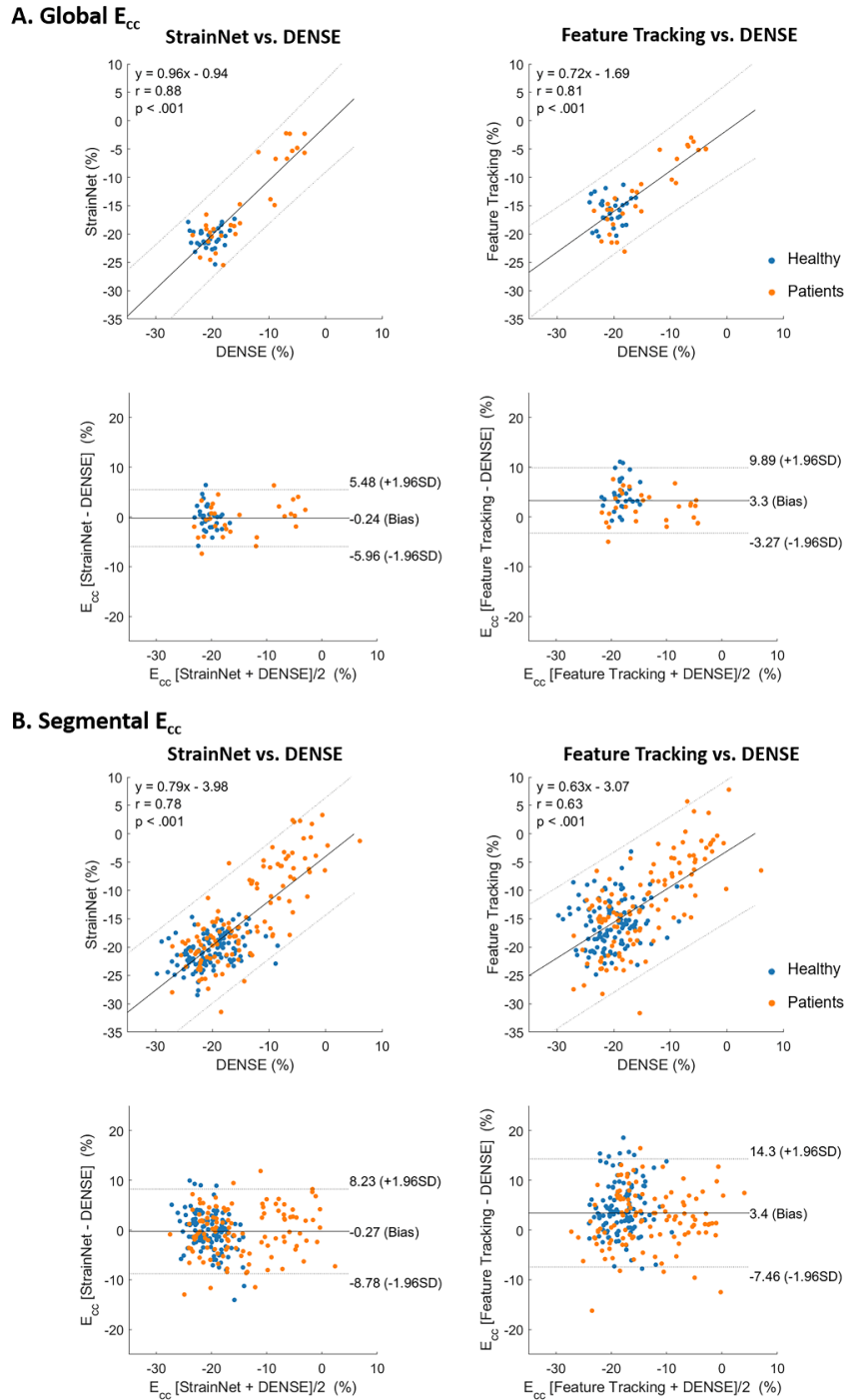


Figure 2-10 Supplementary: Correlation and Bland-Altman plots of StrainNet and FT analyses of apical cine bSSFP slices with DENSE for end-systolic (A) global and (B) segmental E_{cc} .

2.5.5 Comparison of Layer-specific End-systolic E_{cc} (%) among FT, StrainNet and DENSE for Basal, Mid-level and Apical Slices

Table 2-4 Supplementary: Comparison of Layer-specific End-systolic E_{cc} (%) among FT, StrainNet and DENSE

	Subendocardium	Middle Layer	Subepicardium
Basal			
Feature Tracking	-23.94 ± 2.94	-18.09 ± 2.20	-11.41 ± 2.09
StrainNet	-21.83 ± 1.48	-18.73 ± 1.26	-15.40 ± 1.15
DENSE	-19.00 ± 2.87	-16.41 ± 2.50	-13.68 ± 2.36
Mid-level			
Feature Tracking	-21.45 ± 2.28	-15.39 ± 1.87	-9.73 ± 1.86
StrainNet	-21.36 ± 1.74	-18.10 ± 1.70	-14.82 ± 1.54
DENSE	-21.64 ± 2.34	-18.86 ± 2.04	-15.85 ± 2.50
Apical			
Feature Tracking	-23.25 ± 2.98	-15.71 ± 2.63	-9.23 ± 2.55
StrainNet	-24.73 ± 1.92	-20.81 ± 1.55	-16.97 ± 1.36
DENSE	-24.24 ± 2.55	-20.92 ± 2.30	-17.78 ± 2.52

2.5.6 Full Details of Cine and DENSE Imaging Parameters

For each sample, short-axis cine bSSFP images were acquired during repeated breath holds covering the whole left ventricle. Typical imaging parameters were as follows: repetition time,

3.0–3.4 msec; echo time, 1.5–1.7 msec; matrix size, 192×224 – 224×256 ; field of view, 320×320 – 380×380 mm²; and temporal resolution, 30–55 msec, depending on heart rate.

For each sample, 3–4 short-axis cine DENSE sections were also acquired. Typical DENSE imaging parameters were as follows: repetition time, 15–17 msec; echo time, 1.06–1.26 msec; pixel size, 1.56×1.56 – 3.13×3.13 mm²; matrix size, 64×64 – 128×128 ; field of view 200×200 – 360×360 mm²; temporal resolution, 30–34 msec (resulting in 18–43 frames across the cardiac cycle); region of signal generation, 120×120 – 360×360 mm²; 1D or 2D in-plane displacement encoding using the simple three-point method; displacement-encoding frequency, 0.1 cycles/mm, ramped flip angle with final flip angle of 15°, fat suppression, and 4–6 spiral interleaves per image with 2 interleaves acquired per heartbeat. Each cine DENSE acquisition was performed during end-expiratory breath-holding over 14 cardiac cycles.

Chapter 3 – TransStrainNet

3.1 Introduction

The 3D (2D + t) U-Net has a relatively small receptive field which may limit its accuracy for modeling time-series data, especially to learn long-range dependencies such as those that may be present in cine CMR of the heart (76). As an example of a long-range dependency in cine CMR, consider left bundle branch block, where stretch occurring early in the cardiac cycle is closely associated with a stronger and later end-systolic contraction. While recurrent neural networks (RNNs) (59) and long short-term memory (LSTM) (77, 78) were developed for time-series data, the state-of-the-art transformer model can outperform RNNs and LSTM for time-series data, particularly when long-range dependencies are important (79). Unlike models that process data sequentially, the transformer takes the entire sequence of data as input and uses self-attention mechanisms to learn relationships in the sequence. We note that for modeling cardiac motion, the attention mechanism (49) may be particularly well suited, as key phases in the cardiac cycle should likely be emphasized. As examples of key phases, end-systole marks a change from contraction to relaxation, the onset of shortening marks a change from diastasis or prestretch to contraction, and the end of early diastole marks a change from rapid relaxation to diastasis. Because of the self-attention mechanism and the ability to model long-range dependencies, we propose that the transformer is well suited for modeling the complex dynamics of physiological and pathophysiological heart motion, thus we will develop a transformer-based version of StrainNet, termed TransStrainNet.

3.2 Methods

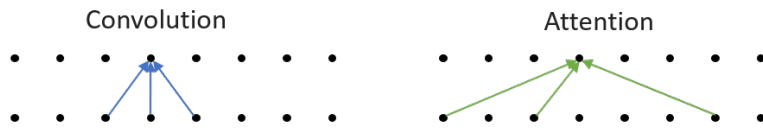
3.2.1 Convolution vs. Attention

StrainNet is a recently-developed convolutional deep learning model trained with displacement encoding with stimulated echoes (DENSE) data to predict intramyocardial motion and strain from myocardial contours of routine cardiac cine MRI (61). While StrainNet provides good-to-excellent strain agreement with DENSE (ICC: 0.87 whole-slice, 0.75 segmental), performance for the subgroup of patients with left bundle branch block (LBBB) and dyssynchrony was worse. The locality of convolutional neural networks (CNNs) may limit their ability to capture long-range dependencies/associations of cardiac motion. Hence, we investigated the use of Transformers (48, 49), known for modeling long-range dependencies, to develop the next generation of StrainNet, termed TransStrainNet. We were particularly interested in the context of mechanical dyssynchrony, as these patients display simultaneous septal stretching and lateral wall contraction, a long-range spatial dependency, as well as the sequence of lateral wall prestretch with a later strong contraction, a long-range temporal dependency. Figure 3-1A compares convolution and attention mechanism in terms of 2D pixels. Compared with convolution which only look at the surrounding pixels, self-attention allows the receptive field to be the entire spatial locations. Therefore, it enables the modeling of long-term dependencies. Figure 3-1B compares the convolutional approaches with Transformer-based methods in the context of cardiac motion, specifically examining long-term dependencies in heart motion for a heart failure patient with LBBB. The study underscores the significance of capturing both spatial and temporal long-term dependencies prevalent in mechanical dyssynchrony observed in such patients. Convolution, due to its localized receptive field, as delineated by the blue box, can only process information from

adjacent areas. This limits its ability to capture the broader spatial dynamics within the cardiac cycle, such as the compensatory mechanisms between septal stretching and lateral wall contraction seen in LBBB. On the contrary, the Transformer's attention mechanism, represented by the green box, offers a substantially larger receptive field, enabling the model to recognize and integrate these complex spatial relationships over greater distances within the myocardium.

For the strain-time curves, the temporal dimension of long-term dependencies becomes apparent. The attention mechanism's capacity to evaluate the entire temporal context allows it to detect the sequence of the lateral wall's pre-stretch phase followed by a strong contraction. This temporal pattern is crucial for understanding the heart's mechanical dyssynchrony in LBBB patients, as it provides insights into the interplay between different regions of the heart muscle over time. The ability of Transformer models to capture such long-term dependencies both spatially and temporally positions them as potentially powerful tools for analyzing complex physiological phenomena and could lead to improved diagnostic and therapeutic strategies for heart failure patients with LBBB.

A. Convolution vs Attention



B. Long-term Dependencies in Heart Motion: An Heart Failure Patient with LBBB

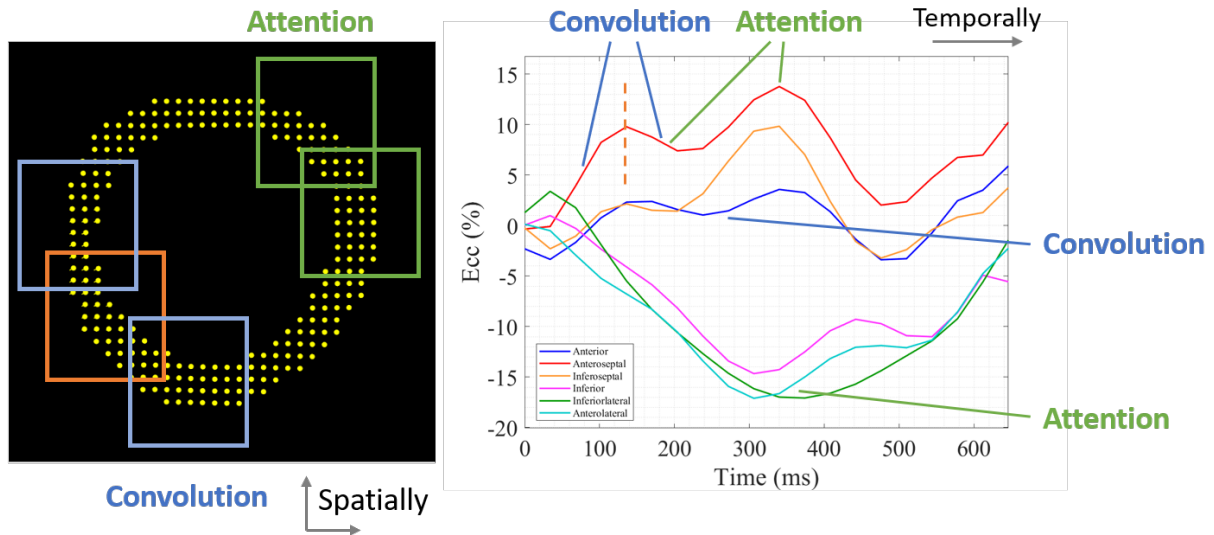


Figure 3-1: Illustration and Comparison of Convolution and Attention Mechanisms. (A) illustrates the fundamental differences between convolution and attention mechanisms. Convolution, depicted by the blue arrows, focuses on local regions, processing information in a confined receptive field. In contrast, the attention mechanism, indicated by green arrows, captures dependencies over larger distances, allowing a broader context to be considered in the analysis. (B) contrasts the ability of convolution and attention mechanisms to capture long-term dependencies in cardiac motion. The orange box at the septum highlights the area of interest. Convolution, marked by the blue box, is limited to immediate surroundings, while attention, shown by the green box, encompasses a wider field, capturing the compensatory relationship between septal stretching and lateral contraction. The strain-time curve further demonstrates the attention mechanism's capacity to discern temporal long-term dependencies, such as the sequence of the lateral wall's prestretch and subsequent contraction.

3.2.2 Transformer with Self-attention Mechanisms

Previously, a sequence is normally compressed into a fixed length vector and information may be lost in the compression especially for long input sequences. Attention mechanism relates different positions of a single sequence to compute a presentation of the sequence. An attention function could be described as the mapping between a query vector and a set of key-value pairs to an output (80). The output is the weighted sum of the values where the weight assigned to each value is computed by a similarity function between the input query and the corresponding key. The attention function can be computed as the following equation:

$$Attention(Q, K, V) = softmax\left(\frac{QK^T}{\sqrt{d_k}}\right)V$$

where Q is the query matrix, K is the key matrix and V is the value matrix. A scaling factor $\frac{1}{\sqrt{d_k}}$ is applied, where d_k is the dimension of key matrix. Self-attention is an attention mechanism that also pay attention to the relativities within encoder and decoder themselves in addition to encoder-decoder attention. Although convolutional architectures remain dominant in vision tasks, multiple works have shown great promises by applying transformers with self-attention to images (48, 76, 81).

Figure 3-2 provides an overall illustration of the Transformer architecture. The Transformer encoder consists of several identical layers stacked together. Each of these layers comprises two distinct sublayers: a multi-head self-attention mechanism and a position-wise feed-forward network. In the encoder's self-attention process, the queries, keys, and values all originate from the outputs of the preceding layer in the encoder, and both sublayers are encircled by a residual connection. This addition from the residual is followed by layer normalization, enhancing the model's stability and performance.

Similarly, the Transformer decoder is built from multiple identical layers with residual connections and layer normalizations. In addition to the two sublayers in the encoder, the decoder introduces an additional sublayer, termed encoder-decoder attention. In this cross-attention, the queries are from the decoder's self-attention, while the keys and values are sourced from the encoder's outputs.

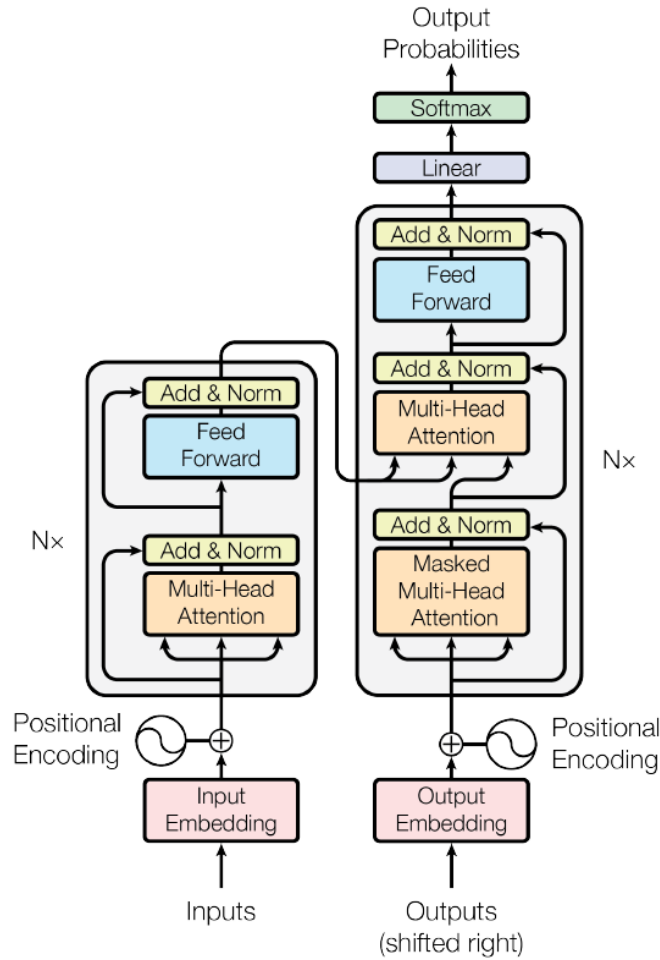


Figure 3-2: Illustration of the encoder-decoder structure of the Transformer architecture.

Figure source: *Attention is All You Need (49)*.

3.2.3 Transformer with 3D Patches as Inputs

As typical for biomedical imaging processing, we will employ the encoder-decoder scheme. The encoder will compress the input into a latent-space representation containing high-level features, and the decoder will predict the output from the latent vector. A vision transformer block will be used as an embedding for global self-attention due to its abilities for compression, time-series modeling and for capturing long-range dependencies and global features. A standard transformer will receive the input as a 1D sequence of token embeddings. However, in order to simultaneously explore the long-term dependency of spatial and temporal dimensions, we design to directly feed Transformer with 3D patches. For 3D images, the $(2D+t)$ input volume will be reshaped into a sequence of flattened patches, and project the patches into a constant latent vector space by a linear layer. To directly process the 3D patches, 3D Transformer blocks would be used as the backbone. After the linear projection of the patches, position embeddings will be combined with patch embeddings to preserve positional information, which will then serve as the input to the transformer blocks. The transformer block consists of alternating multiheaded self-attention (MSA) and feed-forward (FF) layers. LayerNorm (LN) will be applied before each MSA and FF, and skip connections will be used to connect LN and MSA layers and LN and FF layers (49). These elements are used to achieve long-term dependencies among temporal feature maps within the latent space. To project the latent features back to the original image size, a CNN decoder will be applied after the Transformer blocks. The decoded output will finally be fed into a $1 \times 1 \times 1$ convolutional layer to generate the two-channel pixel-wise semantic predictions of displacement maps, with the two maps representing the x and y directions, respectively.

3.2.4 Swin Transformer Blocks

While Vision Transformer (ViT) has achieved superior performance on various vision tasks, adapting the high performance of Transformer from language models to visual tasks faces certain difficulties. One major distinction lies in the significantly higher resolution of pixels in images or voxels in volumetric images, relative to the number of words in text contexts. For example, in the motion estimation tasks explored by this dissertation, dense displacement estimation that requires the prediction at per-pixel level will impose huge computation burden for Transformer models because the complexity of self-attention is quadratic to image size. To enable practical model training, Swin Transformer, a more suitable general-purpose architecture for vision tasks, will be used as the backbone.

There are two key concepts introduced in Swin Transformer to address the issues faced by the original ViT - hierarchical feature maps and shifted window attention.

Hierarchical structure is one of the vital designs in vision models where shallower layers learn more local features and deeper layers capture more abstracted and high-level information. Standard transformer blocks need additional pooling layers to resize the feature maps to achieve hierarchical architecture, such as the deconvolutional layers demonstrated in the previous section. To expand the applicability of transformers and use it as a more general-purpose backbone for vision tasks, the Hierarchical Vision Transformer using Shifted Windows (Swin Transformer) (81) is adopted. Due to its hierarchical design by patch merging and expanding, the Swin Transformer could be easily incorporated into a Unet architecture without the assistant of additional sampling layers. Patch merging is used for down-sampling where the input features of each group are concatenated depth-wise which effectively downsample the input size, and projected by a linear layer. Patch expanding, in reverse, will up-sample the compressed features into higher resolutions.

For the shifted window part, rather than the standard MSA used in ViT, Swin Transformer architecture uses a Window MSA (W-MSA) and a Shifted Window MSA (SW-MSA) module as shown in Figure 3.3B. The typical MSA mechanism computes global self-attention, establishing connections between each patch and every other patch. Consequently, this leads to a computational complexity that is quadratic in relation to the patch count, rendering it inefficient for processing high-resolution images.

The proposed StrainNet with Swin Transformer method is shown schematically in Figure 3-3. The innovation contribution is the combination of 3D U-Net and Swin Transformer block, which facilitates effective and simultaneous exploitation of long-term dependencies of spatiotemporal features. Different patch embedding size, embedding dimensions, shifted-window size, number of multi-heads and number of hierarchical levels will be optimized. Due to the difference of spatial and temporal sizes, isotropic hyperparameters will be designed for spatial and temporal respectively. The Swin Transformer blocks were modified to use both multi-layer perceptron (MLP) and convolutional layers as the feedforward layer to incorporate convolution within the attention blocks rather than only using MLPs. The network depth was 3 and the number of filters was 48. Patch merging was used for down-sampling where the input features of each group of $2 \times 2 \times 2$ were concatenated depth-wise and projected by a linear layer. Patch expanding, in reverse, up-sampled the compressed features by $2 \times 2 \times 2$. The depths of each Swin Transformer stage were 2, 4 and 2, and the number of multi-heads were 3, 6 and 12, from the top to bottom levels, respectively. The window size for Swin Transformer blocks was 3 for spatial dimensions and 2 for the temporal dimension.

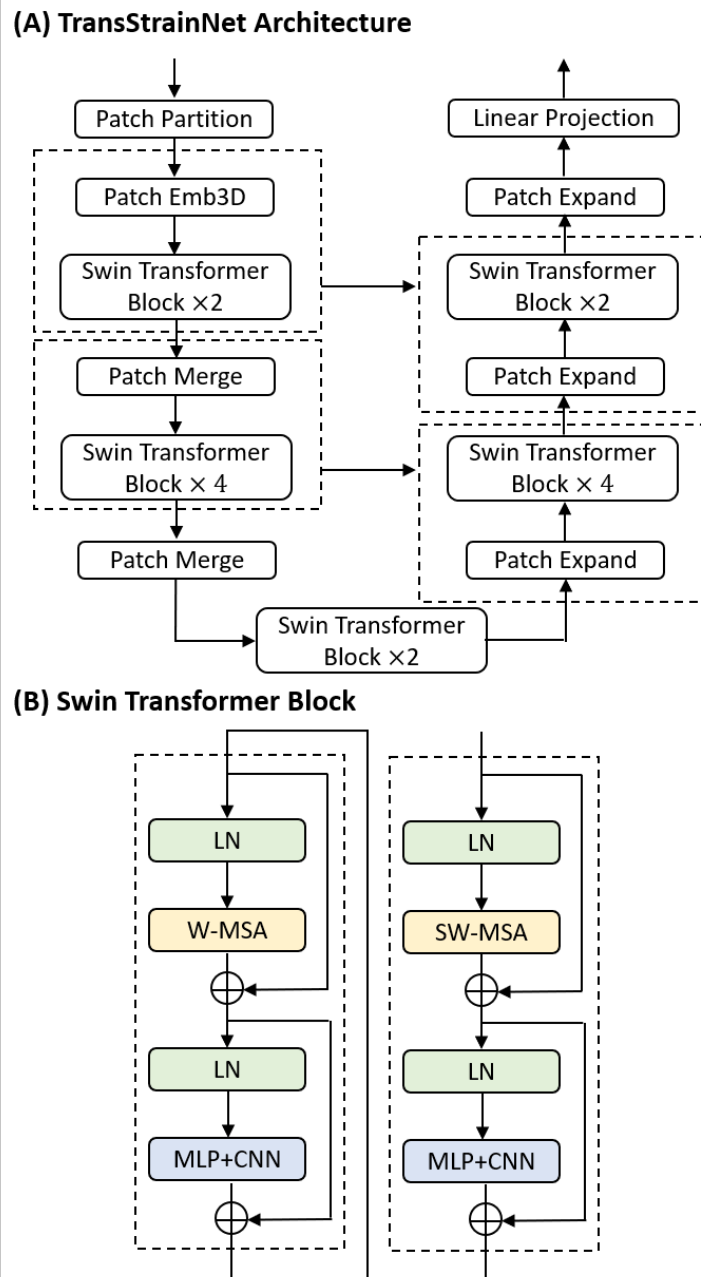


Figure 3-3: General description of Swin transformer-based StrainNet architecture. Encoder, decoder and bottleneck are all composed of 3D (2D+t) Swin transformer blocks. Patch merging and expanding were used to provide the hierarchical architecture, and the encoder latent features were skip connected to decoder features to compose an UNet architecture. Patch merging was used for down-sampling where the input features of each group of $2 \times 2 \times 2$ are concatenated and projected by a linear layer. Patch expanding, in reverse, up-sampled the compressed features into higher resolutions. Our model was trained with the AdamW optimizer using a total of 200 epochs.

The initial learning rate was set to $1e-4$, with a halving schedule every 50 epochs. During training, the inputs were a time series of myocardial contours derived from DENSE magnitude images and the ground truth data were tissue displacement measurements computed from DENSE phase images. End-point-error (EPE) was the loss to calculate the difference between the estimated displacement maps and ground truth DENSE displacements. During testing, the inputs were a time series of myocardial contours derived from routine bSSFP cine images. DENSE data at matched slice locations served as the reference.

3.2.5 Model Training and Testing

The model was trained with myocardial contours from DENSE magnitude images with ground truth as the Lagrangian displacement from DENSE phase images. The inputs were a time series of binarized LV myocardium images and the outputs were the corresponding estimated intramyocardial displacement maps. Data augmentation on-the-fly was performed by random $\pm 90^\circ$ and 180° rotations. The loss function was defined by the average end-point-error within the myocardial region for the whole time series between the estimated displacements and the ground truth DENSE displacements. For testing, TransStrainNet was applied to contours derived from the segmentation of routine cine MRI, and DENSE at matched section locations served as the reference.

Same datasets will be used for StrainNet-Transformer and StrainNet-Unet training and testing as demonstrated in Aim1. The network was trained and tested on the general dataset containing a total of 305 healthy controls and patients with various types of heart diseases, and with a train-test split of 4:1.

3.2.6 Model Performance Evaluation

End-systolic global and segmental circumferential strain (E_{cc}) computed by TransStrainNet and StrainNet were compared with DENSE using the intra-class correlation coefficient (ICC). The

whole E_{cc} -time curve differences between TransStrainNet and DENSE and between StrainNet and DENSE were assessed by root-mean-square-error (RMSE) averaged for each time point. The E_{cc} -time curves from bSSFP cines were interpolated to match with DENSE temporal resolution and the longer E_{cc} -time curves were truncated by the minimum time length of cine MRI and DENSE acquisitions.

3.3 Results

3.3.1 Computation Time

TransStrainNet training and testing were performed with PyTorch on a 24G GPU server (Quadro RTX 6000; NVIDIA). Testing on one slice with the entire cardiac cycle was accomplished in < 0.1 second.

3.3.2 End-systolic Displacement, E_{cc} Maps and E_{cc} -time Curves from Healthy Volunteers and Patients with Heart Disease

Examples of end-systolic displacement, E_{cc} maps and segmental E_{cc} -time curves from StrainNet and TransStrainNet processing of bSSFP image contours and from DENSE for a healthy control (Figure 3-4) and a patient with heart failure with left bundle branch block (Figure 3-5) are shown. For the healthy control, both StrainNet and TransStrainNet depicted normal displacement and E_{cc} , showing good agreement with DENSE. For the patient with LBBB, StrainNet displayed less septal stretch and less lateral wall shortening than DENSE, whereas TransStrainNet showed much better agreement with DENSE in all segments.

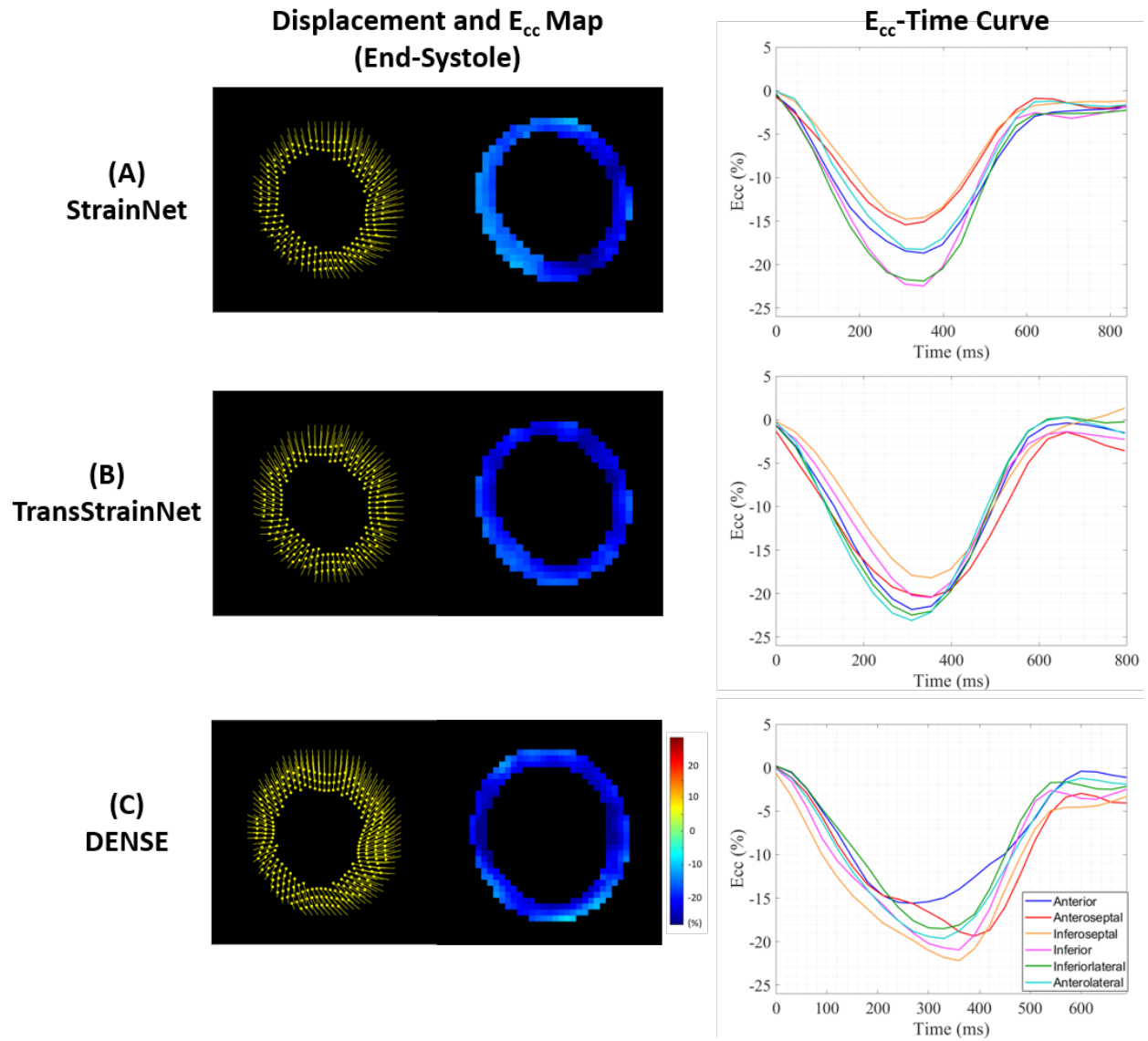


Figure 3-4: Example of end-systolic displacements and E_{cc} maps and segmental circumferential strain-time curves comparing (A) StrainNet and (B) TransStrainNet analysis of bSSFP cine images and (C) ground-truth DENSE for a healthy volunteer.

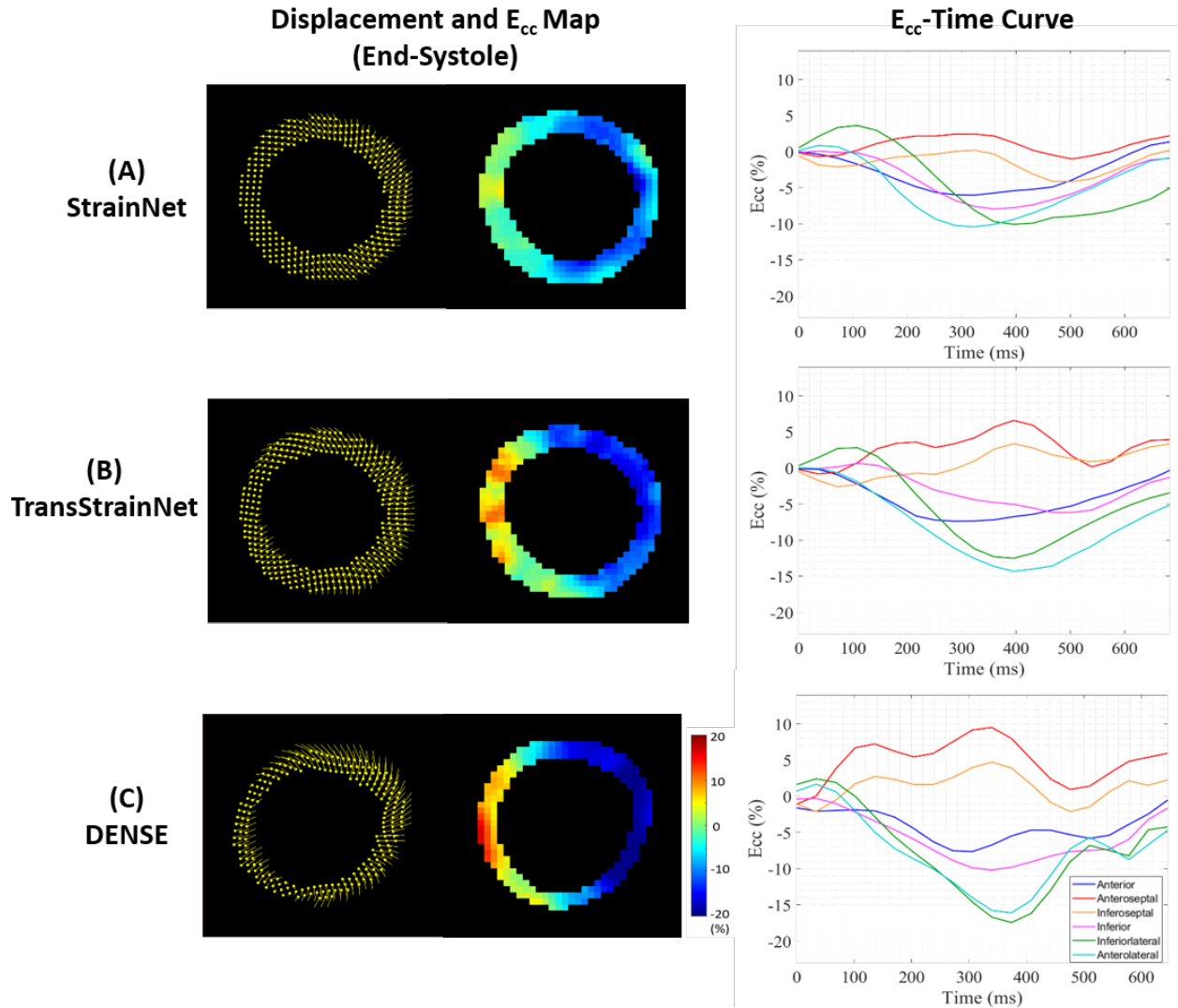


Figure 3-5: Example of end-systolic displacements and E_{cc} maps and segmental circumferential strain-time curves comparing (A) StrainNet and (B) TransStrainNet analysis of bSSFP cine images and (C) ground-truth DENSE for a heart failure patient with left bundle branch block.

3.3.3 Correlations and Agreement of End-systolic E_{cc} and Whole E_{cc} -time Curves

Table 3.1 summarizes the ICCs validated on general testing dataset and on the LBBB subgroup comparing FT, StrainNet and TransStrainNet with DENSE for the assessment of global and segmental E_{cc} . For the general testing dataset, the ICCs between FT and DENSE, StrainNet and DENSE, TransStrainNet and DENSE and were 0.72, 0.87 and 0.87, respectively, for global E_{cc} and 0.48, 0.75 and 0.75, respectively, for segmental E_{cc} , showing that both StrainNet and TransStrainNet had good agreement with DENSE and outperformed FT for both global and segmental E_{cc} . For the LBBB subgroup, TransStrainNet demonstrated the best agreement with DENSE with an ICC of 0.64 for segmental E_{cc} , better than StrainNet and FT with ICCs of 0.57 and 0.49, respectively. RMSE of segmental whole-strain time curves between StrainNet and DENSE and TransStrainNet and DENSE were 3.11 vs. 3.02 for general testing dataset and were 3.96 vs. 3.62 for LBBB subgroup, showing that TransStrainNet had improved performance on segmental strain analysis across the cardiac cycle.

Table 3-1: Comparison of agreement between StrainNet, TransStrainNet and Feature Tracking with DENSE for global and segmental peak-systolic E_{cc} and whole E_{cc} -time curve errors

Group	Metrics	StrainNet	TransStrainNet	FT
All Testing Data	ICC (Global Peak E_{cc})	0.87	0.87	0.72
	ICC (Segmental Peak E_{cc})	0.75	0.75	0.48
	RMSE (Whole E_{cc} -Time Curve)	3.11	3.02	/
LBBB Subgroup	ICC (Global Peak E_{cc})	0.35	0.41	0.31
	ICC (Segmental Peak E_{cc})	0.57	0.64	0.49
	RMSE (Whole E_{cc} -Time Curve)	3.96	3.62	/

Note. E_{cc} = circumferential strain, ICC = Intra-class correlation coefficient, LBBB = left bundle branch block, RMSE = root mean squared error.

3.4 Discussion

While DL-based motion estimation and strain analysis of routine bSSFP cine images have achieved improvements than conventional FT, it is still challenging to accurately track complex cardiac motion such as the patients with mechanical dyssynchrony. In our study, we developed a transformer-based DL framework, named TransStrainNet, that combines the self-attention mechanisms for long-term dependencies and the locality properties of convolution, to capture both global and local patterns for improved intramyocardial motion estimation from contour motion. TransStrainNet showed similarly good performance with StrainNet on general dataset on patients with heart diseases and healthy controls, and demonstrated improved performance on LBBB patients with complex cardiac motion patterns with distinctive long-term spatiotemporal dependencies. The improved strain analysis accuracy also provided the opportunity for providing strain-based prognostics from cine bSSFP images, which was previously limited due to its suboptimal calculation. There are several major findings of our study TransStrainNet generally demonstrated similarly good performance to StrainNet for predicting intramyocardial displacement and strain. Further, for LBBB patients with dyssynchrony and distinctive long-term spatiotemporal relationships of heart motion, the TransStrainNet, which is well-suited for long-term dependencies, led to better performance for the prediction of segmental strain. In addition, TransStrainNet showed better performance on the whole-strain time curves as well as the end-systole peak strain values

Learning-based myocardial motion tracking methods have been investigated previously (51-54) and demonstrated the potential for the performance and inference efficiency than

conventional FT algorithms which were mainly based on optical-flow (9) or deformable (73) models. Although convolutional neural networks are well-suited for vision tasks by extracting high-level and multi-scale features, convolution has a relatively small receptive field which may limit its accuracy for modeling time-series data, especially to learn long-range dependencies such as those that may be present in cine CMR of the heart (76). Our design combined Swin Transformer with convolution in a 2D+t U-Net structure which could simultaneously capture the multi-scale global and local spatiotemporal features, and therefore have improved performance for modeling the complex dynamics of physiological and pathophysiological heart motion. In addition to the architecture design, TransStrainNet also benefited from the availability of multi-center, multi-disease datasets to develop a comprehensive mapping from contour motion to accurate displacement maps for various cardiac motion patterns. To further validate TransStrainNet in clinical applications on CRT patient outcome prediction and showing its promises in risk stratification, our study will go beyond the displacement and strain accuracy assessment and validated strain metrics from bSSFP cine images in the next Chapter.

While the dataset in this study are diverse and substantial, a larger dataset would be better to train transformer models from scratch compared to convolutional neural networks due to the increased complexity and larger number of model parameters. In addition, an external testing dataset may be needed in the future to validate the model generalization ability and the potential data leakage between the training and testing groups. Moreover, reproducibility experiments of the segmentation of endocardial and epicardial contours from different segmentation algorithms and different users should be conducted. In this study, we have developed the DL pipeline with the aim of improved motion estimation from contour motion and the consequence strain analysis.

However, the actual impact on clinical workflows remains to be validated, and we will test our models in inline settings on the scanners in the future.

In conclusion, a transformer-based DL framework combining self-attention and convolution was developed to accurately predict intramyocardial motion from contour motion by capturing both global and local feature patterns. TransStrainNet showed better performance than StrainNet for the peak-systole global and segmental circumferential strain and better accuracy on through-time strain estimation on LBBB subgroup with complex spatiotemporal motion patterns, using DENSE as the reference.

Chapter 4 – Application in CRT Patient Prognostication

4.1 Background

4.1.1 Strain in CRT

Heart failure is a growing burden for the United States, with around one million new cases emerging annually (82). Forecasts indicate that by 2030, over 8 million Americans will be living with heart failure, translating to a prevalence of 1 in every 33 individuals (83). Cardiac resynchronization therapy (CRT), using a pacemaker or implantable cardioverter defibrillator to restore the normal patterns of the heartbeat, has proven effective in improving mechanical synchrony and thus enhancing outcomes in selected heart failure patients - demonstrating a reduction in symptoms, hospitalizations, and an increase in survival rates (84-91). However, the clinical challenge lies in discerning the appropriate recipients for CRT, as its significant benefits are observed in only 55-65% of patients deemed responders in observational studies (92, 93).

Cardiovascular Magnetic Resonance (CMR) has been highlighted for its critical role in optimizing CRT application, as detailed in a white paper by the SCMR Clinical Trials Committee (94). CMR techniques are pivotal in identifying patients poised to benefit from CRT by quantifying the degree of cardiac dyssynchrony (95) and in pinpointing the most effective pacing sites by mapping mechanical activation time (96). The circumferential uniformity ratio estimate (97) with singular value decomposition (CURE-SVD) derived from DENSE (93) stands as a robust biomarker to quantify dyssynchrony, and CURE-SVD by DENSE has been proved to be a stable predictor of CRT response, survival, and arrhythmia outcomes (93, 95, 98). The CURE-SVD, a validated metric for assessing cardiac discoordination based on regional circumferential strain, has been strongly associated with CRT patient outcomes, with a lower CURE-SVD from DENSE indicating a favorable response. Although alternative CURE-SVD calculations based on FT from

bSSFP cine images might align with an efficient clinical workflow, the limited reproducibility for segmental strain of FT hampers its effectiveness in prognostics and CURE-SVD computations.

Development of a technique to accurately evaluate dyssynchrony using CURE-SVD from standard bSSFP cine images would significantly enhance CMR's utility in CRT management, expanding its availability to more patients and centers via a more rapid CMR examination. CRT's capacity to improve cardiac function through biventricular pacing, particularly in late-activating myocardium, underscores its potential can improve survival rate, enhance heart function, and improve quality of life (65). Nevertheless, with a nonresponse rate of about 40%, refining the prediction of CRT responsiveness is crucial for managing potential CRT candidates (66). Utilizing CMR results to select suitable patients for CRT and to direct the implantation of the left ventricular (LV) pacing lead to the optimal region can substantially impact treatment outcomes (67).

4.1.2 StrainNet Analysis of CRT Patients

TransStrainNet has shown outperformed performance than FT on the regional circumferential strain analysis in Aim 2. We developed and validated a general TransStrainNet model for improved motion estimation and strain analysis on healthy volunteers and patients with various types of heart disease. It leverages a broad dataset from multiple centers and multiple diseases for general intramyocardial motion tracking. As a foundational model, it could serve as an ideal pre-trained model for further fine-tuning on specialized tasks using additional, specific datasets. Since CRT is a very important application of strain for prognosis where we have bSSFP images, DENSE ground truth and outcomes, we will investigate whether DL strain analysis outperforms feature tracking for prognostication in CRT patients. The first, Study A, develops and validates a general TransStrainNet model for improved motion estimation and strain analysis on healthy volunteers and patients with various types of heart disease. It leverages a broad dataset from multiple centers

and multiple diseases for general intramyocardial motion tracking. As a foundational model, it could serve as an ideal pre-trained model for further fine-tuning on specialized tasks using additional, specific datasets. The second study, Study B, focuses on the clinical validation of strain metrics derived from TransStrainNet for prognostication of CRT patients, utilizing the baseline TransStrainNet model developed in Study A for the initial model weights and fine-tuning the model using the CRT cohort.

4.2 Methods

4.2.1 Patient Cohort Description

We included 120 patients with CRT and cardiac MRI examinations with DENSE between 2008 and 2023 (2, 98, 99). All patients had LV ejection fraction of 35% or less, NYHA functional class II-IV, and QRS greater than 120ms and qualified for CRT based on AHA/ACC/HRS guidelines. Before the CRT procedure at University of Virginia Health System, patients provided information on demographics, health conditions, and medications. There are 38 baseline characteristics available for this cohort, including 6 demographic characteristics (gender, age, Body Mass Index (BMI), weight, New York Heart Association (NYHA) heart failure class, and race), 6 comorbid conditions (ischemic cardiomyopathy, hypertension, atrial fibrillation, chronic kidney disease, diabetes mellitus, and prior Coronary Artery Bypass Graft (CABG)), 5 medications (beta-blocker use, Angiotensin-Converting Enzyme (ACE) inhibitor use, loop diuretic dose, digoxin, and statin), 7 laboratory studies, vital signs, and exercise testing (systolic blood pressure, sodium, creatinine, hemoglobin, Glomerular Filtration Rate (GFR), B-Type Natriuretic Peptide (BNP), and Peak VO₂), 8 Cardiac Magnetic Resonance (CMR) and echocardiography assessment parameters (Left Ventricular Ejection Fraction (LVEF), Left Ventricular End-Diastolic Volume Index (LVEDVI),

Left Ventricular End-Systolic Volume Index (LVESVI), Right Ventricular Ejection Fraction (RVEF), Right Ventricular End-Diastolic Volume Index (RVEDVI), Right Ventricular End-Systolic Volume Index (RVESVI), presence of Late Gadolinium Enhancement (LGE), and Circumferential Uniformity Ratio Estimate with Singular Value Decomposition (CURE-SVD)), and 6 Electrocardiogram (ECG) parameters (QRS, QRS-LV Electrogram Time (QLV), Left Bundle Branch Block (LBBB), Right Bundle Branch Block (RBBB), Paced rhythm, and upgrade or new device).

There are three response parameters available at 6 months post CRT, including Left Ventricular End-Systolic Volume Index Fractional Change (LVESVI-FC), B-type natriuretic peptide (BNP), and Δ Peak VO₂. 6-month LVESVI-FC was determined by a second echocardiography scan 6 months after their CRT procedure. Determination of death was based on clinical follow-up, reports of deaths from families, and a regional death index. Demographics and clinical data are summarized in Table 4.1.

Table 4-1: Demographics of the 200 CRT patients. Values are median (interquartile range) or n (%). ACE = angiotensin-converting enzyme; ARB = angiotensin receptor blocker; BMI = body mass index; BNP = B-type natriuretic peptide; BP = blood pressure; CABG = coronary artery bypass graft; CURE-SVD = circumferential uniformity ratio estimate with singular value decomposition; GFR = glomerular filtration rate; LBBB = left bundle branch block; LGE = late gadolinium enhancement; LVEDVI = left ventricular end-diastolic volume index; LVEF = left ventricular ejection fraction; LVESVI = left ventricular end-systolic volume index; NYHA = New York Heart Association; QLV = QRS-LV electrogram time; RBBB = right bundle branch block;

RVEDVI = right ventricular end-diastolic volume index; RVEF = right ventricular ejection fraction; RVESVI = right ventricular end-systolic volume index.

Patient Characteristics	Cohort (N = 200)	Patient Characteristics	Cohort (N = 200)
Demographics		CMR & Echocardiography	
Age, years	67.4 (58.0-74.0)	LVEF, %	24.0 (17.7-30.5)
BMI	28.9 (25.4-33.7)	LVEDVI, mL/m ²	126.3 (102.5-157.0)
Weight (kg)	89.4 (75.1-102.9)	LVESVI, mL/m ²	93.7 (73.7-123.6)
Female	54 (27.0%)	RVEF, %	37.5 (25.8-45.6)
NYHA HF Class		RVEDVI, mL/m ²	68.5 (52.9-83.1)
II	73 (36.5%)	RVESVI, mL/m ²	38.8 (29.9-55.5)
III	126 (63.0%)	LGE Presence	95 (47.5%)
IV	1 (0.5%)	CURE-SVD	0.59 (0.45-0.76)
Race		ECG Parameters	
Black	27 (13.5%)	QRS, ms	158 (142-175)
White/Other	173 (86.5%)	QLV, ms	120.0 (87.0-149.3)
Comorbid Conditions		LBBB	151 (75.5%)
Isch. Cardiomyopathy	87 (43.5%)	RBBB	22 (11.0%)
Hypertension	115 (57.5%)	Paced Rhythm	28 (14.0%)
Atrial Fibrillation	52 (26.0%)	Upgrade or New Device	
Chronic Kidney Dis.	62 (31.0%)	De Novo Device	153 (76.5%)
Diabetes Mellitus	73 (36.5%)	Upgrade Device	47 (23.5%)
Prior CABG	35 (17.5%)	Response (6 Months)	
Medications		Fractional Change LVESVI	-0.18 (-0.33--0.01)
Beta-Blocker	191 (95.5%)	BNP, pg/mL	177.0 (59.5-592.0)
ACE Inhibitor or ARB	175 (87.5%)	Δ Peak VO ₂ , mL/kg/min	-0.01 (-1.2-1.3)
Loop Diuretic Dose, mg		Survival Status at 4 Years	
0	58 (29.0%)	Alive	149 (74.5%)
20-40	90 (45.0%)	Dead	51 (25.5%)
60-80	34 (17.0%)		
>100	18 (9.0%)		
Digoxin	17 (8.5%)		
Statin	120 (60.0%)		
Laboratory, Vital Signs			
Systolic BP, mm Hg	118.0 (104.0-130.0)		
Sodium, mEq/L	138.0 (137.0-140.0)		
Creatinine, mg/dL	1.1 (0.9-1.3)		
Hemoglobin, g/dL	13.25 (12.3-14.7)		
GFR, mL/min/1.72m ²	67.2 (54.1-84.1)		
BNP, pg/mL	272.0 (130.0-632.3)		
Peak VO ₂ , mL/kg/min	14.4 (12.5-15.8)		

4.2.2 Determination of CURE-SVD

CURE-SVD will be calculated from the circumferential strain in 18 segments per slice. Specifically, the circumferential strain data will be used to create a 2D strain matrix E_{cc} and a rank-1 approximation of the matrix E_{cc}^1 will be calculated using Singular Value Decomposition (SVD) as shown in the following equation:

$$E_{cc}^1 = US^1V^*,$$

where the columns of U and V consist of the left and right singular vectors, respectively. S is a diagonal matrix whose diagonal entries are the singular values of E_{cc} , and S^1 contains only the first singular value (69). Fourier Transform will be applied on one column of E_{cc}^1 , and CURE-SVD will be calculated based on $f_0/(f_0 + f_1)$, where f_0 is the zero-order term of the Fourier transform, and f_1 is the first-order term, representing low frequency changes. CURE-SVD score ranges from 0 to 1, with 1 indicating perfect synchrony.

For bSSFP images, the endocardial and epicardial contours will be automatically detected and regional circumferential strain will be calculated from a commercial software (suiteHEART, NeoSoft). StrainNet will be applied to the same bSSFP images and get the displacement and circumferential strain values. The alternative CURE-SVD scores will be derived from FT and StrainNet, respectively. The imaging analysis will be conducted blinded to DENSE analysis and survival outcomes.

For cine MRI, the CURE-SVDs were calculated for mid-ventricular slices and averaged to get a single CURE-SVD value for each subject. The CURE-SVD scores were derived from TransStrainNet and FT, respectively, termed CURE-SVD-TransStrainNet and CURE-SVD-FT. The CURE-SVD values from DENSE were calculated as previously reported (2, 98).

4.3.3 Prediction of CRT Response and Outcomes

CRT response was measured as the fractional change over 6 months in LV end-systolic volume index (FC-LVESVI = [post-LVESVI - baseline LVESVI] / baseline LVESVI, with negative as favorable response), and with the decrease larger than 15% considered as a favorable responder. Logistic regressions were used to predict the 6-month response and 4-year survival free of heart transplantation and LV assist device based on CURE-SVDs.

4.3.4 Statistics Analysis

Short-axis (base, mid, apex) endocardial and epicardial contours will be automatically detected from bSSFP images from all subjects and FT will be performed by experienced individuals using commercial software (SuiteHeart, NeoSoft). The endocardial and epicardial contours will be exported to a personal computer and used as input into TransStrainNet for displacement and global and segmental circumferential strain analysis.

The Receiver operating characteristic (ROC) curves for each fold within the 5-fold cross-validation for CURE-SVD-TransStrainNet and CURE-SVD-FT were generated, and areas under the ROC curves (AUC) were calculated to evaluate and compare the performances of response and survival predictions, respectively. Kaplan-Meier analysis and Cox proportional hazards regression was used to construct the 4-year survival curves based on the medium cluster identified by CURE-SVDs for TransStrainNet, NeoSoft and DENSE, respectively. $P < .05$ was considered statistically significant. Statistical analyses were performed using MATLAB R2018b (Mathworks Inc, Natick, MA) and Python 3.9.7 (Python Software Foundation).

4.4 Results

4.4.1 CRT Patients Response and Outcome Predictions

Binary classification was performed based on CURE-SVD-FT, CURE-SVD-TransStrainNet and CURE-SVD-DENSE, and the prediction performance was shown for 6-month response (Figure 4-1) and 4-year survival (Figure 4-2) with ROC curves. The AUCs for each fold within the cross-validation was displayed along with the area under the average ROC curve. The average AUC values for FT, TransStrainNet and DENSE were 0.67 ± 0.12 , 0.72 ± 0.07 and 0.80 ± 0.09 for 6-month response prediction, and 0.65 ± 0.08 , 0.69 ± 0.07 and 0.72 ± 0.13 for 4-year survival outcome prediction. TransStrainNet demonstrated better prognostication performance and less variability than FT for both 6-month remodeling and survival prediction.

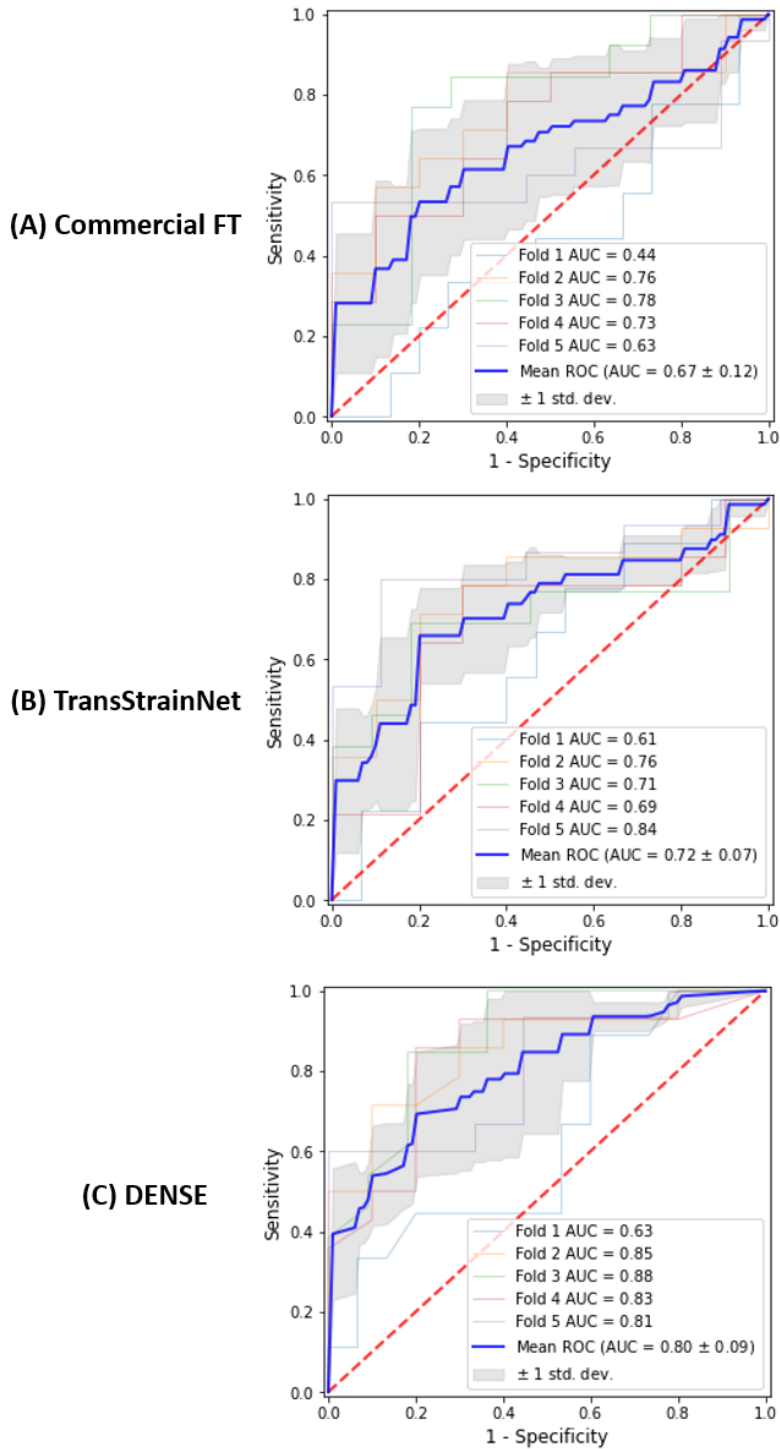


Figure 4-1: Time-Dependent Receiver-Operating Characteristic Curves for CRT patient 6-month response prediction with 5-fold cross validation. Time-dependent receiver-operating characteristic curves based on CURE-SVDs are shown for 3 models: (A) Commercial Feature Tracking, (B) TransStrainNet and (C) DENSE.

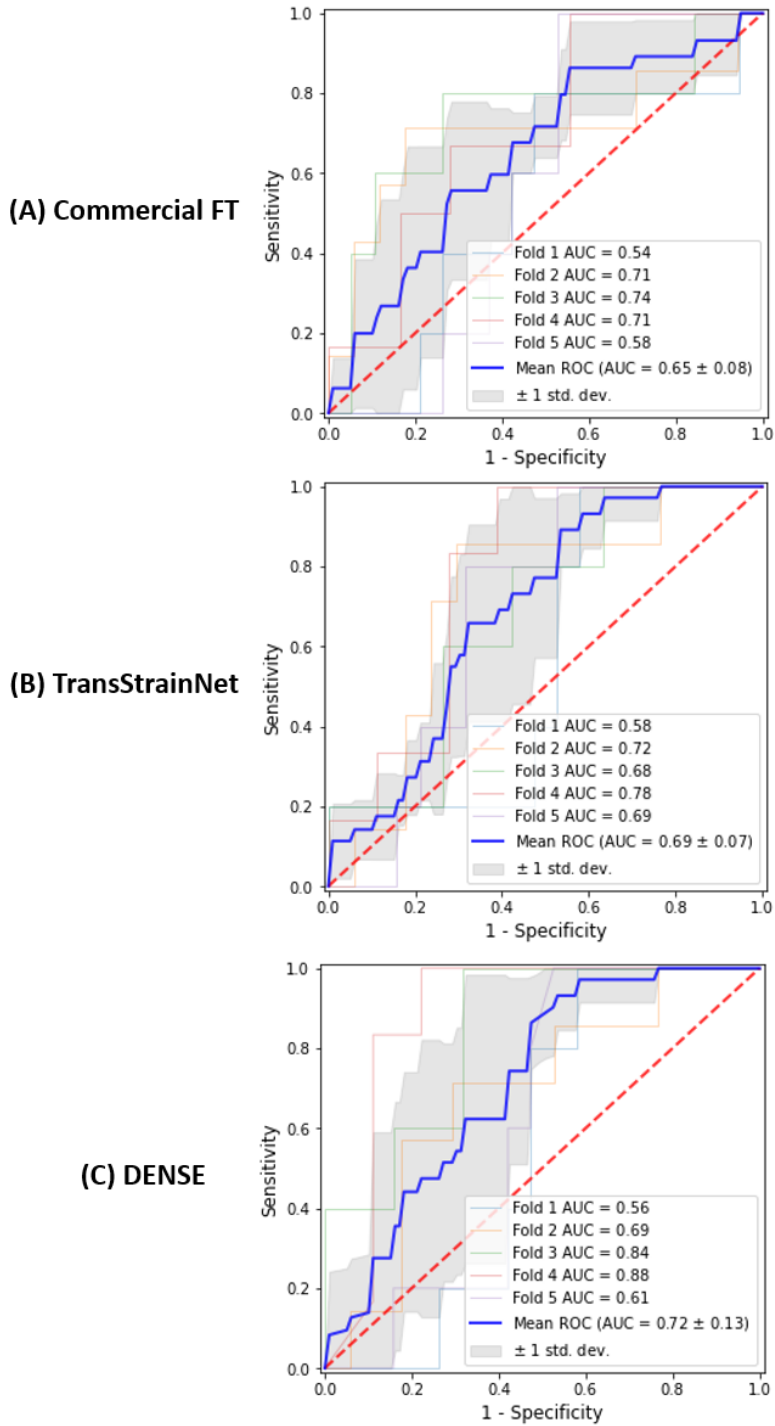


Figure 4-2: Time-Dependent Receiver-Operating Characteristic Curves for CRT patient 4-year survival prediction with 5-fold cross validation. Time-dependent receiver-operating characteristic curves based on CURE-SVDs are shown for 3 models: (A) Commercial Feature Tracking, (B) TransStrainNet and (C) DENSE.

4.4.2 CRT Cohort Risk Stratification

The Kaplan-Meier survival analysis was displayed in Figure 4-3 and demonstrated that patients with lower CURE-SVD scores (Group 1) had better survival probability than patients with higher CURE-SVD scores (Group 2) in all three methods of FT, TransStrainNet and DENSE. FT showed obvious overlapping of the two survival curves after Year 2 compared to the overlapping area of TransStrainNet and DENSE. The hazard ratios (HR) for the two subgroups were 1.77 (95% CI: 0.95-3.31) for FT, 2.70 (95% CI: 1.40-5.21) for TransStrainNet and 2.88 (95% CI: 1.46-5.61) for DENSE. There were significant differences between the two survival groups stratified by CURE-SVD-TransStrainNet [P=.03] and by CURE-SVD-DENSE [P=.02]; whereas we found no evidence of differences between the survival groups stratified by CURE-SVD-FT [P=.07].

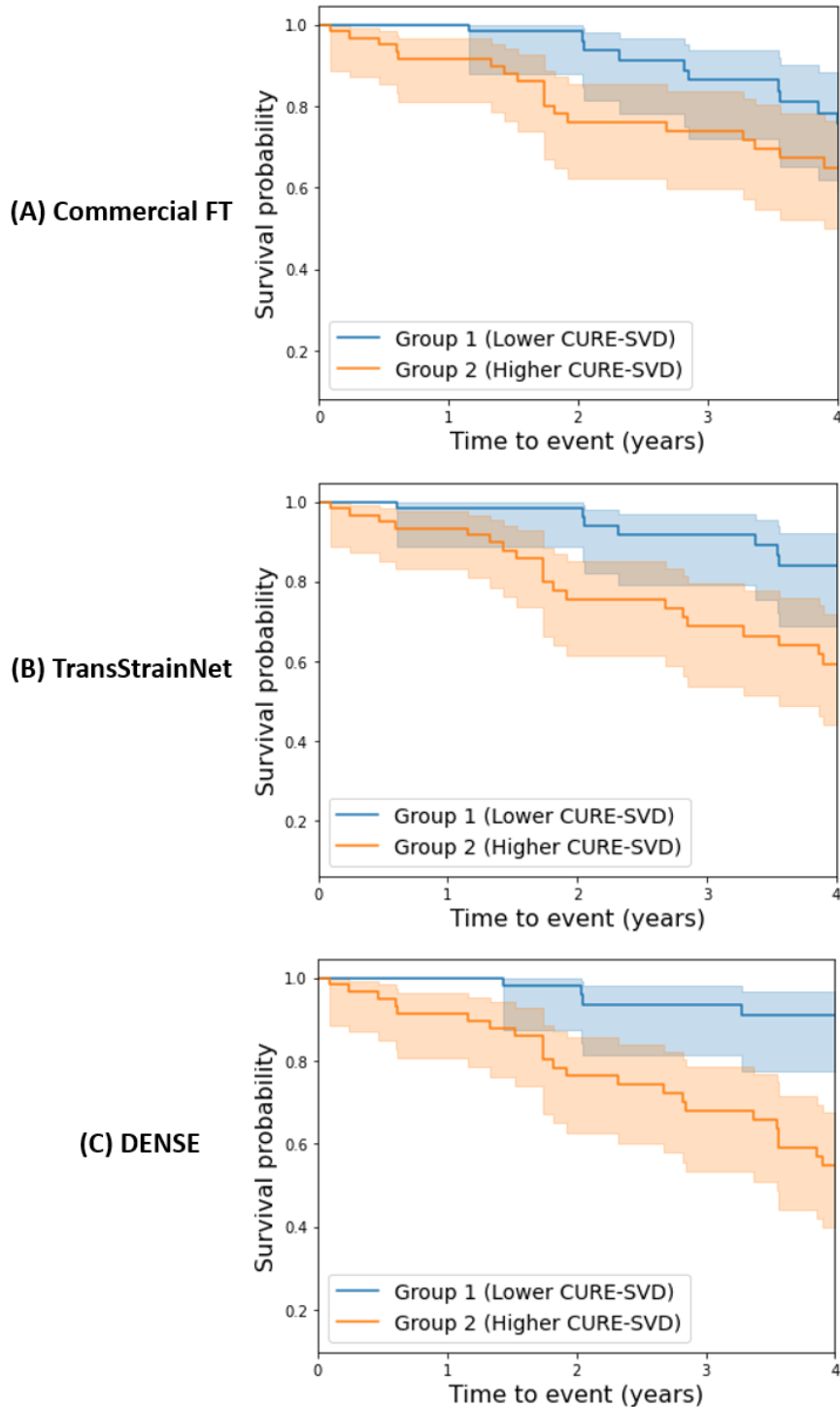


Figure 4-3: Stratified Kaplan-Meier analysis. Kaplan-Meier survival curves are presented for the two groups (Group 1: with lower CURE-SVD score, Group 2: with higher CURE-SVD score) stratified by the medium of CURE-SVDs from (A) Commercial Feature Tracking, (B) TransStrainNet and (C) DENSE.

Chapter 5 – Conclusions and Future Directions

5.1 Conclusions

Deep Learning characterization of cardiovascular diseases from cardiac MRI has clinical potentials in many aspects. This dissertation aims to address most of the technical challenges related to cine strain analysis by utilizing strain-dedicated DENSE data to demonstrate the potential at the quantification level and clinical prognostication level.

We developed StrainNet model to predict intramyocardial displacement from contour motion trained with DENSE data and tested with cine MRI. We showed that StrainNet outperformed commercial feature tracking for global and segmental circumferential strain analysis of cine MRI. We also investigated the use of self-attention mechanisms and transformer blocks (TransStrainNet) for improved motion estimation ability by capturing the complex heart motion patterns and long-term dependencies. TransStrainNet demonstrated better performance than StrainNet for the peak-systole global and segmental circumferential strain and better accuracy on through-time strain estimation on LBBB subgroup. In addition to the strain value assessment, we experimented on the clinical applications of TransStrainNet by predicting the prognostication of CRT patients based on CURE-SVDs to quantify cardiac dyssynchrony, and showed better performance than the results from commercial FT on 6-month response and 4-year outcome prediction.

5.2 Future Directions

5.2.1 Reproducibility of StrainNet

In this dissertation, we have developed and validated StrainNet on multi-site, multi-disease dataset containing healthy volunteers and patients. However, we have not done extensive experiments on the reproducibility of StrainNet. In the future, reproducibility experiments, especially in the

context of segmentation of endocardial and epicardial contours from different segmentation algorithms and different users, should be conducted to validate the robustness and reproducibility. In addition, an external testing dataset may be needed to validate the model generalization ability and the potential data leakage between the training and testing groups.

5.2.2 StrainNet Extension to Multi-modality

StrainNet is trained using DENSE images to predict intramyocardial displacement from myocardial contours and can be applied to any image series that provides myocardial contours. In this dissertation, we have developed and validated StrainNet application in cine MRI images. Since the input of StrainNet only utilizes the contour motion, StrainNet can be applied to any image series that provides myocardial contours such as echocardiographic images and CT images.

Echocardiography is the most commonly used modality in myocardial strain imaging and is more practical in clinical applications (31, 33, 100). Myocardial deformation analysis based on echocardiography is an easily accessible and low-cost procedure with no patient discomfort (101). StrainNet provides the opportunity to combine the accuracy of strain-dedicated images by training from DENSE and the convenience of echocardiographic images in real clinical settings.

Although CT images are not very commonly used in myocardial strain imaging, there are still some promising research recently to show the feasibility of CT in the calculation of regional cardiac function assessment. For example, Stretch QUantification of Endocardial Engraved Zones (SQUEEZ) has been developed for the quantitative evaluation of left ventricular function through automated 3D tracking of endocardial surface structures (36, 102, 103). Due to the generalization ability of StrainNet, it can also be applied to CT images for strain analysis.

StrainNet may provide more accurate strain analysis of echo images than speckle tracking echocardiography (STE). More importantly, by utilizing the same technique in different

modalities, StrainNet may provide more interchangeable strain values between echo and CMR, which used to be not interchangeable by utilizing STE to analyze echo imaging and FT or strain-dedicated images in MRI. Preliminary results were shown in Appendix B.

5.2.3 StrainNet Extension to Longitudinal Strain

Although short-axis images are commonly used in cardiac MRI, longitudinal strain is dominant in systolic strain especially in echocardiography (104-107). For example, imaging of global longitudinal strain is recommended for the early detection and monitoring of chemotherapy-induced cardiotoxicity (1, 108, 109). Extending StrainNet to long-axis images has great potentials and more clinical values. The development and validation of StrainNet analysis of cine MRI to assess global and segmental longitudinal strain will be valuable for a more comprehensive strain analysis pipeline. This could not only enhance the accuracy of cardiac function assessment but also broaden the scope of detectable cardiac abnormalities via myocardial strain imaging.

The long-axis version of StrainNet can also be applied to echocardiography will also be important for more accurate longitudinal strain analysis of echo images and for building up interchangeable longitudinal strain values between echo and MRI.

5.2.4 StrainNet Application to Cardiotoxicity

One of the most important clinical applications of myocardial strain imaging is the monitoring and early detection of chemotherapy-induced cardiotoxicity. Current treatment for cancer has led to cancer therapy-related cardiac dysfunction, heart failure and increased cardiovascular mortality in cancer survivors (110). The early detection of cardiac dysfunction is important and LV ejection fraction is commonly used to monitor the heart function. However, cardiac dysfunction may happen before the decreases of LVEF, a global metrics for function evaluation. Therefore, strain

imaging, especially segmental strain analysis, is critical in the detection of early and regional dysfunction. Although end-systolic global longitudinal strain assessed by echocardiography is routinely used for this application, CMR is also an important and likely superior modality as it can provide accurate LVEF and strain values. Previous studies have shown that CMR end-systolic global circumferential strain using FT is a new potentially powerful outcome predictor (111).

We have shown that StrainNet provides more accurate circumferential strain than commercial FT and therefore the application of StrainNet to the cardiotoxicity patient data will be of interest and may provide better prognostication performance. Figure 5-1 shows an example of impaired strain 3 months after initiating chemotherapy vs baseline detected using the StrainNet applied to bSSFP cine images from one breast cancer patient.

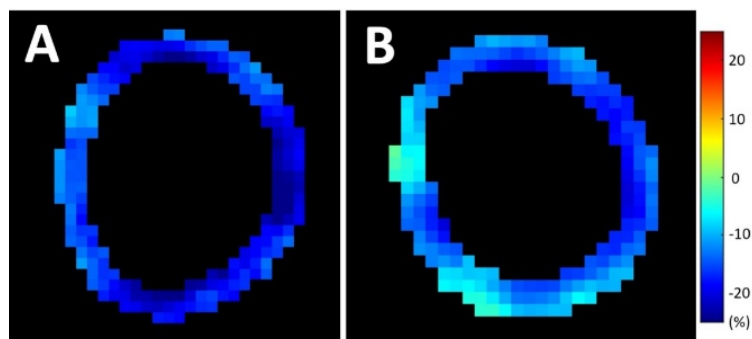


Figure 5-1: Example E_{cc} maps from a breast cancer patient before (A) and 3 months after (B) initiating chemotherapy. Impaired strain, especially in the septum and inferior wall are detected and quantified in (B).

5.2.5 Inline StrainNet

In this study, we have developed the DL pipeline with the aim of improved motion estimation from contour motion and the consequence strain analysis. However, the actual impact on clinical workflows remains to be validated, and we will test our models in inline settings on the scanners in the future. The integration with Siemens Framework for Image Reconstruction (FIRE) prototype

framework (112) may directly visualize the StrainNet analysis results on the console, providing real-time feedback in the clinical settings.

Appendix A – FlowNet2-based StrainNet

A.1 Background and Rationale

Before the current design of StrainNet architecture, a FlowNet2-based DL network was implemented to predict the intramyocardial displacement from myocardial contours. FlowNet 2.0 is one of the best 2D end-to-end optical flow convolutional neural networks (CNN) and is widely used for motion tracking in video imagery (113, 114). We implemented a DL-based FT model that uses FlowNet 2.0 but is retrained with DENSE data to estimate intramyocardial displacement from contour motion. This approach combines properties of optical flow with DENSE training data. In addition to these methods that primarily exploit spatial heart motion patterns, we will also exploit temporal patterns of heart motion by adding a subsequent through-time correction network and training it with dynamic through-time cine DENSE data.

The results were compared with StrainNet as shown in the A.2 Abstract below. Although we finally showed that a single 3D network as in StrainNet and TransStrainNet were better than FlowNet2-based networks two-step framework. The FlowNet2-based model showed the proof-of-concept to develop a DL-based FT framework using DENSE data to enable accurate and convenient myocardial strain imaging.

A.2 Abstract

Synopsis: Cine DENSE provides both myocardial contours and intramyocardial displacements. We propose to use DENSE to train deep networks to predict intramyocardial motion from contour motion. Two workflows were implemented: a two-step FlowNet2-based framework with a through-time correction network and a 3D (2D+t) Unet framework. Both networks depicted cardiac contraction and abnormal motion patterns. The 3D Unet showed excellent reliability for

global circumferential strain (E_{cc}) and good reliability for segmental E_{cc} , and it outperformed commercial FT for both global and segmental E_{cc} .

Summary of Main Findings: DENSE-trained deep networks can predict intramyocardial motion from contour motion, show good agreement with DENSE ground truth, and outperform a commercial feature tracking algorithm for global and segmental circumferential strain.

Background: CMR myocardial strain imaging is used diagnostically and prognostically for many types of heart disease. Feature tracking (FT) is a widely used and convenient method for strain MRI, as it applies post-processing algorithms directly to standard cine images to assess strain. It is, however, less accurate than strain-dedicated acquisitions like displacement encoding with stimulated echoes (DENSE) (1-4), especially for segmental strain. FT methods track myocardial contours rather than intramyocardial tissue because the myocardium presents uniform signal on cine MRI, lacking features to track. The intramyocardial motion is then (imperfectly) estimated using optical-flow based methods applied to the times series of endocardial and epicardial contours (5). In contrast, DENSE directly measures intramyocardial tissue displacement; however, it requires additional acquisitions. As DENSE provides both myocardial contours and accurate intramyocardial tissue displacement information, we investigated the use of DENSE data to train deep networks to predict intramyocardial tissue motion from contour motion. This deep learning (DL) approach may provide the clinical convenience of FT and accuracy similar to DENSE.

Methods: Two approaches were developed and evaluated: (a) a two-step FlowNet2-based framework with a through-time correction network (TC-FlowNet2), and (b) a 3D Unet. TC-FlowNet2 framework: This network was built upon a successful optical-flow convolutional neural network (CNN) called FlowNet2 (6), which is widely used for frame-to-frame motion tracking of video imagery. We fine-tuned FlowNet2 using DENSE datasets, and we added a 3D through-time

correction network to exploit the time dimension (Fig. 1A). 3D Unet framework: For this approach, a 3D Unet was trained to predict intramyocardial displacement from contour motion (Fig. 1B). For both approaches, during training, the inputs were a time series of myocardial contours derived from DENSE magnitude images and the ground truth data were DENSE tissue displacement measurements. Because DENSE and cine images at matched slice locations share similar motion patterns, we tested our trained model using contours derived from standard cine images (Fig. 1C).

Data pre-processing for network training: We segmented the left-ventricular myocardium on DENSE and cine images, binarized the images by filling the myocardial area with 1 and the outside area and blood pool with 0, and cropped the images to a fixed size: $N_x * N_y$. Data augmentation was performed using 90° rotations. Cine images were scaled to match the resolution range of DENSE images. The input size for the FlowNet2-based network was two frames of endocardial and epicardial contours and the output of the DT-FlowNet2 was the frame-to-frame displacement field. The input of the through-time correction network was a stack of sequential displacements fields from DT-FlowNet2 with size of $2 * N_x * N_y * N_t$, where the factor of 2 accounts for displacements in two directions and N_t represents the number of temporal frames. The output was also size of $2 * N_x * N_y * N_t$. For the 3D Unet, the input size was $N_x * N_y * N_t$ and the output size was $2 * N_x * N_y * N_t$.

Datasets: Training datasets are described in Fig. 1D, and included a total of 60 volunteers and 42 patients with various pathologies such as left bundle branch block (LBBB), hypertrophic cardiomyopathy, dilated cardiomyopathy, coronary artery disease and hypertension. The model was tested on cine images of 10 volunteers and 18 patients using 3 short-axis views (base, mid-level and apex). For TC-FlowNet2, datasets were divided into two parts to separately train DENSE-trained FlowNet2 and the correction network, thus the testing dataset number (15 subject,

48 slices) was half the size as that used for the 3D Unet. Commercial feature-tracking (suiteHEART, Neosoft, WI) was also used to measure strain from cine images.

Results: Fig. 2 shows examples comparing TC-FlowNet2, 3D Unet and DENSE for computing end-systolic displacement and circumferential strain (E_{cc}) for a healthy subject and a LBBB patient. In these examples, both methods detect cardiac contraction in the healthy volunteer and stretching of the septum in the LBBB patient, but TC-FlowNet2 shows less contraction. Fig. 3 shows examples comparing commercial FT, TC-FlowNet2, 3D Unet and DENSE for computing global and segmental circumferential strain-time curves, with the 3D Unet showing better agreement with the ground truth (DENSE). Correlation plots and Bland-Altman plots (Fig. 4A, B) show that 3D Unet outperformed both TC-FlowNet2 and commercial FT for global and segmental E_{cc} . Also, as shown in Table 1, the intraclass correlation coefficient (ICC), coefficient of variation (CoV), and Pearson correlation coefficient (Pearson CC) showed that the 3D Unet provides the best agreement with DENSE, where the 3D Unet achieved ICC = 0.89 for global E_{cc} and ICC = 0.75 for segmental E_{cc} . Although TC-FlowNet2 showed good linearity relationship with DENSE, it has a relatively big bias, leading to its high Pearson CC but relatively low ICC.

Conclusions: A 3D Unet, trained using DENSE datasets to predict intramyocardial motion from contour motion, outperformed both TC-FlowNet2 and commercial FT for the measurement of both global and segmental E_{cc} , for which DENSE data at matched locations served the reference standard.

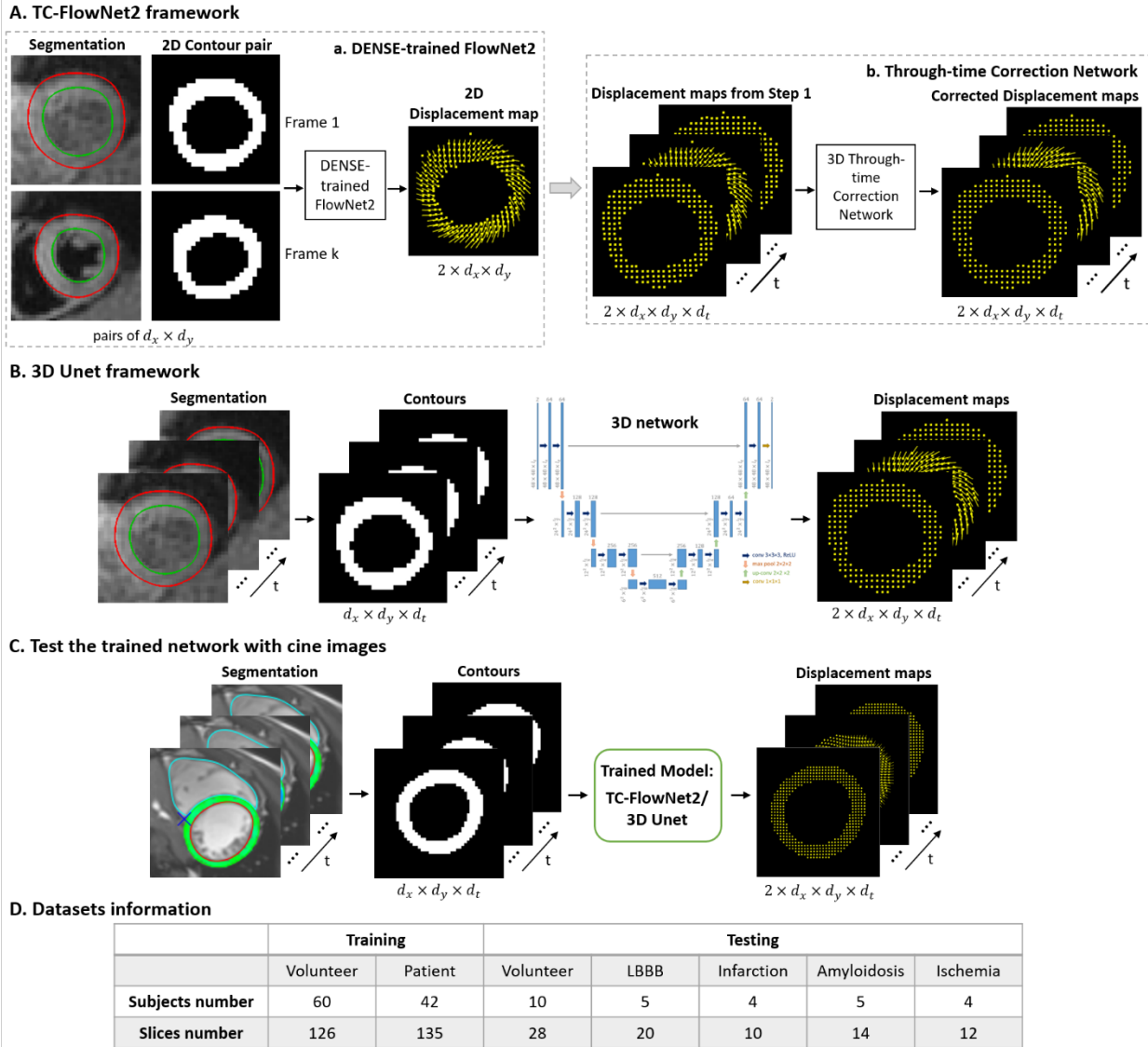
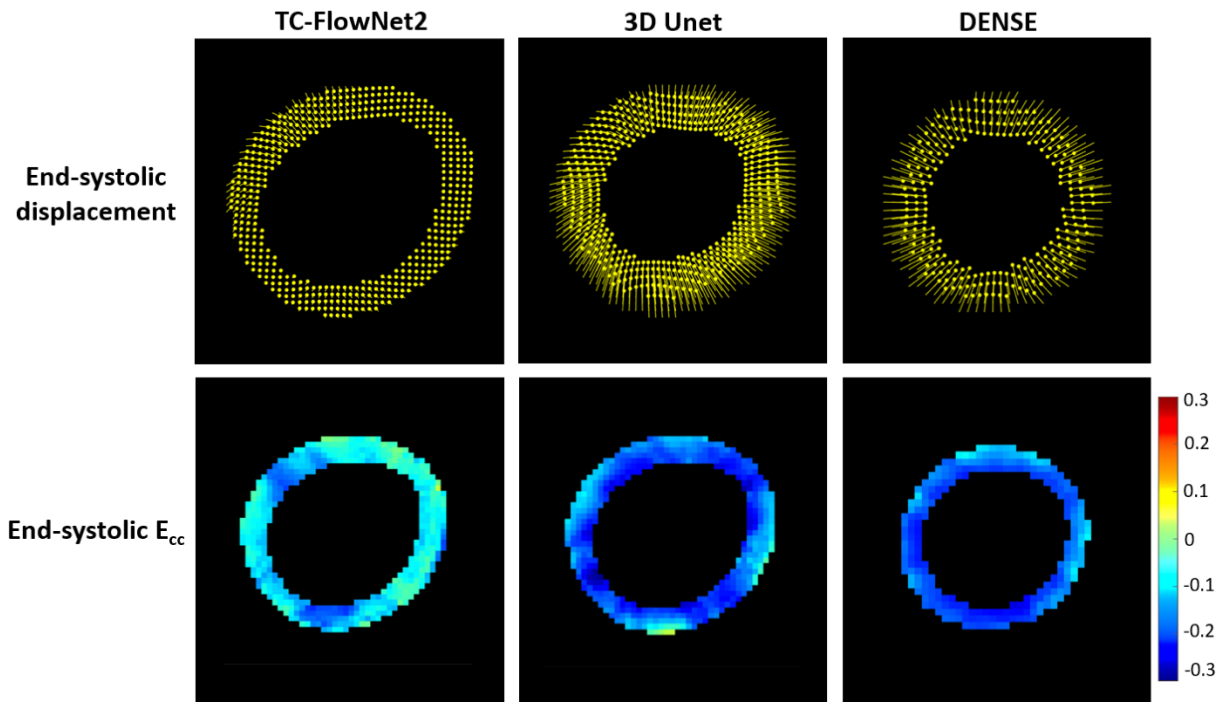


Figure Appendix A-1: Schematics showing (A) the through-time-corrected FlowNet2 framework, (B) the 3D Unet framework to predict intramyocardial displacement from contour motion, and (C) testing procedure to apply the trained network to cine images. (D) Also provided is a tabulation of the datasets used for training and testing.

A. Volunteer



B. LBBB patient

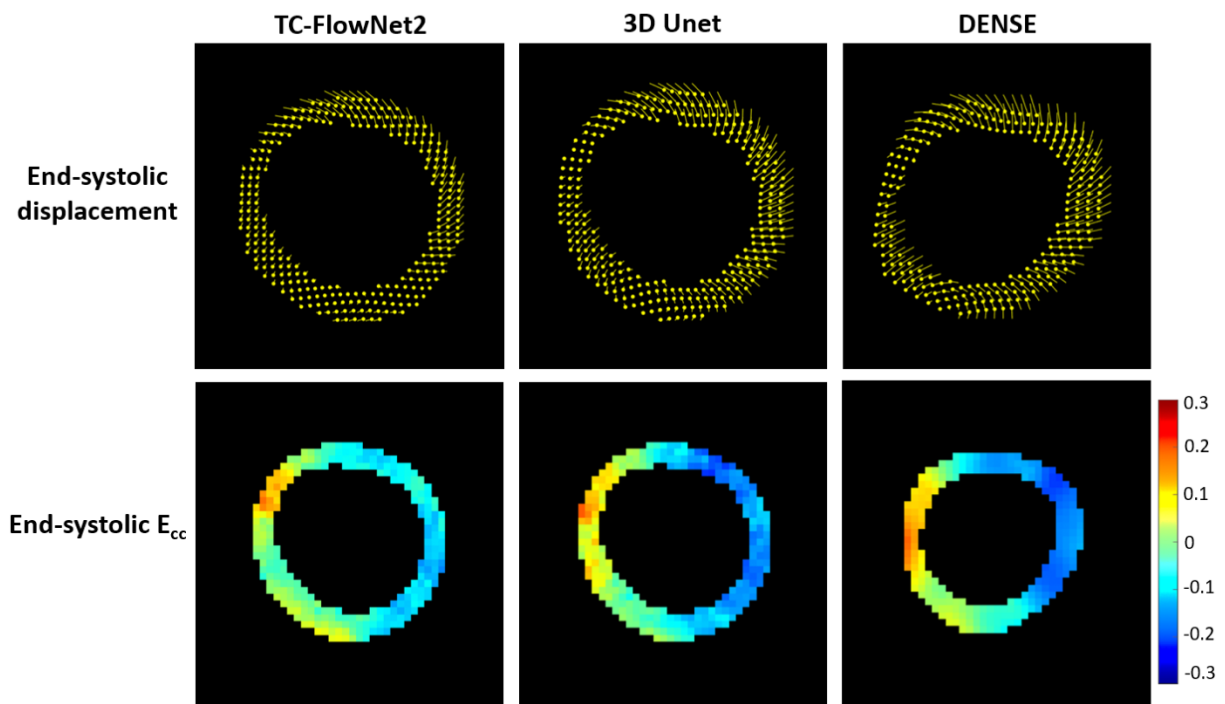


Figure Appendix A-2: Examples comparing TC-FlowNet2, 3D Unet and DENSE for mapping end-systolic displacement and end-systolic circumferential strain (E_{cc}) in a healthy subject (A) and a LBBB patient (B).

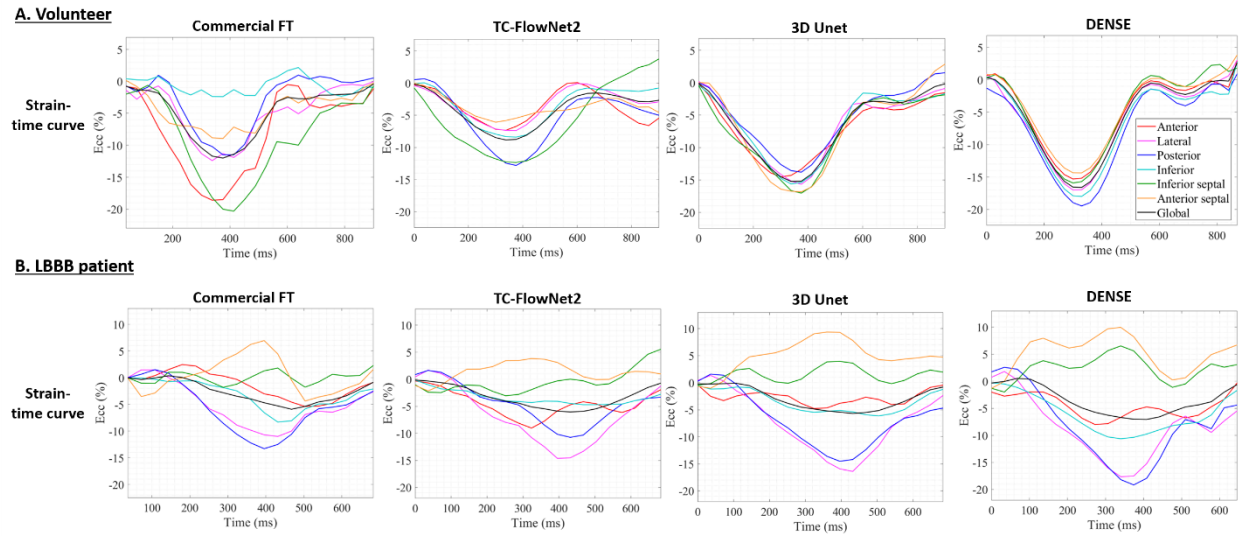
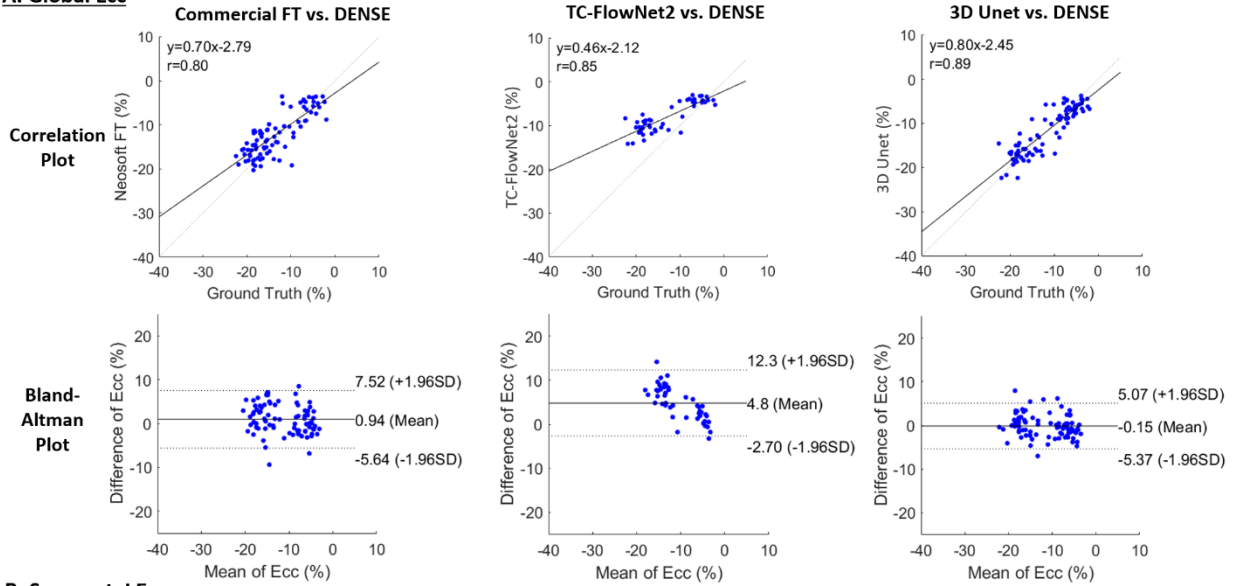


Figure Appendix A-3: Examples comparing TC-FlowNet2, 3D Unet, DENSE, and commercial FT (SuiteHEART, NeoSoft) for global and segmental circumferential strain-time curves in a healthy subject (A) and a LBBB patient (B).

A. Global Ecc



B. Segmental Ecc

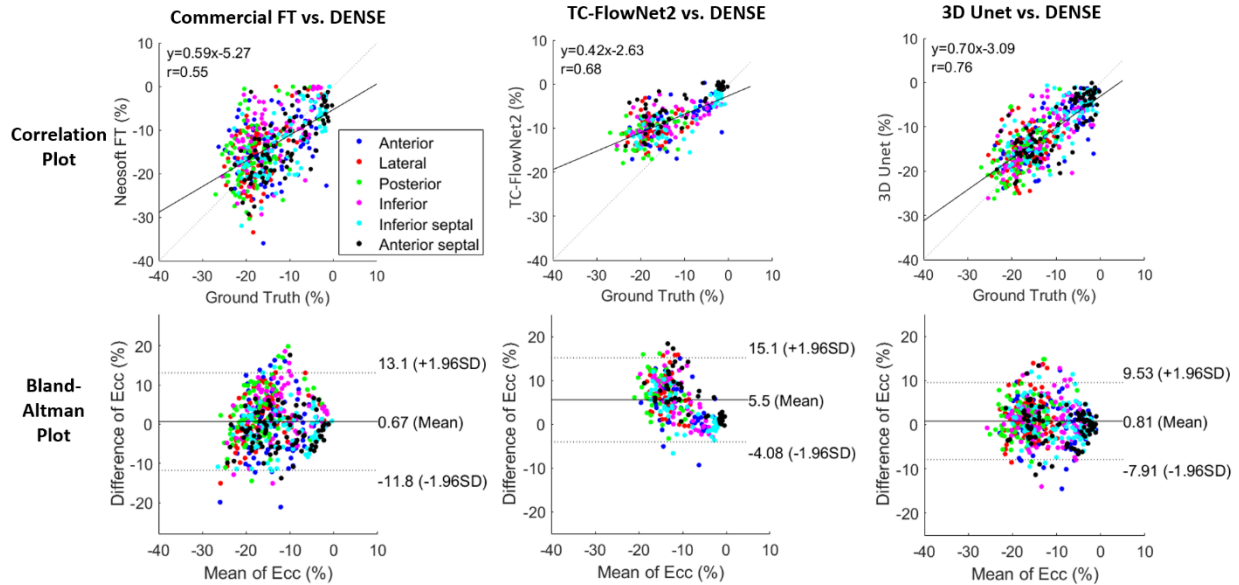


Figure Appendix A-4: Correlation plots and Bland-Altman plots comparing TC-FlowNet2, 3D Unet and commercial FT with DENSE ground truth data for global (A) and segmental (B) analysis of E_{cc} .

Table 1. Summary of ICC (Intraclass Correlation Coefficient), CoV (Coefficient of Variation) and Pearson CC for global and segmental Ecc

Method	Global Ecc			Segmental Ecc		
	Commercial FT	TC-FlowNet2 ³	3D Unet	Commercial FT	TC-FlowNet2 ³	3D Unet
ICC ¹	0.78	0.49	0.89	0.54	0.41	0.75
CoV ²	24.13	37.08	21.64	43.35	53.06	34.43
Pearson CC ¹	0.80	0.85	0.89	0.55	0.68	0.76

¹Reliability value ranges between 0 and 1, with values closer to 1 representing stronger reliability: < 0.5 indicate poor reliability, 0.5~0.75 indicate moderate reliability, 0.75~0.9 indicate good reliability, > 0.90 indicate excellent reliability.

²The higher the coefficient of variation, the greater the level of dispersion around the mean.

³TC-FlowNet2 results only have half of the datasets (48 slices) to test.

Table Appendix A-1: Summary of ICC (Intraclass Correlation Coefficient), CoV (Coefficient of Variation) and Pearson CC comparing TC-FlowNet2, 3D Unet and commercial FT with DENSE ground truth for global and segmental Ecc.

Appendix B – StrainNet Applied to Echocardiography

B.1 Abstract

Myocardial strain imaging is used diagnostically and prognostically for many types of heart disease. Strain-dedicated CMR techniques such as displacement encoding with stimulated echoes (DENSE) and myocardial tagging serve as the gold standard for strain assessment and for validating other strain measurement techniques [1-3]. StrainNet is a recently-developed deep learning model trained with DENSE data that predicts intramyocardial motion from myocardial contours (Fig. 1A), and has been validated on cine MRI [4]. Since StrainNet can be applied to any image series that provides myocardial contour motion, we investigated the application of StrainNet to echocardiography images (StrainNet-echo). Leveraging a deep network trained from gold standard strain-dedicated DENSE CMR, we hypothesized that StrainNet would provide more accurate strain analysis of echocardiography than speckle tracking echocardiography (STE) and provide more interchangeable strain values between the two modalities.

Datasets: Eighteen patients with heart failure and left bundle branch block (LBBB) underwent CMR with DENSE and echocardiography examinations, and the imaging studies were performed within 2 days of each other to minimize time-dependent variations in myocardial function. Forty slices from these patients at 3 short-axis views (base, mid-level and apex) were analyzed. Data processing: Segmentation and speckle tracking of echocardiography images were performed using TomTec-Arena 2D Cardiac Performance Analysis 1.3.0.147 on Agfa Healthcare Enterprise Imaging platform. For StrainNet analysis, echo images were scaled to match the mean spatial resolution of DENSE, and then were cropped to a fixed size. Images were binarized by filling the myocardial area with ones and the non-myocardial area with zeroes after LV segmentation using the TomTec STE LV contours (Fig. 1B).

Examples of end-systolic displacement and circumferential strain (E_{cc}) maps from StrainNet-echo and from CMR DENSE for a heart failure patient with LBBB are shown in Fig. 2A, and segmental strain-time curves corresponding to STE, StrainNet-echo and DENSE are shown in Fig. 2B. StrainNet-echo shows simultaneous stretching of the septal segments and contraction of the lateral wall, with good agreement with DENSE, whereas STE fails to show septal stretching, in disagreement with reference DENSE. While StrainNet-echo shows good agreement with STE for global E_{cc} , with an ICC of 0.90, with regard to agreement with DENSE, correlation plots, Bland-Altman plots (Fig. 3A, B), intraclass correlation coefficient (ICC), Pearson correlation coefficient (Pearson CC) and coefficient of variation (CV) (Fig. 3C) all show that StrainNet-echo outperformed STE for circumferential strain assessment, especially for segmental strain.

StrainNet predicts intramyocardial displacement and strain from echocardiography contours and showed good agreement with speckle tracking. StrainNet applied to echocardiography showed better agreement than STE with DENSE for both global and segmental E_{cc} .

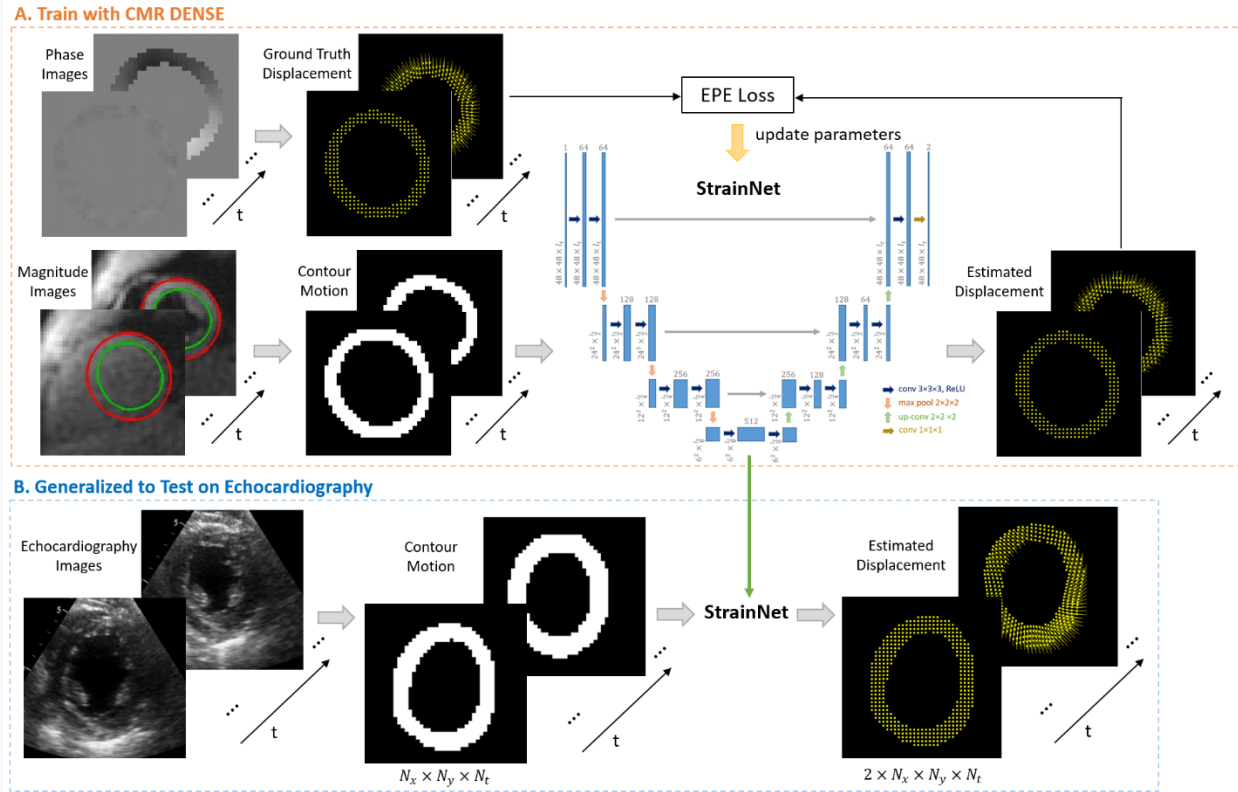


Figure Appendix A-1: (A) Schematic showing that, using CMR DENSE data, StrainNet was trained to predict intramyocardial displacement from contour motion. (B) Generalization of StrainNet to predict intramyocardial motion from echocardiography contour motion. The input size for the network was $N_x \times N_y \times N_t$, with N_t representing the number of temporal frames. The output size was $2 \times N_x \times N_y \times N_t$, with the factor of 2 accounting for displacements in two directions.

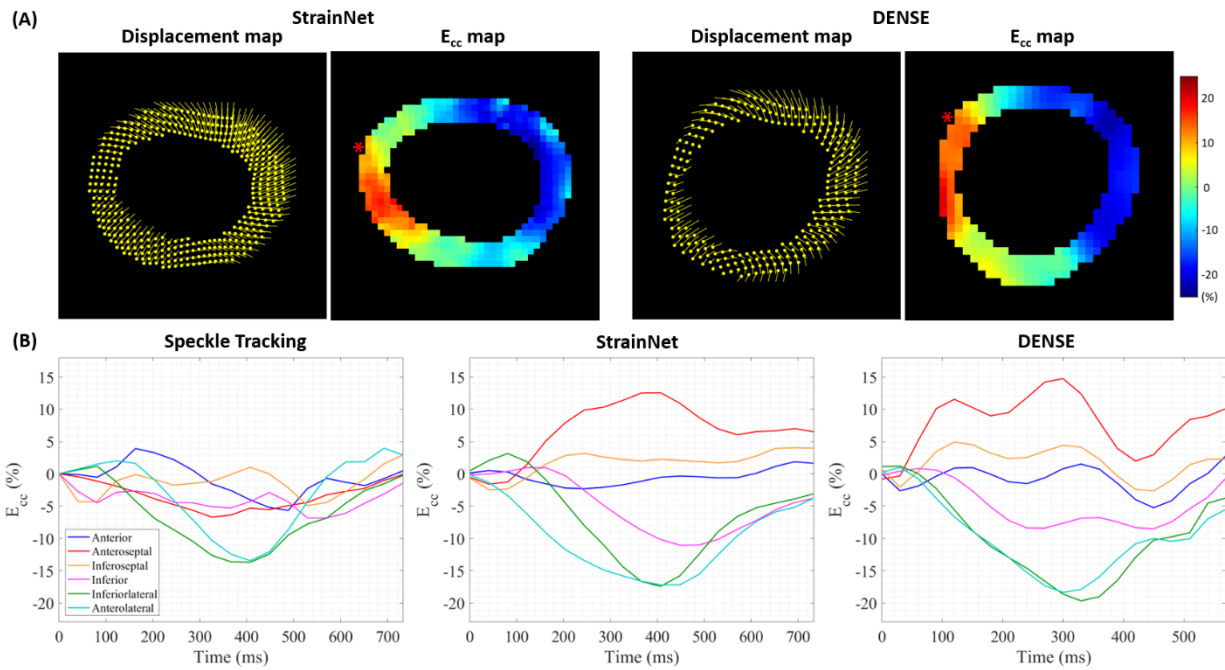
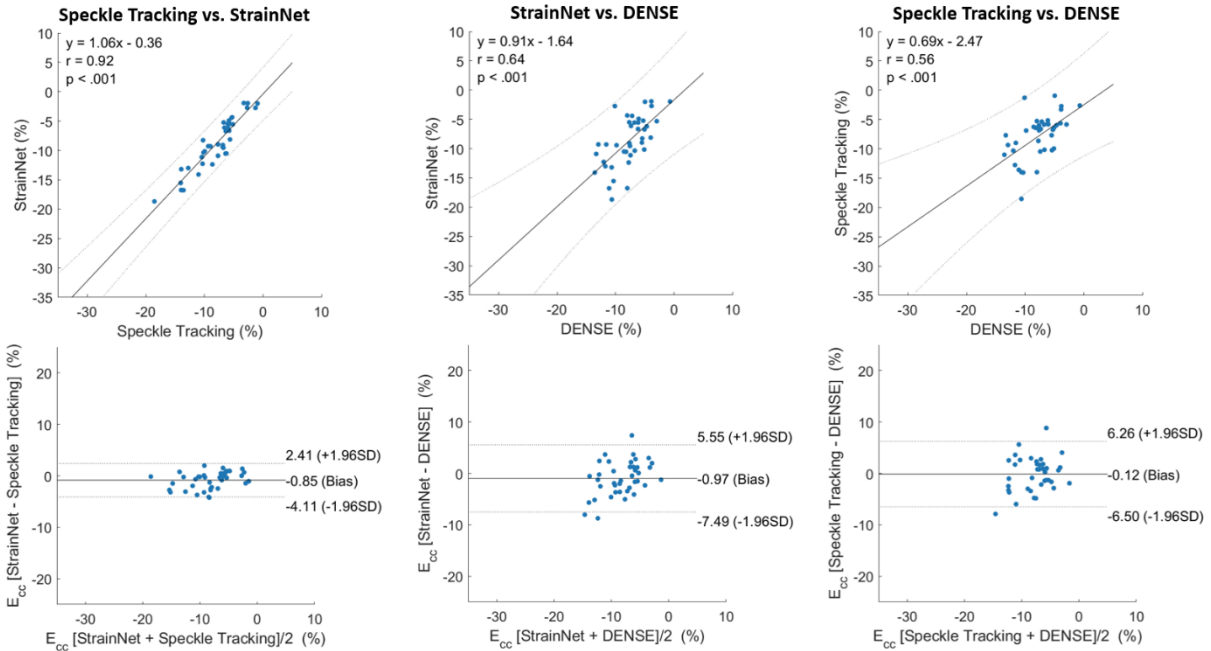
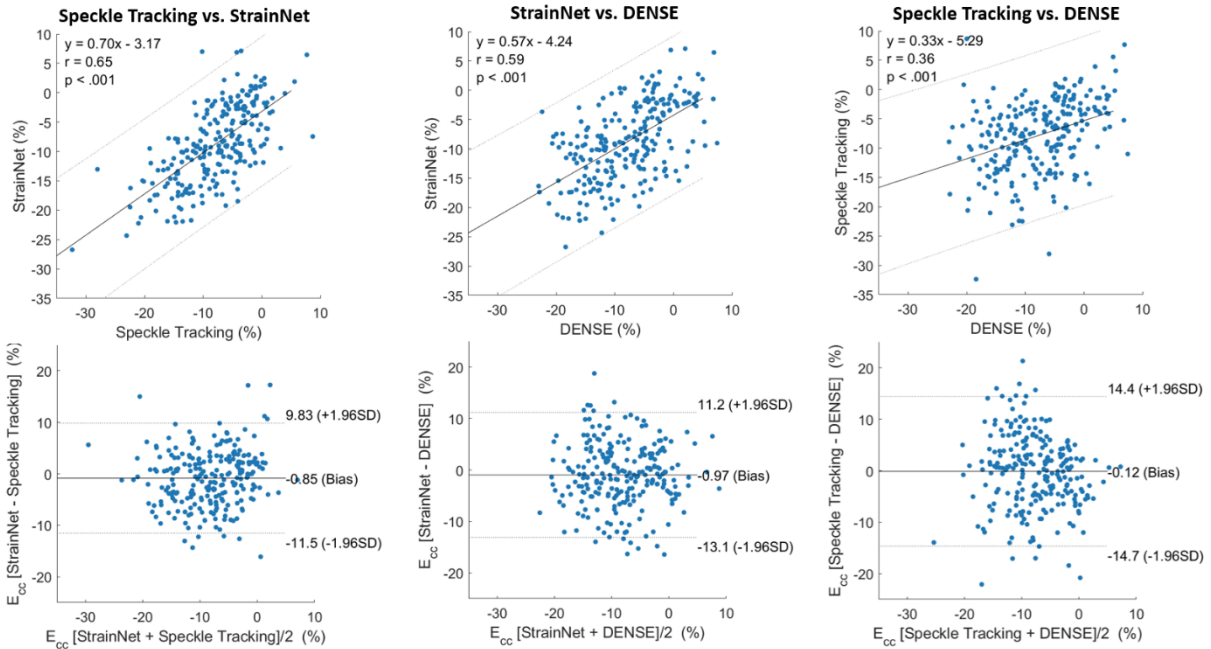


Figure Appendix A-2: Example of a heart failure patient with left bundle branch block. (A) End-systolic displacement and E_{cc} maps comparing StrainNet analysis of echocardiography images and DENSE. Anterior right ventricular insertion points were annotated with red asterisks. (B) Segmental circumferential strain-time curves for speckle tracking, StrainNet analysis of echocardiography, and CMR DENSE. There are 19 frames with 41 ms per frame for echocardiography, and 19 frames with TR = 30ms for CMR DENSE.

A. Global E_{cc}



B. Segmental E_{cc}



C. Summary of ICC, Pearson CC and CV for global and segmental E_{cc}

	Global E_{cc}			Segmental E_{cc}		
	ICC ¹	Pearson CC ¹	CV ²	ICC ¹	Pearson CC ¹	CV ²
Speckle Tracking vs. StrainNet	0.90	0.92	15.35	0.64	0.65	44.23
Speckle Tracking vs. DENSE	0.55	0.56	29.07	0.36	0.36	63.55
StrainNet vs. DENSE	0.59	0.64	28.54	0.58	0.59	50.72

Note. -ICC = Intra-class correlation coefficient, Pearson CC = Pearson correlation coefficient, CV = Coefficient of Variation.

¹Reliability value ranges between 0 and 1, with values closer to 1 representing stronger reliability.

²The higher the coefficient of variation, the greater the level of dispersion around the mean.

Figure Appendix A-3: Correlation and Bland-Altman plots comparing STE, StrainNet analysis of echocardiography and DENSE for end-systolic (A) global and (B) segmental E_{cc} . (C) Comparison of agreement of global and segmental E_{cc} for ICC, Pearson and CV.

Appendix C – List of Publications

C.1 Awards

- American Heart Association Predoctoral Fellowship 2020AHAPRE0000203801,
Percentile Rank: 1.77%, PI: Wang, Yu
Title: Improved Cardiac MRI Feature Tracking by Learning from Displacement-encoded
Imaging, *April 2021 - April 2023*
- Student Stipend for International Society of Magnetic Resonance in Medicine, *2019,*
2021, 2022
- UVA Coulter Fellowship Award, *2023*

C.2 First Author Manuscripts

Wang Y, Sun CY, Ghadimi S, Auger D, Croisille P, Viallon M, Mangion K, Berry C, Haggerty CM, Jing LY, Fornwalt BK, Cao JJ, Cheng JY, Scott AD, Ferreira PF, Oshinski JN, Ennis DB, Bilchick KC, Epstein FH. StrainNet: Improved Myocardial Strain Analysis of Cine MRI by Deep Learning from DENSE. *Radiology: Cardiothoracic Imaging*. 2023 May 4;5(3):e220196.

Wang Y, Epstein FH, et al. TransStrainNet: Improved Strain Analysis of Cine MRI with Long-Range Spatiotemporal Relationship Learning. *Manuscript preparation and to be submitted to Journal of Cardiovascular Magnetic Resonance*.

C.3 Other Manuscripts

Sun CY, Robinson A, **Wang Y**, Bilchick KC, Kramer CM, Weller D, Salerno M, Epstein FH. A Slice-Low-Rank Plus Sparse (slice-L+S) Reconstruction Method for k-t Undersampled Multiband First-Pass Myocardial Perfusion MRI. *Magnetic Resonance in Medicine*. 2022 Sep;88(3):1140-55.

Bivona DJ, Oomen PJ, **Wang Y**, Morales FL, Abdi M, Gao X, Malhotra R, Darby A, Mehta N, Monfredi OJ, Mangrum JM, Mason PK, Levy WC, Mazimba S, Patel AR, Epstein FH, Bilchick KC. Cardiac Magnetic Resonance, Electromechanical Activation, Kidney Function, and Natriuretic Peptides in Cardiac Resynchronization Therapy Upgrades. *Journal of Cardiovascular Development and Disease*. 2023 Sep 22;10(10):409.

Bivona DJ, Ghadimi S, **Wang Y**, Oomen PJ, Malhotra R, Darby A, Mangrum M, Mason PK, Mazimba S, Patel AR, Epstein FH. Machine Learning of ECG Waveforms and Cardiac Magnetic

Resonance for Response and Survival After Cardiac Resynchronization Therapy. *Submitted to Computers in Biology and Medicine.*

Zhang Q, Fotaki A, Ghadimi S, **Wang Y**, Doneva M, Wetzl J, Delfino JG, O'Regan DP, Prieto C, Epstein FH. Improving the efficiency and accuracy of CMR with AI – a review of evidence and proposition of a roadmap to clinical translation. *Submitted to Journal of Cardiovascular Magnetic Resonance.*

C.4 First Author Conference Abstracts

Wang Y, Zhang MM, Bilchick KC, Epstein FH. Transformer-StrainNet: Improved Strain Analysis of Cine MRI with Long-Range Spatiotemporal Relationship Learning. *27th Annual Meeting of SCMR, London, UK, 2024. Oral Presentation.*

Wang Y, Singulane CC, Wang S, Sun CY, Bivona DJ, Bilchick KC, Patel A, Epstein FH. Novel Approach to Regional Circumferential Strain Analysis: Bringing Cardiac Magnetic Resonance Precision to Echocardiography Using a New Artificial Intelligence Model. *34th Annual Meeting of ASE, National Harbor, MD, USA, 2023.*

Wang Y, Sun CY, Wang S, Bivona DJ, Patel A, Bilchick KC, Epstein FH. Multi-modality Strain Analysis: Generalization of CMR-trained StrainNet to Echocardiography. *26th Annual Meeting of SCMR, San Diego, USA, 2023.*

Wang Y, Sun CY, Ghadimi S, Auger D, Croisille P, Viallon M, Mangion K, Berry C, Haggerty CM, Jing LY, Fornwalt BK, Cao JJ, Cheng JY, Scott AD, Ferreira PF, Oshinski JN, Ennis DB, Bilchick KC, Epstein FH. StrainNet: Improved Myocardial Strain Analysis of Cine MRI by Deep Learning from DENSE. *26th Annual Meeting of SCMR, San Diego, USA, 2023.*

Wang Y, Sun CY, Ghadimi S, Auger D, Croisille P, Viallon M, Cao JJ, Cheng JY, Scott AD, Ferreira PF, Oshinski JN, Ennis DB, Bilchick KC, Epstein FH. Improved strain analysis of cine images by deep learning from DENSE: Comparison of a 3D Unet and an optical-flow net. *30th Annual Meeting of ISMRM, London, England, UK, 2022.*

Wang Y, Sun CY, Ghadimi S, Auger D, Croisille P, Viallon M, Cao JJ, Cheng JY, Scott AD, Ferreira PF, Oshinski JN, Ennis DB, Bilchick KC, Epstein FH. Improved strain analysis of cine

images by deep learning from DENSE. *25th Annual Meeting of SCMR, Virtual, 2022. Oral Presentation.*

Wang Y, Ghadimi S, Sun CY, Epstein FH. Cardiac MRI feature tracking by deep learning from DENSE data. *29th Annual Meeting of ISMRM, Virtual, 2021.*

C.5 Invention Disclosures

Wang Y, Sun CY, Ghadimi S, Epstein FH. Method and System for Strain Analysis that Includes CMR-trained StrainNet to Echocardiography. *U.S. Provisional Patent Application Serial No. 63/408,760*.

Wang Y, Sun CY, Epstein FH. System and Method for Improved Cardiac MRI Feature Tracking by Learning from Displacement-Encoded Imaging. *U.S. Provisional Patent Application Serial No. 63/149,900*.

Acknowledgements

There are several faculty members, staff, and students I would like to thank for their contributions and efforts guiding me through my time at UVA.

My Advisor and Full Dissertation Committee – Dr. Frederick Epstein (Advisor), Dr. Craig Meyer (Committee Chair), Dr. Kenneth Bilchick, Dr. Amit Patel, Dr. Claudia Prieto, Dr. Miaomiao Zhang

Epstein Lab – Dr. Frederick Epstein, Dr. Changyu Sun, Dr. Sona Ghadimi, Dr. Soham Shah, Dr. Dan Auger, Jack Echols, Julia Bresticker and Thomas Skacel

Bilchick Lab – Dr. Kenneth Bilchick, Dr. Derek Bivona, Gabrielle Li

Amit Lab – Dr. Amit Patel, Dr. Shuo Wang, Dr. Cristiane De Carvalho Singulane, Dr. Jonathan Pan, Dr. Nisha Hosadurg

UVA BME Staff

Other Collaborators – Dr. Colin Berry, Dr. J. Jane Cao, Joshua Y. Cheng, Dr. Pierre Croisille, Dr. Daniel B. Ennis, Dr. Pedro F. Ferreira, Dr. Brandon K. Fornwalt, Dr. Christopher M. Haggerty, Dr. Linyuan Jing, Dr. Kenneth Mangion, Dr. John N. Oshinski, Dr. Andrew D. Scott, Dr. Magalie Viallon

References

1. Giusca S, Korosoglou G, Montenbruck M, Gersak B, Schwarz AK, Esch S, et al. Multiparametric Early Detection and Prediction of Cardiotoxicity Using Myocardial Strain, T1 and T2 Mapping, and Biochemical Markers: A Longitudinal Cardiac Resonance Imaging Study During 2 Years of Follow-Up. *Circ Cardiovasc Imaging*. 2021;14(6):e012459.
2. Bilchick KC, Auger DA, Abdishektaei M, Mathew R, Sohn MW, Cai X, et al. CMR DENSE and the Seattle Heart Failure Model Inform Survival and Arrhythmia Risk After CRT. *JACC Cardiovasc Imaging*. 2020;13(4):924-36.
3. Mangion K, Carrick D, Carberry J, Mahrous A, McComb C, Oldroyd KG, et al. Circumferential Strain Predicts Major Adverse Cardiovascular Events Following an Acute ST-Segment-Elevation Myocardial Infarction. *Radiology*. 2019;290(2):329-37.
4. Ernande L, Thibault H, Bergerot C, Moulin P, Wen H, Derumeaux G, et al. Systolic myocardial dysfunction in patients with type 2 diabetes mellitus: identification at MR imaging with cine displacement encoding with stimulated echoes. *Radiology*. 2012;265(2):402-9.
5. Axel L, Dougherty L. Heart wall motion: improved method of spatial modulation of magnetization for MR imaging. *Radiology*. 1989;172(2):349-50.
6. Aletras AH, Ding S, Balaban RS, Wen H. DENSE: displacement encoding with stimulated echoes in cardiac functional MRI. *J Magn Reson*. 1999;137(1):247-52.
7. Kim D, Gilson WD, Kramer CM, Epstein FH. Myocardial tissue tracking with two-dimensional cine displacement-encoded MR imaging: Development and initial evaluation. *Radiology*. 2004;230(3):862-71.
8. Osman NF, Sampath S, Atalar E, Prince JL. Imaging longitudinal cardiac strain on short-axis images using strain-encoded MRI. *Magn Reson Med*. 2001;46(2):324-34.

9. Hor KN, Baumann R, Pedrizzetti G, Tonti G, Gottliebson WM, Taylor M, et al. Magnetic resonance derived myocardial strain assessment using feature tracking. *J Vis Exp*. 2011(48).
10. Auger DA, Ghadimi S, Cai X, Reagan CE, Sun C, Abdi M, et al. Reproducibility of global and segmental myocardial strain using cine DENSE at 3 T: a multicenter cardiovascular magnetic resonance study in healthy subjects and patients with heart disease. *J Cardiovasc Magn Reson*. 2022;24(1):23.
11. Mangion K, Burke NMM, McComb C, Carrick D, Woodward R, Berry C. Feature-tracking myocardial strain in healthy adults- a magnetic resonance study at 3.0 tesla. *Sci Rep*. 2019;9(1):3239.
12. Assomull RG, Pennell DJ, Prasad SK. Cardiovascular magnetic resonance in the evaluation of heart failure. *Heart*. 2007;93(8):985-92.
13. de Roos A, Higgins CB. Cardiac radiology: centenary review. *Radiology*. 2014;273(2S):S142-S59.
14. Kalam K, Otahal P, Marwick TH. Prognostic implications of global LV dysfunction: a systematic review and meta-analysis of global longitudinal strain and ejection fraction. *Heart*. 2014;100(21):1673-80.
15. Chitiboi T, Axel L. Magnetic resonance imaging of myocardial strain: a review of current approaches. *Journal of Magnetic Resonance Imaging*. 2017;46(5):1263-80.
16. Sutherland GR, Di Salvo G, Claus P, D'hooge J, Bijnens B. Strain and strain rate imaging: a new clinical approach to quantifying regional myocardial function. *Journal of the American Society of Echocardiography*. 2004;17(7):788-802.
17. Smiseth OA, Torp H, Opdahl A, Haugaa KH, Urheim S. Myocardial strain imaging: how useful is it in clinical decision making? *European heart journal*. 2016;37(15):1196-207.

18. Szymanski C, Lévy F, Tribouilloy C. Should LVEF be replaced by global longitudinal strain? : BMJ Publishing Group Ltd and British Cardiovascular Society; 2014.
19. Plana JC, Galderisi M, Barac A, Ewer MS, Ky B, Scherrer-Crosbie M, et al. Expert consensus for multimodality imaging evaluation of adult patients during and after cancer therapy: a report from the American Society of Echocardiography and the European Association of Cardiovascular Imaging. *European Heart Journal–Cardiovascular Imaging*. 2014;15(10):1063-93.
20. Ong G, Brezden-Masley C, Dhir V, Deva DP, Chan KK, Chow C-M, et al. Myocardial strain imaging by cardiac magnetic resonance for detection of subclinical myocardial dysfunction in breast cancer patients receiving trastuzumab and chemotherapy. *International journal of cardiology*. 2018;261:228-33.
21. Drafts BC, Twomley KM, D'Agostino R, Lawrence J, Avis N, Ellis LR, et al. Low to moderate dose anthracycline-based chemotherapy is associated with early noninvasive imaging evidence of subclinical cardiovascular disease. *JACC: Cardiovascular Imaging*. 2013;6(8):877-85.
22. Bilchick KC, Auger DA, Abdishektaei M, Mathew R, Sohn M-W, Cai X, et al. CMR DENSE and the Seattle heart failure model inform survival and arrhythmia risk after CRT. *JACC: Cardiovascular Imaging*. 2020;13(4):924-36.
23. Shetty AK, Duckett SG, Ginks MR, Ma Y, Sohal M, Bostock J, et al. Cardiac magnetic resonance-derived anatomy, scar, and dyssynchrony fused with fluoroscopy to guide LV lead placement in cardiac resynchronization therapy: a comparison with acute haemodynamic measures and echocardiographic reverse remodelling. *European Heart Journal–Cardiovascular Imaging*. 2013;14(7):692-9.

24. Lindman BR, Dweck MR, Lancellotti P, Génèreux P, Piérard LA, O’Gara PT, et al. Management of asymptomatic severe aortic stenosis: evolving concepts in timing of valve replacement. *JACC: Cardiovascular Imaging*. 2020;13(2):481-93.
25. Mangion K, Carrick D, Carberry J, Mahrous A, McComb C, Oldroyd KG, et al. Circumferential strain predicts major adverse cardiovascular events following an acute ST-segment–elevation myocardial infarction. *Radiology*. 2019;290(2):329-37.
26. Buss SJ, Breuninger K, Lehrke S, Voss A, Galuschky C, Lossnitzer D, et al. Assessment of myocardial deformation with cardiac magnetic resonance strain imaging improves risk stratification in patients with dilated cardiomyopathy. *European Heart Journal-Cardiovascular Imaging*. 2015;16(3):307-15.
27. Wehner GJ, Jing L, Haggerty CM, Suever JD, Chen J, Hamlet SM, et al. Comparison of left ventricular strains and torsion derived from feature tracking and DENSE CMR. *Journal of Cardiovascular Magnetic Resonance*. 2018;20(1):63.
28. Amzulescu MS, De Craene M, Langet H, Pasquet A, Vancraeynest D, Pouleur A-C, et al. Myocardial strain imaging: review of general principles, validation, and sources of discrepancies. *European Heart Journal-Cardiovascular Imaging*. 2019;20(6):605-19.
29. Johnson C, Kuyt K, Oxborough D, Stout M. Practical tips and tricks in measuring strain, strain rate and twist for the left and right ventricles. *Echo Res Pract*. 2019;6(3):R87-R98.
30. Cerqueira MD, Weissman NJ, Dilsizian V, Jacobs AK, Kaul S, Laskey WK, et al. Standardized myocardial segmentation and nomenclature for tomographic imaging of the heart. A statement for healthcare professionals from the Cardiac Imaging Committee of the Council on Clinical Cardiology of the American Heart Association. *Circulation*. 2002;105(4):539-42.

31. Geyer H, Caracciolo G, Abe H, Wilansky S, Carerj S, Gentile F, et al. Assessment of myocardial mechanics using speckle tracking echocardiography: fundamentals and clinical applications. *Journal of the American Society of Echocardiography*. 2010;23(4):351-69.
32. Blessberger H, Binder T. Two dimensional speckle tracking echocardiography: basic principles. *Heart*. 2010;96(9):716-22.
33. Mondillo S, Galderisi M, Mele D, Cameli M, Lomoriello VS, Zacà V, et al. Speckle-tracking echocardiography: a new technique for assessing myocardial function. *Journal of Ultrasound in Medicine*. 2011;30(1):71-83.
34. Pourmorteza A, Chen MY, van der Pals J, Arai AE, McVeigh ER. Correlation of CT-based regional cardiac function (SQUEEZ) with myocardial strain calculated from tagged MRI: an experimental study. *The international journal of cardiovascular imaging*. 2016;32:817-23.
35. McVeigh ER, Pourmorteza A, Guttman M, Sandfort V, Contijoch F, Budhiraja S, et al. Regional myocardial strain measurements from 4DCT in patients with normal LV function. *Journal of cardiovascular computed tomography*. 2018;12(5):372-8.
36. Chen Z, Contijoch F, Kahn AM, Kligerman S, Narayan HK, Manohar A, et al. Myocardial Regional Shortening from 4D Cardiac CT Angiography for the Detection of Left Ventricular Segmental Wall Motion Abnormality. *Radiology: Cardiothoracic Imaging*. 2023;5(2):e220134.
37. Axel L, Dougherty L. MR imaging of motion with spatial modulation of magnetization. *Radiology*. 1989;171(3):841-5.
38. Osman NF, Kerwin WS, McVeigh ER, Prince JL. Cardiac motion tracking using CINE harmonic phase (HARP) magnetic resonance imaging. *Magnetic Resonance in Medicine: An Official Journal of the International Society for Magnetic Resonance in Medicine*. 1999;42(6):1048-60.

39. Hess AT, Zhong X, Spottiswoode BS, Epstein FH, Meintjes EM. Myocardial 3D strain calculation by combining cine displacement encoding with stimulated echoes (DENSE) and cine strain encoding (SENC) imaging. *Magnetic Resonance in Medicine: An Official Journal of the International Society for Magnetic Resonance in Medicine*. 2009;62(1):77-84.
40. Lin K, Meng L, Collins JD, Chowdhary V, Markl M, Carr JC. Reproducibility of cine displacement encoding with stimulated echoes (DENSE) in human subjects. *Magnetic resonance imaging*. 2017;35:148-53.
41. Spottiswoode BS, Zhong X, Hess AT, Kramer C, Meintjes EM, Mayosi BM, et al. Tracking myocardial motion from cine DENSE images using spatiotemporal phase unwrapping and temporal fitting. *IEEE transactions on medical imaging*. 2006;26(1):15-30.
42. Spottiswoode BS, Zhong X, Lorenz CH, Mayosi BM, Meintjes EM, Epstein FH. Motion-guided segmentation for cine DENSE MRI. *Med Image Anal*. 2009;13(1):105-15.
43. Schuster A, Hor KN, Kowallick JT, Beerbaum P, Kutty S. Cardiovascular magnetic resonance myocardial feature tracking: concepts and clinical applications. *Circulation: Cardiovascular Imaging*. 2016;9(4):e004077.
44. Horn BK, Schunck BG, editors. Determining optical flow. *Techniques and Applications of Image Understanding*; 1981: International Society for Optics and Photonics.
45. Cho K, Van Merriënboer B, Bahdanau D, Bengio Y. On the properties of neural machine translation: Encoder-decoder approaches. *arXiv preprint arXiv:14091259*. 2014.
46. Ronneberger O, Fischer P, Brox T. U-Net: Convolutional Networks for Biomedical Image Segmentation. *Medical Image Computing and Computer-Assisted Intervention, Pt Iii*. 2015;9351:234-41.

47. Yin XX, Sun L, Fu Y, Lu R, Zhang Y. U-Net-Based Medical Image Segmentation. *J Healthc Eng.* 2022;2022:4189781.
48. Dosovitskiy A, Beyer L, Kolesnikov A, Weissenborn D, Zhai X, Unterthiner T, et al. An image is worth 16x16 words: Transformers for image recognition at scale. *arXiv preprint arXiv:201011929.* 2020.
49. Vaswani A, Shazeer N, Parmar N, Uszkoreit J, Jones L, Gomez AN, et al. Attention is all you need. *Advances in neural information processing systems.* 2017;30.
50. Matsoukas C, Haslum JF, Söderberg M, Smith K. Is it time to replace cnns with transformers for medical images? *arXiv preprint arXiv:210809038.* 2021.
51. Morales MA, van den Boomen M, Nguyen C, Kalpathy-Cramer J, Rosen BR, Stultz CM, et al. DeepStrain: A Deep Learning Workflow for the Automated Characterization of Cardiac Mechanics. *Front Cardiovasc Med.* 2021;8:730316.
52. Qiao M, Wang Y, Guo Y, Huang L, Xia L, Tao Q. Temporally coherent cardiac motion tracking from cine MRI: Traditional registration method and modern CNN method. *Med Phys.* 2020;47(9):4189-98.
53. Yu HC, Sun SH, Yu HC, Chen X, Shi HH, Huang TS, et al. FOAL: Fast Online Adaptive Learning for Cardiac Motion Estimation. 2020 *Ieee/Cvf Conference on Computer Vision and Pattern Recognition (Cvpr).* 2020:4312-22.
54. Qin C, Bai WJ, Schlemper J, Petersen SE, Piechnik SK, Neubauer S, et al. Joint Motion Estimation and Segmentation from Undersampled Cardiac MR Image. *Lect Notes Comput Sc.* 2018;11074:55-63.

55. Backhaus SJ, Aldehayat H, Kowallick JT, Evertz R, Lange T, Kutty S, et al. Artificial intelligence fully automated myocardial strain quantification for risk stratification following acute myocardial infarction. *Scientific reports*. 2022;12(1):12220.
56. Kawakubo M, Moriyama D, Yamasaki Y, Abe K, Hosokawa K, Moriyama T, et al. Right ventricular strain and volume analyses through deep learning-based fully automatic segmentation based on radial long-axis reconstruction of short-axis cine magnetic resonance images. *Magnetic Resonance Materials in Physics, Biology and Medicine*. 2022;35(6):911-21.
57. Tan Z, Yang Y, Wu X, Li S, Li L, Zhong L, et al. Left atrial remodeling and the prognostic value of feature tracking derived left atrial strain in patients with light-chain amyloidosis: a cardiovascular magnetic resonance study. *The International Journal of Cardiovascular Imaging*. 2022;38(7):1519-32.
58. Cau R, Pisu F, Porcu M, Cademartiri F, Montisci R, Bassareo P, et al. Machine learning approach in diagnosing Takotsubo cardiomyopathy: The role of the combined evaluation of atrial and ventricular strain, and parametric mapping. *International Journal of Cardiology*. 2023;373:124-33.
59. Qin C, Schlemper J, Caballero J, Price AN, Hajnal JV, Rueckert D. Convolutional recurrent neural networks for dynamic MR image reconstruction. *IEEE transactions on medical imaging*. 2018;38(1):280-90.
60. Yu H, Sun S, Yu H, Chen X, Shi H, Huang TS, et al., editors. Foal: Fast online adaptive learning for cardiac motion estimation. *Proceedings of the IEEE/CVF Conference on Computer Vision and Pattern Recognition*; 2020.

61. Wang Y, Sun C, Ghadimi S, Auger DC, Croisille P, Viallon M, et al. StrainNet: Improved Myocardial Strain Analysis of Cine MRI by Deep Learning from DENSE. *Radiology: Cardiothoracic Imaging*. 2023;5(3):e220196.
62. Morales MA, Cirillo J, Nakata K, Kucukseymen S, Ngo LH, Izquierdo-Garcia D, et al. Comparison of DeepStrain and feature tracking for cardiac MRI strain analysis. *Journal of Magnetic Resonance Imaging*. 2022.
63. Ye M, Kanski M, Yang D, Chang Q, Yan Z, Huang Q, et al., editors. Deeptag: An unsupervised deep learning method for motion tracking on cardiac tagging magnetic resonance images. *Proceedings of the IEEE/CVF conference on computer vision and pattern recognition*; 2021.
64. Ghadimi S, Auger DA, Feng X, Sun C, Meyer CH, Bilchick KC, et al. Fully-automated global and segmental strain analysis of DENSE cardiovascular magnetic resonance using deep learning for segmentation and phase unwrapping. *J Cardiovasc Magn Reson*. 2021;23(1):20.
65. Auricchio A, Abraham WT. Cardiac resynchronization therapy: current state of the art: cost versus benefit. *Circulation*. 2004;109(3):300-7.
66. Sieniewicz BJ, Gould J, Porter B, Sidhu BS, Teall T, Webb J, et al. Understanding non-response to cardiac resynchronisation therapy: common problems and potential solutions. *Heart Fail Rev*. 2019;24(1):41-54.
67. Shetty AK, Duckett SG, Ginks MR, Ma Y, Sohal M, Bostock J, et al. Cardiac magnetic resonance-derived anatomy, scar, and dyssynchrony fused with fluoroscopy to guide LV lead placement in cardiac resynchronization therapy: a comparison with acute haemodynamic measures and echocardiographic reverse remodelling. *Eur Heart J Cardiovasc Imaging*. 2013;14(7):692-9.

68. Exner DV, Auricchio A, Singh JP. Contemporary and future trends in cardiac resynchronization therapy to enhance response. *Heart rhythm*. 2012;9(8):S27-S35.
69. Ramachandran R, Chen X, Kramer CM, Epstein FH, Bilchick KC. Singular Value Decomposition Applied to Cardiac Strain from MR Imaging for Selection of Optimal Cardiac Resynchronization Therapy Candidates. *Radiology*. 2015;275(2):413-20.
70. Bilchick KC, Auger DA, Abdishektaei M, Mathew R, Sohn MW, Cai XY, et al. CMR DENSE and the Seattle Heart Failure Model Inform Survival and Arrhythmia Risk After CRT. *Jacc-Cardiovasc Imag*. 2020;13(4):924-36.
71. Young AA, Li B, Kirton RS, Cowan BR. Generalized spatiotemporal myocardial strain analysis for DENSE and SPAMM imaging. *Magn Reson Med*. 2012;67(6):1590-9.
72. Kar J, Knutsen AK, Cupps BP, Pasque MK. A validation of two-dimensional in vivo regional strain computed from displacement encoding with stimulated echoes (DENSE), in reference to tagged magnetic resonance imaging and studies in repeatability. *Ann Biomed Eng*. 2014;42(3):541-54.
73. Bistoquet A, Oshinski J, Skrinjar O. Myocardial deformation recovery from cine MRI using a nearly incompressible biventricular model. *Medical Image Analysis*. 2008;12(1):69-85.
74. Ilg E, Mayer N, Saikia T, Keuper M, Dosovitskiy A, Brox T. FlowNet 2.0: Evolution of Optical Flow Estimation with Deep Networks. *Proc Cvpr Ieee*. 2017:1647-55.
75. Sun DQ, Yang XD, Liu MY, Kautz J. PWC-Net: CNNs for Optical Flow Using Pyramid, Warping, and Cost Volume. 2018 *Ieee/Cvf Conference on Computer Vision and Pattern Recognition (Cvpr)*. 2018:8934-43.

76. Hatamizadeh A, Tang Y, Nath V, Yang D, Myronenko A, Landman B, et al., editors. Unetr: Transformers for 3d medical image segmentation. Proceedings of the IEEE/CVF winter conference on applications of computer vision; 2022.
77. Hochreiter S, Schmidhuber J. Long short-term memory. *Neural computation*. 1997;9(8):1735-80.
78. Gao Y, Phillips JM, Zheng Y, Min R, Fletcher PT, Gerig G, editors. Fully convolutional structured LSTM networks for joint 4D medical image segmentation. 2018 IEEE 15th international symposium on biomedical imaging (ISBI 2018); 2018: IEEE.
79. Li S, Jin X, Xuan Y, Zhou X, Chen W, Wang Y-X, et al. Enhancing the locality and breaking the memory bottleneck of transformer on time series forecasting. *Advances in neural information processing systems*. 2019;32.
80. Bahdanau D, Cho K, Bengio Y. Neural machine translation by jointly learning to align and translate. arXiv preprint arXiv:14090473. 2014.
81. Liu Z, Lin Y, Cao Y, Hu H, Wei Y, Zhang Z, et al., editors. Swin transformer: Hierarchical vision transformer using shifted windows. Proceedings of the IEEE/CVF international conference on computer vision; 2021.
82. Virani SS, Alonso A, Benjamin EJ, Bittencourt MS, Callaway CW, Carson AP, et al. Heart disease and stroke statistics—2020 update: a report from the American Heart Association. *Circulation*. 2020;141(9):e139-e596.
83. Heidenreich PA, Albert NM, Allen LA, Bluemke DA, Butler J, Fonarow GC, et al. Forecasting the impact of heart failure in the United States: a policy statement from the American Heart Association. *Circulation: Heart Failure*. 2013;6(3):606-19.

84. Abraham WT, Fisher WG, Smith AL, Delurgio DB, Leon AR, Loh E, et al. Cardiac resynchronization in chronic heart failure. *New England Journal of Medicine*. 2002;346(24):1845-53.
85. Bristow MR, Saxon LA, Boehmer J, Krueger S, Kass DA, De Marco T, et al. Cardiac-resynchronization therapy with or without an implantable defibrillator in advanced chronic heart failure. *New England Journal of Medicine*. 2004;350(21):2140-50.
86. Cleland JG, Daubert J-C, Erdmann E, Freemantle N, Gras D, Kappenberger L, et al. The effect of cardiac resynchronization on morbidity and mortality in heart failure. *New England Journal of Medicine*. 2005;352(15):1539-49.
87. De Marco T, Wolfel E, Feldman AM, Lowes B, Higginbotham MB, Ghali JK, et al. Impact of cardiac resynchronization therapy on exercise performance, functional capacity, and quality of life in systolic heart failure with QRS prolongation: COMPANION trial sub-study. *Journal of cardiac failure*. 2008;14(1):9-18.
88. Linde C, Abraham WT, Gold MR, St. John Sutton M, Ghio S, Daubert C, et al. Randomized trial of cardiac resynchronization in mildly symptomatic heart failure patients and in asymptomatic patients with left ventricular dysfunction and previous heart failure symptoms. *Journal of the American College of Cardiology*. 2008;52(23):1834-43.
89. Moss AJ, Hall WJ, Cannom DS, Klein H, Brown MW, Daubert JP, et al. Cardiac-resynchronization therapy for the prevention of heart-failure events. *New England Journal of Medicine*. 2009;361(14):1329-38.
90. Tang AS, Wells GA, Talajic M, Arnold MO, Sheldon R, Connolly S, et al. Cardiac-resynchronization therapy for mild-to-moderate heart failure. *New England Journal of Medicine*. 2010;363(25):2385-95.

91. Lindenfeld J, Feldman AM, Saxon L, Boehmer J, Carson P, Ghali JK, et al. Effects of cardiac resynchronization therapy with or without a defibrillator on survival and hospitalizations in patients with New York Heart Association class IV heart failure. *Circulation*. 2007;115(2):204-12.
92. Bilchick KC, Kuruvilla S, Hamirani YS, Ramachandran R, Clarke SA, Parker KM, et al. Impact of mechanical activation, scar, and electrical timing on cardiac resynchronization therapy response and clinical outcomes. *Journal of the American College of Cardiology*. 2014;63(16):1657-66.
93. Ramachandran R, Chen X, Kramer CM, Epstein FH, Bilchick KC. Singular value decomposition applied to cardiac strain from MR imaging for selection of optimal cardiac resynchronization therapy candidates. *Radiology*. 2015;275(2):413.
94. Rabbat MG, Kwong RY, Heitner JF, Young AA, Shanbhag SM, Petersen SE, et al. *The Future of Cardiac Magnetic Resonance Clinical Trials*. Elsevier; 2021.
95. Bilchick KC, Auger DA, Abdishektaei M, Mathew R, Sohn M-W, Cai X, et al. CMR DENSE and the Seattle heart failure model inform survival and arrhythmia risk after CRT. *Cardiovascular Imaging*. 2020;13(4):924-36.
96. Auger DA, Bilchick KC, Gonzalez JA, Cui SX, Holmes JW, Kramer CM, et al. Imaging left-ventricular mechanical activation in heart failure patients using cine DENSE MRI: Validation and implications for cardiac resynchronization therapy. *Journal of Magnetic Resonance Imaging*. 2017;46(3):887-96.
97. Leclercq C, Faris O, Tunin R, Johnson J, Kato R, Evans F, et al. Systolic improvement and mechanical resynchronization does not require electrical synchrony in the dilated failing heart with left bundle-branch block. *Circulation*. 2002;106(14):1760-3.

98. Bivona DJ, Tallavajhala S, Abdi M, Oomen PJ, Gao X, Malhotra R, et al. Machine learning for multidimensional response and survival after cardiac resynchronization therapy using features from cardiac magnetic resonance. *Heart Rhythm O2*. 2022;3(5):542-52.
99. Bivona DJ, Oomen PJA, Wang Y, Morales FL, Abdi M, Gao X, et al. Cardiac Magnetic Resonance, Electromechanical Activation, Kidney Function, and Natriuretic Peptides in Cardiac Resynchronization Therapy Upgrades. *J Cardiovasc Dev Dis*. 2023;10(10).
100. Pedrizzetti G, Claus P, Kilner PJ, Nagel E. Principles of cardiovascular magnetic resonance feature tracking and echocardiographic speckle tracking for informed clinical use. *J Cardiovasc Magn Reson*. 2016;18(1):51.
101. Pryds K, Larsen AH, Hansen MS, Grondal AYK, Tougaard RS, Hansson NH, et al. Myocardial strain assessed by feature tracking cardiac magnetic resonance in patients with a variety of cardiovascular diseases - A comparison with echocardiography. *Sci Rep*. 2019;9(1):11296.
102. Pourmorteza A, Schuleri KH, Herzka DA, Lardo AC, McVeigh ER. A new method for cardiac computed tomography regional function assessment: stretch quantifier for endocardial engraved zones (SQUEEZ). *Circ Cardiovasc Imaging*. 2012;5(2):243-50.
103. Pourmorteza A, Schuleri KH, Herzka DA, Lardo AC, McVeigh ER. Regional cardiac function assessment in 4D CT: comparison between SQUEEZ and ejection fraction. *Annu Int Conf IEEE Eng Med Biol Soc*. 2012;2012:4966-9.
104. Claus P, Omar AMS, Pedrizzetti G, Sengupta PP, Nagel E. Tissue Tracking Technology for Assessing Cardiac Mechanics: Principles, Normal Values, and Clinical Applications. *JACC Cardiovasc Imaging*. 2015;8(12):1444-60.

105. Brann A, Miller J, Eshraghian E, Park JJ, Greenberg B. Global longitudinal strain predicts clinical outcomes in patients with heart failure with preserved ejection fraction. *Eur J Heart Fail.* 2023;25(10):1755-65.
106. Chengode S. Left ventricular global systolic function assessment by echocardiography. *Ann Card Anaesth.* 2016;19(Supplement):S26-S34.
107. Reisner SA, Lysyansky P, Agmon Y, Mutlak D, Lessick J, Friedman Z. Global longitudinal strain: a novel index of left ventricular systolic function. *J Am Soc Echocardiogr.* 2004;17(6):630-3.
108. Liu JE, Barac A, Thavendiranathan P, Scherrer-Crosbie M. Strain Imaging in Cardio-Oncology. *JACC CardioOncol.* 2020;2(5):677-89.
109. Oikonomou EK, Kokkinidis DG, Kampaktis PN, Amir EA, Marwick TH, Gupta D, et al. Assessment of Prognostic Value of Left Ventricular Global Longitudinal Strain for Early Prediction of Chemotherapy-Induced Cardiotoxicity: A Systematic Review and Meta-analysis. *JAMA Cardiol.* 2019;4(10):1007-18.
110. Zamorano JL, Lancellotti P, Rodriguez Munoz D, Aboyans V, Asteggiano R, Galderisi M, et al. 2016 ESC Position Paper on cancer treatments and cardiovascular toxicity developed under the auspices of the ESC Committee for Practice Guidelines: The Task Force for cancer treatments and cardiovascular toxicity of the European Society of Cardiology (ESC). *European heart journal.* 2016;37(36):2768-801.
111. Steen H, Montenbruck M, Gerzak B, Schwarz AK, Kelle S, Giusca S, et al. Cardiotoxicity during cancer treatment causes more regional than global dysfunction: the PREFECT Study. *Journal of the American College of Cardiology.* 2020;75(11_Supplement_1):1824-.

112. Veldmann M, Ehses P, Chow K, Nielsen JF, Zaitsev M, Stocker T. Open-source MR imaging and reconstruction workflow. *Magn Reson Med.* 2022;88(6):2395-407.
113. Ilg E, Mayer N, Saikia T, Keuper M, Dosovitskiy A, Brox T, editors. FlowNet 2.0: Evolution of optical flow estimation with deep networks. *Proceedings of the IEEE conference on computer vision and pattern recognition*; 2017.
114. Dosovitskiy A, Fischer P, Ilg E, Hausser P, Hazirbas C, Golkov V, et al. FlowNet: Learning Optical Flow with Convolutional Networks. *Ieee I Conf Comp Vis.* 2015:2758-66.